UNIVERSITÀ DEGLI STUDI DI MILANO-BICOCCA

FACOLTÀ DI SCIENZE MATEMATICHE, FISICHE E NATURALI
Corso di Laurea in Fisica

TESI DI LAUREA MAGISTRALE

STUDY AND VALIDATION OF AN INNOVATIVE EXPERIMENT TO MEASURE THE HADRONIC CONTRIBUTIONS TO THE RUNNING OF α_{em}

Relatore:
Prof. M. Paganoni

Correlatore:
Prof.ssa C. Matteuzzi

Candidato:
Matteo Bonanomi
Matricola 777113

Anno Accademico 2017-2018

ABSTRACT

The aim of this work is to present recent developments in the study of an innovative experiment to measure the hadronic contributions to the running of the QED coupling α_{em} in the space-like region, exploiting the scattering of high-energy muons on atomic electrons of a graphite target. The differential cross section of this process, measured as a function of the squared momentum transfer $t = -q^2<0$ (space-like region), provides direct sensitivity to the leading-order hadronic contribution to the muon anomaly (a_μ^{HLO}). This work mainly presents the results of the analysis of the 2017 test beam data, as well as the design of a dedicated GEANT4 simulation of the experimental set-up. The main goal of the test beam was to have a first proof-of-concept of the final experiment and to study the effect of multiple scattering on $\mathcal{O}(10\ \text{GeV})$ electrons in graphite targets. The ratio Monte Carlo/Data of the distributions of the difference $(\theta_{out} - \theta_{in})$ for traversing electrons, shows a $\sim 1\%$ agreement between the two samples, in particular in the gaussian core region. We also studied an analytical model based on the convolution of a gaussian distribution and a Student's, which takes into account both the multiple scattering and resolution effects and describes the experimental distribution with good accuracy in the entire range. We used a tracking algorithm based on multiple scattering covariance error matrix and on chi-square minimization, to study the effect of the multiple scattering in thin silicon trackers. The entire analysis did not return any showstopper for the final experiment and allowed us to understand several details which must be taken into account to achieve the final desired precision of 0.3% on a_μ^{HLO}.

A smooth sea never made a skillful mariner

ACKNOWLEDGEMENTS

To Sergio & Giuseppe

I would like to thank all the brilliant people I had the opportunity to meet during this thesis activity: every meeting was an occasion to learn and to improve. A special thanks goes to my supervisor prof. Marco Paganoni for introducing me to my co-supervisor prof. Clara Matteuzzi. The doors of their offices were always open whenever I needed it. Thanks to all the members of the MUonE collaboration for the occasion to work in such a stimulating environment.

I must express my gratitude to my friends: without them I would not be the person I am today. During these years we grew up together, we shared fears and happiness and we have become better men and women. Thanks for encouraging and supporting me everyday throughout my study. I owe you a lot!

Last but not least, I would like to thank my parents and my family. Thanks for having taught me never to give up, to be determined and to believe in my dreams. This is for you.

Matteo Bonanomi

CONTENTS

1

INTRODUCTION

The aim of this work is to present the study and development of an innovative experiment to measure the hadronic contributions to the running of the electromagnetic coupling α_{em} in the space-like region, exploiting the scattering of high-energy muons on atomic electrons of low-Z target. The differential cross section of this process, provides direct sensitivity to the leading-order hadronic contribution to the muon anomaly ($a_\mu = \frac{g-2}{2}$), a_μ^{HLO}.

At present a_μ is not only one of the most precisely measured quantities in particle physics, but theory and experiment lie apart by $(3-4)\sigma$, $\Delta a_\mu(Exp - SM) \simeq (28 \pm 8) \times 10^{-10}$. This discrepancy has been considered during the last years as one of the most intriguing indications of physics beyond the Standard Model (SM). This direct measurement of a_μ^{HLO} will provide an independent determination and consolidate the theoretical prediction for the muon $g-2$ in the SM.

This chapter gives an overall introduction to the theory of magnetic moments, from the classical interpretation to the Dirac relativistic theory and the discovery of the so called *anomaly*. In section 1.2 is presented the theory of the electromagnetic coupling (α_{em}) running. In chapter 2, after a brief recap on the history of the muon, I give an overview of the a_μ value in the Standard Model, as well as the current status of a_μ from an experimental point of view. Chapter 3 contains the core of this work: here is presented the proposal of this new experiment, after a brief theoretical framework. After a description of the proposed experimental set-up and considerations on the achievable statistical precision, I discuss more in detail the data analysis of the test beam we had in October 2017 using 12, 20 GeV e^- beams and a 160GeV μ beam, available at CERN North-Area. Finally, in chapter 5, I present the outcome of this work, the current status of the experiment and possible future developments.

1.1 MAGNETIC MOMENTS

The study of magnetic moments of subatomic particles grew up with the development of quantum mechanics. For fermions the magnetic dipole moment is related to the spin by

$$\vec{\mu} = g\frac{Qe}{2m}\vec{s}$$

Where $Q = \pm 1$, $e > 0$ is the particle charge and m, $\vec{s}$ are the mass and the spin of the fermion respectively. The *gyromagnetic ratio* g is the ratio of the magnetic moment of a system to the value obtained by multiplying its angular momentum by the Larmor ratio ($e/2mc$). For an orbiting electron $g = 1$. When Goudschmit and Uhlenbeck postulated the spinning electron with angular momentum $(h/4\pi)$ to explain the anomalous Zeeman effect, it was surprising that its magnetic moment, one Bohr magneton, was twice the expected value: the gyromagnetic ratio for the electron was apparently 2. Later Dirac found that this value came out as a natural consequence of his relativistic equation for the electron

$$\left(i\delta_\mu - eA_\mu\right)\gamma^\mu\psi = m\psi$$

This was one of the great successes of Dirac's relativistic theory and, for some years, experimental data confirmed his prediction. The electron had $g = 2$, and his equation seemed to describe nature.

A surprising and unexpected result was obtained in 1933 when Stern and his collaborators measured the g-factor of the proton to be ~5.5 instead of the expected value of 2. This discrepancy from the theoretical value was observed also for the electron and could be explained by a term in Dirac equation, proposed by Pauli, which would give a deviation

$$a\frac{e}{2m}\sigma_{\mu\nu}F^{\mu\nu}\psi \;\rightarrow\; g = 2(1+a)$$

In 1947, motivated by measurements of the hyperfine structure in hydrogen that obtained splittings larger than expected from the Dirac theory, Schwinger showed that from a theoretical viewpoint these "discrepancies can be accounted for by a small additional electron spin magnetic moment" that arises from the lowest-order radiative correction to the Dirac moment

$$\frac{\delta\mu}{\mu} = \frac{1}{2\pi}\frac{e^2}{\hbar c} = \frac{\alpha}{2\pi} = 0.001162.$$

Hence, the magnetic moment for a fermion can be written into two terms:

$$\mu = (1+a)\frac{e\hbar}{2m}, \text{ where } a = \frac{(g-2)}{2}.$$

The first term is the Dirac moment, 1 in units of the appropriate magneton $e\hbar/2m$. The second term is the anomalous (Pauli) moment, where the dimensionless quantity a (Schwinger's $\delta\mu/\mu$) is sometimes referred to as the $g-2$ *anomaly* [1], [2].

Both the electron and muon anomalies have been measured very precisely:

$$a_e^{exp} = 1159652180.73(28) \times 10^{-12} \pm 0.24 \text{ ppb}$$

$$a_\mu^{exp} = 116592089(63) \times 10^{-11} \pm 0.54 \text{ ppm}$$

While the electron anomaly has been measured very precisely, it is significantly less sensitive to heavier physics, because the relative contribution of heavier virtual particles to the muon anomaly goes as $(m_\mu/m_e)^2 \simeq 43000$. Thus the lowest-order hadronic contribution to electron anomaly is 1.5 ppb of a_e, while for the muon is ~ 60 ppm. So with much less precision, when compared with the electron, the measured muon anomaly is sensitive to mass scales in the several hundred GeV region. This not only includes the contribution of the W and Z bosons, but perhaps contributions from new, as yet undiscovered, particles such as the supersymmetric partners of the electroweak gauge bosons.

1.2 THE RUNNING OF α_{em}

In QED the lepton g-factor can be expressed as a perturbation series in powers of α/π:

$$a^{QED} = A(\alpha/\pi) + B(\alpha/\pi)^2 + C(\alpha/\pi)^3 + \dots$$

In the following we will see that also the leading-order hadronic contributions to a can be expressed in terms of α_{em}. Hence, the precision on the electromagnetic coupling directly reflects on a_μ.

In the electroweak Standard Model, the running of the electromagnetic coupling α is determined by the theory as

$$\alpha(t) = \frac{\alpha(0)}{1 - \Delta\alpha(t)} = \frac{\alpha(0)}{1 - \Delta\alpha_{lep}(t) - \Delta\alpha_{had}(t)}$$

Where $t = -q^2 < 0$ and $\alpha(0) = \alpha_0$ is the Sommerfeld fine structure constant, which has been measured to a precision of 1.7×10^{-9}. Precise knowledge of $\alpha(q^2)$ is fundamental for any electroweak observable prediction at $q^2 \neq 0$. From here it comes the necessity of evolving α from $q^2 = 0$ up to the Z-mass scale $q^2 = m_Z^2$. The evolution expressed by the quantity $\Delta\alpha$ receives contributions from leptons, hadrons and the gauge bosons. The largest uncertainty on any evolved value of $\alpha(q^2)$, especially for $| q^2 |> 4m_\pi^2$, comes from the hadronic contributions. More precisely, the contribution to the vacuum polarization (hVP) can not be calculated directly but has to be estimated with the help of a dispersion integral and evaluated by using total cross section measurements of $e^+e^- \to$had. at low energies. Moreover, not only hVP limits the precision on any evolved value $\alpha(q^2)$ but also on a_μ, especially in the hadronic sector, as we will see in more detail in the next section.

From an experimental point of view, attempts have been made to measure the running of α directly, using e^+e^- data at various energies, such as measuring the ratio of $e^+e^-\gamma/e^+e^-$, or more directly the angular distribution of Bhabha scattering [3]. In this work we are going to present an alternative approach to measure the running of the fine-structure constant in the space-like region by scattering

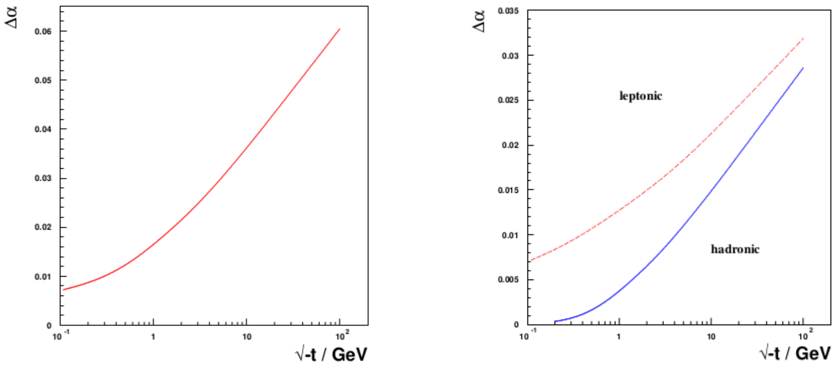

(a) $\Delta\alpha$ versus $\sqrt{-t}$ in units of GeV in the space-like region.

(b) Contributions to $\Delta\alpha$ from leptons and hadrons versus $\sqrt{-t}$ in units of GeV.

Figure 1: The running of $\alpha(t)$.

high energy muons on atomic electrons of a low-Z target through the process $\mu e \to \mu e$. For any scattering process, the space-like momentum transfer $t = - \mid q^2 \mid$ is

$$t = -\frac{1}{2}s(1 - \cos\theta)$$

It is related to the total invariant energy $\sqrt{s}$ and to the scattering angle θ of the final-state lepton. Figure 1a presents the t-dependence of the overall running $\Delta\alpha(t)$, while in figure 1b depicts the two contributions from leptons and hadrons. As one can see, the running of the electromagnetic coupling is dominated by the contribution from leptons, while the contribution involving hadrons gets relevant only for high $\mid t \mid$ values.

1.2.1 *Theory of the α running*

To measure the running of α from a scattering process between two leptons $l_1 l_2 \to l_1 l_2$, one exploits the fact that the cross section can be decomposed into three factors:

$$\frac{d\sigma}{dt} = \frac{d\sigma^0}{dt}\left(\frac{\alpha(t)}{\alpha(0)}\right)^2 (1 + \Delta r(t))$$

Where the first factor on the right-hand side refers to the effective Born cross section for the considered process, including soft and virtual photons, and accounts the strongest dependence on t. The vacuum-polarization effect in the leading photon t channel exchange is incorporated in the running of α and gives rise to the squared factor. The third factor, $\Delta r(t)$, collects all the remaining real and virtual radiative effects not incorporated in the running of α.

- The differential cross section $\frac{d\sigma^0}{dt}$ is defined as

$$\frac{d\sigma^0}{dt} = \frac{d\sigma^B}{dt}\left(\frac{\alpha(0)}{\alpha(t)}\right)^2$$

The factor $d\sigma^B/dt$ is the $\mu - e$ cross section in the improved Born approximation and includes, by definition, the running of α. This physical observable within the electroweak Standard Model is precisely known. For convenience $d\sigma^B/dt$ can be decomposed into the contributions arising from the t channel (B_t), the s channel (B_s) and their interference (B_i):

$$\frac{d\sigma^B}{dt} = \frac{\pi\alpha_0^2}{2s^2} Re\left\{B_t + B_s + B_i\right\}$$

where

$$\begin{aligned} B_t = \left(\frac{s}{t}\right)^2 \Bigg\{ & \frac{5+2c+c^2}{(1-\Pi(t))^2} + \xi\frac{2(g_v^2+g_a^2)(5+2c+c^2)}{(1-\Pi(t))} + \\ & +\xi^2\left(4(g_v^2+g_a^2)^2 + (1+c)^2(g_v^4+g_a^4+6g_v^2g_a^2)\right)\Bigg\} \end{aligned}$$

$$\begin{aligned} B_s = & \frac{2(1+c^2)}{\mid 1-\Pi(s)\mid^2} + 2\chi\frac{(1-c)^2(g_v^2-g_a^2)+(1+c)^2(g_v^2+g_a^2)}{1-\Pi(s)} + \\ & +\chi^2\left[(1-c)^2(g_v^2-g_a^2)^2 + (1+c)^2(g_v^4+g_a^4+6g_v^2g_a^2)\right] \end{aligned}$$

$$\begin{aligned} B_i = 1\frac{s}{t}(1+c)^2 \Bigg\{ & \frac{1}{(1-\Pi(t))(1-\Pi(s))} + \\ & + (g_v^2+g_a^2)\left(\frac{\xi}{1-\Pi(s)} + \frac{\chi}{1-\Pi(t)}\right) + \\ & + (g_v^2+6g_v^2g_a^2+g_a^4)\xi\chi\Bigg\} \end{aligned}$$

Where

$$\chi = \frac{s}{s-m_z^2+im_z\Gamma}\cdot\frac{1}{\sin 2\theta_w}$$

$$\xi = \frac{t}{t-m_z^2}\frac{1}{\sin 2\theta_w}$$

$$g_a = -\frac{1}{2},\ g_v = -\frac{1}{2} + 2\sin^2\theta_w$$

$$t = (p_1-q_1)^2 = -\frac{1}{2}s(1-c)$$

$$c = \cos\theta,\ \theta = \mathbf{p}_1\hat{\mathbf{q}}_1$$

Where s is the total squared invariant mass, θ_w the Weinberg mixing angle and θ the scattering angle between the initial and final lepton with momenta $\mathbf{p}_1$ and $\mathbf{q}_1$ respectively.

- The **running of** α in the space-like and time-like regions is represented by the two functions $\Pi(s) = \Delta\alpha(s)$ and $\Pi(t) = \Delta\alpha(t)$. More precisely one can write, in terms of the fermion-loop insertions into the virtual photon lines [3]:

$$\Pi(t) = \frac{\alpha_0}{t}\left(\delta_t + \frac{1}{3}L - \frac{5}{9}\right) + \\ + \left(\frac{\alpha_0}{\pi}\right)^2\left(\frac{1}{4}L + \zeta(3) - \frac{5}{24}\right) + \\ + \left(\frac{\alpha_0}{\pi}\right)^3 \Pi^{(3)}(t) + \mathcal{O}\left(\frac{m_e^2}{t}\right)$$

  where

$$L = \ln\frac{Q^2}{m_e^2},\ Q^2 = -t,\ \zeta(3) = 1.202$$

  The term $\Pi^{(3)}(t)$ represents the third-order (three-loop) leptonic contributions to the vacuum polarization.

- For what concerns our measurement of the α running using $\mu - e$ scattering, the **radiative factor** 1+$\Delta r(t)$ has been proved to be negligible [3], [4] as well as the following contributions:
  - Any electroweak effect beyond tree level, for instance appearing in boxes or vertices with Z^0 and W bosons, running weak coupling, etc.;
  - Box diagrams at order α^2 and larger;
  - Contributions of order α^2 without large logarithms, leading from order α^4 and subleading higher order;
  - Contributions from pair-produced hadrons, muons, taus and the corresponding virtual corrections to the vertices.

2

MUON $g-2$

2.1 THE MUON

The muon was observed for the first time in a Wilson cloud chamber by Kunze in 1933, but it was reported to be "a particle of uncertain nature". In 1936 Anderson and Neddermeyer discovered the presence of "particles less massive than protons but more penetrating than electrons" in cosmic rays. In 1943 Rossi and Nereson measured the lifetime of these particles to be $\tau \simeq 2.15 \pm 0.1 \mu s$, assuming it was the carrier of the nuclear force predicted by the Yukawa's theory. Eventually it was understood that cosmic rays consist of two different particles: the pion π, which actually it Yukawa's particle, and the muon μ. The latter is obtained from the former by weak decay $\pi^- \rightarrow \mu^- \nu_\mu$. The muon is a second generation lepton, with a mass about 207 times the electron's. Like the electron, the muon obeys QED, and can interact with other particles through the electromagnetic and weak forces. Unlike the electron, the muon decays through the weak force predominantly by $\mu^- \rightarrow e^- \nu_\mu \bar{\nu}_e$. The muon's long lifetime of ∼2.2 μs permits precision measurements of its mass, lifetime, and magnetic moment.

Table 1: Principal properties of the muon as quoted in the Particle Data Group (PDG) [6].

μ Properties (PDG 18)	
J	1/2
m_μ	105.6583745 ± 0.0000024 MeV
τ	2.1969811 ± 0.0000022 μs
a_μ ($\times 10^{-10}$)	11659208 ± 54 ± 3.3

2.2 THE $g-2$ ANOMALY IN THE STANDARD MODEL

In the Standard Model, the muon anomaly a_μ gets measurable contributions from QED, the strong interaction and from the electroweak interaction:

$$a_\mu = a^{QED} + a^{Had} + a^{Weak} \tag{1}$$

The uncertainty on this observable is dominated by the contribution of virtual hadrons in loops. In the following we present the current state of art of theoretical calculations for each one of the terms in eq.(1).

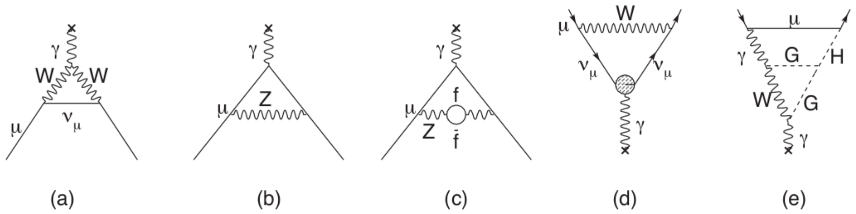

Figure 2: Weak contributions to the muon anomalous magnetic moment from [9]. Single loop contributions from: (a) virtual W and (b) virtual Z gauge bosons. These two contributions enter with opposite sign, and there is a partial cancellation. The two-loop contributions fall into three categories: (c) fermionic loops which involve the coupling of the gauge bosons to quarks, (d) bosonic loops which appear as corrections to the one-loop diagrams, and (e) a new class of diagrams involving the Higgs where G is the longitudinal component of the gauge bosons.

2.2.1 *QED contributions*

The QED contribution to a_μ is well understood. The present QED value, calculated for the full five-loop contribution, is

$$a_\mu^{QED} = 116584718.951(0.009)(0.019)(0.007)(0.077) \times 10^{-11}$$

where the uncertainties are from the lepton mass ratios, the eight-order term, the tenth order term, and the value of α taken from the ^{87}Rb atom [5] $\alpha^{-1}(\mathrm{Rb}) = 137.035999049(90)$ (0.66 ppb).

2.2.2 *Weak contributions*

The electroweak contribution has been completely calculated up to two-loops contributions [7], while the leading logs for the next-order term have been shown to be small [8]. Fig. 2 shows Feynman diagrams for the weak contributions to the muon anomalous magnetic moment. The one loop result, calculated shortly after G. 't Hooft showed the Glashow-Salam-Wienberg theory to be renormalizable, is

$$\begin{aligned} a_\mu^{EW(1)} = \frac{G_F}{\sqrt{2}} \frac{m_\mu^2}{8\pi^2} \left\{ \frac{10}{3} + \frac{1}{3}(1 - 4\sin^2\theta_W)^2 - \frac{5}{3} \right. \\ \left. \mathcal{O}\left(\frac{m_\mu^2}{M_Z^2} \log \frac{M_Z^2}{m_\mu^2}\right) + \frac{m_\mu^2}{M_H^2} \int_0^1 dx \frac{2x^2(2-x)}{1 - x + \frac{m_\mu^2}{M_H^2} x^2} \right\} = \\ = 19.8 \times 10^{-11} \end{aligned}$$

Only the W and Z bosons contribute at a measurable level in the lowest order electroweak term, as shown in Fig. 2. The two-loop contribution (Fig. 2(c-e)), has been re-evaluated recently using the

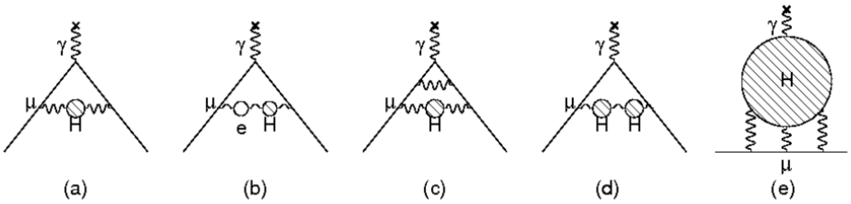

Figure 3: The hadronic contribution to the muon anomaly from [9], where the dominant contribution comes from the lowest-order diagram (a). The hadronic light-by-light is shown in (e).

LHC value of the Higgs mass [8]. The total electroweak contribution is

$$a_\mu^{EW} = (153.6 \pm 1.9) \times 10^{-11}$$

where the error comes from hadronic effects in the second-order electroweak diagrams with quark triangle loops, along with unknown three-loop contributions. The weak contribution is about 1.3 ppm of the muon g-2, so the experimental uncertainty on a_μ (BNL E821) of ± 0.54 ppm now probes the weak scale of the Standard Model.

2.2.3 *Hadronic contribution*

The hadronic contribution to a_μ is about 60 ppm of the total value and dominates the theoretical uncertainty on the muon anomalous magnetic moment. This category of contribution contains two phenomenologies: the hadronic vacuum polarization and the light-by-light effect. While the former dominates this contribution and its error, the latter is also important. Fig. 3 shows the Feynman diagrams of these processes. The energy scale for the virtual hadrons is of order $m_\mu c^2$, well below the perturbative region of QCD (pQCD). However the lowest order hadronic contribution can be calculated from the dispersion relation

$$a_\mu^{had;LO} = \left(\frac{\alpha m_\mu}{3\pi}\right)^2 \int_{m_\pi^2}^{\infty} \frac{ds}{s^2} K(s) R_{had}(s) \qquad (2)$$

where:

$$R_{had} \equiv \frac{\sigma_{tot}(e^+e^- \to \text{had.})}{\sigma(e^+e^- \to \mu^+\mu^-)}$$

using the measured cross sections for $e^+e^- \to$ had. as input, where $K(s)$ is a kinematic factor ranging from 0.4 at $s = m_\pi^2$ to 0 at $s = \infty$. The dispersive integral above is usually calculated the experimental value of $R_{had}(s)$ up to a certain value of s, and by using pQCD in the high-energy tails. The problem is that due to resonances (especially the ρ resonance) and threshold effects at low energies, $R_{had}(s)$ in the integrand is highly fluctuating. Fig. 4 depicts pictorially this calculation. The determination of $a_\mu^{had;LO}$ is dominated by the values

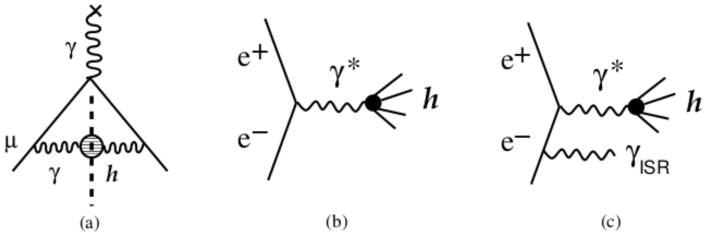

Figure 4: Pictorial display of the dispersion integral from [9]. (a) The "cut" hadronic vacuum polarization diagram; (b) The e^+e^- annihilation into hadrons; (c) Initial state radiation accompanied by the production of hadrons.

of R_{had} at low energies, as shown in Figure 5. The contribution is

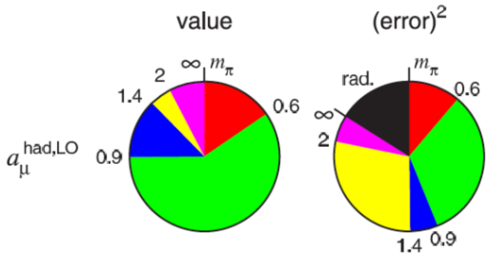

Figure 5: Contributions to the dispersion integral for different energy regions, and to the associated error squared on the dispersion integral in that energy region. Taken from Hagiwara et al. [10].

dominated by the 2π final state, but other low-energy multi-hadron cross sections are also important.

Recently two analyses [10] [11], using the newest compilation of experimental cross sections for $e^+e^- \to had.$, obtained:

$$a_\mu^{had;LO} = (6923 \pm 42) \times 10^{-11}$$

$$a_\mu^{had;LO} = (6949 \pm 43) \times 10^{-11}$$

respectively. The latest evaluation of the next-to-leading order hadronic contributions [10] shown in Fig. 3 is:

$$a_\mu^{had;NLO} = (-98.4 \pm 0.6_{exp} \pm 0.4_{rad}) \times 10^{-11}$$

2.2.4 *Hadronic light-by-light contribution*

The hadronic light-by-light contribution is depicted in Fig. 3(e). This term can not be determined from data, but rather must be extracted using hadronic models that correctly reproduce properties of QCD. Due to asymptotic QCD constraints, a full model independent evaluation is not possible at present. It should be stressed here that the difficulty in the evaluation of the HLbL effect does not come from theory but from the technical difficulty in the implementation of the model itself. The physics of the HLbL scattering contribution is well understood: theoretical predictions of a_μ^{HLbL} have been relatively stable for more than ten years now. The current value [12] for this contribution, obtained from a synthesis of different models, which was agreed to by authors from each of the leading groups that have been working in this field, is

$$a_\mu^{HLbL} = (105 \pm 26) \times 10^{-11}$$

2.2.5 *The SM value of* $g-2$

The current state of art of the theoretical prediction on a_μ highly depend on the reference used to calculate the lowest-order hadronic contribution. The two most accurate calculations present in literature at the moment are from Davier, et al. [11] and from Hagiwara et al., [10]. The higher-orders hadronic contribution is currently taken from [11]. Table 2 presents a summary of the different contributions which sum up to a_μ as defined in eq. (1).

Contribution	Value ($\times 10^{-11}$)
QED ($\gamma + l$)	$116584718.951 \pm 0.009 \pm 0.019 \pm 0.007 \pm 0.077$
HVP (lo) [10]	6923 ± 42
HVP (lo) [11]	6949 ± 43
HVP (ho) [11]	-98.4 ± 0.7
HLbL	105 ± 26
EW	154 ± 1
Total SM [10]	$116591802 \pm 42_{\text{H-LO}} \pm 26_{\text{H-HLO}} \pm 2_{\text{other}}$ ($\pm 49_{\text{tot}}$)
Total SM [11]	$116591828 \pm 43_{\text{H-LO}} \pm 26_{\text{H-HLO}} \pm 2_{\text{other}}$ ($\pm 49_{\text{tot}}$)

Table 2: Standard Model value of the muon anomalous magnetic moment. The two different values depend on the two most precise calculations of the lowest-order hadronic vacuum polarization contribution from [10], [11].

Where the QED calculation is from Aoyama [13]; the electroweak contribution from Miller, et al. [14] and the hadronic light-by-light effect is from the model currently agreed on, known as "Glasow Consensus" [15].

2.3 MEASURING THE MUON ANOMALY

The muon anomalous magnetic moment was measured with three experiments at CERN and by the E821 collaboration at the Brookhaven National Laboratory. In this section we present a brief overview of these experiments with a more detailed description of E821, which

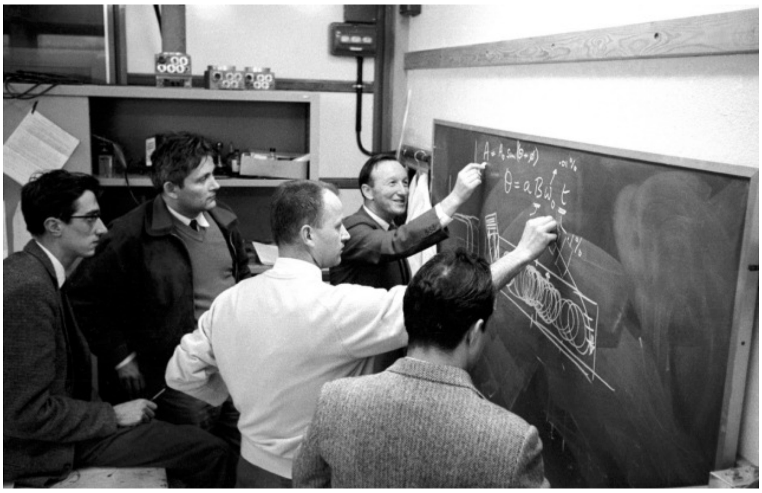

Figure 6: Blackboard interpretations of the g-2 experiment of the SC at CERN. Muller and Farley at blackboard, J.C. Sens and A. Zichichi on the extreme left and right and G. Charpack in far background.
Image from CERN© archives , all rights reserved.

measured the muon g-2 with a precision of 0.54 ppm: currently the most precise experimental value for this observable.

2.3.1 *CERN-I*

Acting on an idea of Leon Lederman, CERN launched the g-2 experiment in 1959, aimed at measuring the muon magnetic moment. Six physicists joined forces in the same year to measure this value on CERN's first accelerator, the Synchrocyclotron. The first experiment at CERN to measure the muon anomalous magnetic moment was performed in 1961. In this case muons were injected into a 6 meters long straight magnet where they followed a drift spiral path, traversing the magnet because of a small gradient introduced in the field. Using a polarimeter to stop the muons outside the magnet and measuring their net spin precession, a_μ was determined with an uncertainty of 4300 ppm. The result agreed with the prediction of QED for structureless particles. This experiment opened a new field of research and the muon g-2 began to raise high interest for its properties and for the possibility to be used for precision tests of QED. In particular, the CERN-I experiment tested with a 95% confidence level that conventional quantum electrodynamics is applicable to distances as small as 7×10^{-14} cm and that the "radius" of the muon is less than 4.5×10^{-14} cm.

2.3.2 *CERN-II*

In the second experiment at CERN (1962-1968) was used a magnetic ring to extend the muon storage time. Muons were obtained using a

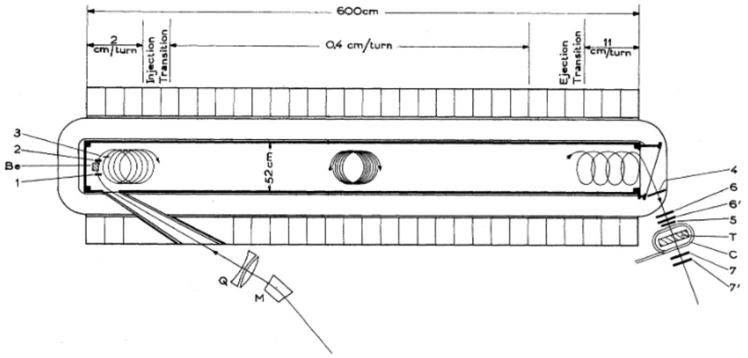

Figure 7: General plan of the 6-m magnet from the CERN-I experiment. Q, M are quadrupoles and bending magnet respectively. On the right Be-moderator and counters for injected protons. On the left T: methylene-iodide target and counters for "backward" and "forward" electrons. Image from [16].

primary proton beam which was injected directly onto a target inside the storage ring where produced pions decayed. Only a small fraction of the muons produced in this manner fell onto stable orbits. The result to 270 ppm agreed with QED.

2.3.3 *CERN-III*

The last experiment conducted at CERN could count on the experience gained with the second one and on the recent theoretical improvements. In fact it was clear, from the calculations by Gourdin and de Rafael, that the muon anomaly had contributions also from the strong interaction and the previous experiment was just on the verge of seeing this effect. Moved by all these motivations a collaboration started to work on the new storage ring which started its operations in the 70's.
The CERN-III (1974-1976) experiment used a uniform-field storage ring and electric quadrupoles to provide vertical containment for muons. This focusing was specific for muons with momentum of 3.1 GeV/c, defined as *magic momentum*: in fact, at this value the muon spin precession is not affected by the electric field from the quadrupoles. Instead of protons, pions were injected directly into the storage ring to reduce background and to increase the fraction of stored muons. The CERN-III experiment achieved a precision of 10 ppm for each muon polarity. The results were combined to give a 7.3 ppm measurement, in agreement with theory. Moreover, this result served as the first confirmation of the predicted 60 ppm contribution to a_μ from hadronic vacuum polarization.

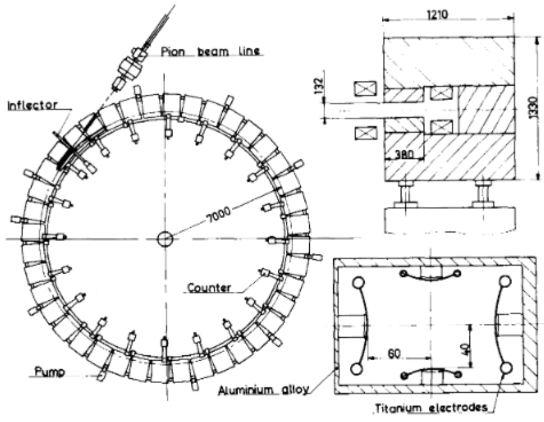

Figure 8: Plan view of the 14m diameter magnet which formed the second muon storage ring at CERN. On the right cross sections of magnet and quadrupoles are shown. Image from [17].

2.3.4 *BNL E821*

The complete standard model value of the muon anomalous magnetic moment, currently known to a precision of 0.54 ppm, was measured by the E821 experiment at Brookhaven National Laboratory (BNL). E821 followed the same general technique as CERN-III, but with consistent improvements. It used a continuous superconducting magnet, instead of a lattice of discrete resistive magnets. A direct current inflector magnet permitted the ring to be filled at 33 ms intervals, matching the bunch extraction from the AGS. Muons were injected directly in the storage ring, increasing the storage efficiency and reducing the intense hadron background. Muons were placed and centred on stable orbits by a pulsed kicker. Combining the results of four positive muon runs taken from 1997 to 2000 and a final run using negative muons, a_μ was determined to a precision of 0.54 ppm. In the following we give an overview of the experimental technique used at E821, as the recent "g-2" experiment in program at Fermilab for the next years plans to use the same apparatus as well as an analogous technique.

2.3.4.1 *Experimental method*

The muon g-2 can be extracted measuring the anomalous precession frequency ω_a, id est the rate at which the polarization turns relative to the momentum. For a muon moving in the horizontal plane of a magnetic storage ring, the cyclotron ω_c and spin precession ω_s frequencies are given by:

$$\vec{\omega}_c = -\frac{Qe\vec{B}}{m\gamma}, \; \vec{\omega}_s = -\frac{gQe\vec{B}}{2m} - (1-\gamma)\frac{Qe\vec{B}}{m\gamma}$$

The quantity ω_a is determined from the difference

$$\vec{\omega}_a = \vec{\omega}_s - \vec{\omega}_c = -\left(\frac{g-2}{2}\right)\frac{Qe\vec{B}}{m} = -a_\mu \frac{Qe\vec{B}}{m} \tag{3}$$

Equation (3) describes the anomalous precession frequency in case of no electric field applied. In reality muons in the rest frame see the electric field of quadrupoles used to provide vertical focusing in the storage ring and this can affect the spin precession frequency. Hence in presence of an electromagnetic field, in case that $\vec{\beta}$ is perpendicular to both the fields, eq. (3) becomes

$$\vec{\omega}_a = -\frac{Qe}{m}\left[a_\mu \vec{B} - \left(a_\mu - \frac{1}{\gamma^2 - 1}\right)\frac{\vec{\beta} \times \vec{E}}{c}\right] \tag{4}$$

E821 as well as CERN-III operates at the specific μ momentum of 3.094 GeV/c, the so called *magic*. At this value the coefficient of the term $\vec{\beta} \times \vec{E}$ vanishes and the anomalous precession frequency only depends on the magnetic field applied, which was uniform in the case of E821 experiment. The magnetic field $\vec{B}$ used in eq. (4) is the average over muon trajectories during the course of the experiment, weighted with magnetic field distribution. Thus, a_μ can be extracted by measuring ω_a and the value of the field normalized to the Larmor frequency of a free proton ω_p:

$$a_\mu = \frac{\omega_a/\omega_p}{\lambda_+ - \omega_a/\omega_p} = \frac{\mathcal{R}}{\lambda_+ - \mathcal{R}}$$

The quantity λ_+ is the muon-to-proton magnetic moment ratio

$$\lambda_+ = \frac{\mu_{\mu^+}}{\mu_p} = 3.183345137(85)$$

determined from muonium hyperfine level structure measurements assuming CPT invariance.

The E821 experiment was commissioned in 1997 using the same pion injection technique employed by the CERN-III experiment. Data were obtained in typical 3/4 months annual runs through 2001. The final experimental result obtained from the BNL experiment is

$$a_\mu(E821) = 11659208.0(6.3) \times 10^{-10} \text{ (0.54 ppm)}$$

At present this is the most accurate measurement of the muon anomalous magnetic moment and it ultimately is limited by statistics. New experiments at Fermilab and J-PARC, aiming at measuring the muon g-2 to a precision of 1.6×10^{-10} (0.14 ppm), are underway [1], [19]. In the final report of the BNL E821 experiment the collaboration stated that

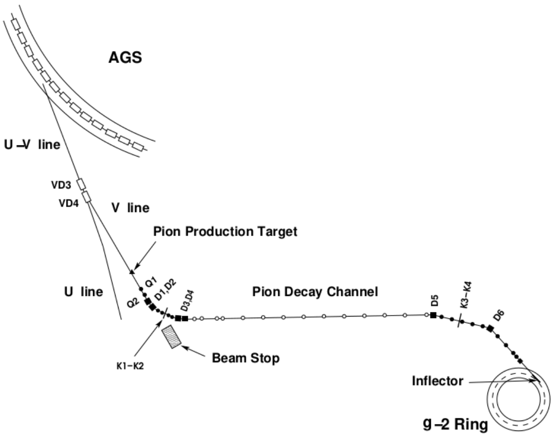

Figure 9: Plan view of the pion/muon beamline. The pion decay channel is 80 m and the ring diameter is 14.1 m. Image from [18].

> *The precision on the SM value will be improved, enabling a more sensitive comparison with experiment.*

SM theoretical development has progressed, with QED loops evaluated through fourth order and estimated through fifth, weak loops through second order and hadronic loops through second order as well. The current status of the SM prediction has been presented in section 2.2.5 and the final comparison with experiment gives

$$\Delta a_\mu(E821-SM) = \begin{array}{l} (287 \pm 80) \times 10^{-11} \;\; [10] \\ (261 \pm 78) \times 10^{-11} \;\; [11] \end{array}$$

depending on which evaluation of the lowest-order hadronic contribution that is used. This comparison between the experimental values and the present SM value is shown graphically in Fig. 10. The discrepancy between the SM expectation from [10], [11] and experimental value corresponds to a 3.3-3.6σ deviation. While, at a level of 3σ, one can not speak of a firmly established deviation from the SM prediction, all different contributions have been checked thoroughly. As pointed out many times so far, the SM value is expected to be improved in the hadronic data and it seems increasingly difficult to explain the discrepancy by a change in this sector alone. In the following section we present in more detail the state of art of the a_μ^{HLO} evaluation explaining how data required as input in eq. (2) are obtained and how more recent calculations from [23] improved this value, leading to a 3.7σ discrepancy between the SM expectation and the E821 measurement.

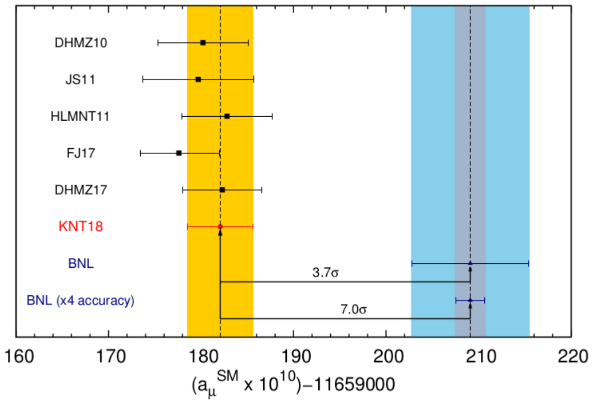

Figure 10: Comparison between $a_\mu^{SM}$and a_μ^{Exp}. DHMZ10 is Ref. [11], JS11 is Ref. [20], HLMNT11 is Ref. [10], FJ17 [21] and DHMZ17 [22]. KNT18 from Ref. [23] is the same central value with a reduced error obtained by recent improvement on the hadronic cross section measurement; "BNL" is the current experimental value of a_μ; "BNL (x4 accuracy)" is the same central value with a fourfold improved precision as planned by the future $(g-2)$ experiments at Fermilab and J-PARC [19].

2.4 LEADING-ORDER HADRONIC CONTRIBUTION TO THE MUON $g-2$

The hadronic contribution to the muon anomalous magnetic moment can be divided into the lowest order (LO) and higher orders (HO) vacuum polarization (VP) terms and the hadronic light-by-light effect

$$a_\mu^{Had} = a_\mu^{LOVP-Had} + a_\mu^{HVP-Had} + a_\mu^{HLbL}$$

The first term accounts for 60 ppm to a_μ, while the higher orders term and the hadronic light-by-light effect have relatively less impact on the final value of the muon g-2, being of an order $\mathcal{O}(\alpha^3)$. The lowest-order contribution can be evaluated exploiting the dispersion relation given in eq. (2). However in the SM, none of the contributions which define a_μ^{had} can be calculated reliably using perturbative QCD (pQCD), as virtual photons with low q^2 dominate the loop integrals. Figure 5 pictorially depicts this situation. At present a precision of 1% is required on a_μ^{HLO} to substantially improve the SM prediction on the muon anomalous magnetic moment. To achieve this precision it is mandatory to exploit and combine the best measurements available for $e^+e^- \rightarrow \gamma^\star \rightarrow had$. We recall the dispersion relation (2)

$$a_\mu^{had;LO} = \left(\frac{\alpha m_\mu}{3\pi}\right)^2 \int_{m_\pi^2}^{\infty} \frac{ds}{s^2} K(s) R_{had}(s)$$

which depends on the kernel function $K(s)$

$$K(s) = \frac{m_\mu^2}{(3\pi)^2}(0.4\ldots1) = \int_0^1 dx \frac{x^2(1-x)}{x+(1-x)\frac{s}{m_\mu^2}}$$

which increases monotonically from $s=0.4$ to $s=1$. Hence, low energy region weights more in the evaluation of the integral (2), making the $\rho \rightarrow 2\pi$ channel the most dominant (∼70%) in the evaluation of a_μ^{HLO}. This effect reflects directly on the $R_{had}(s)$-dependence of the integral, as it is necessary to have extremely precise measurements of undressed total hadronic cross sections as input for the calculation. Experimentally two methods are used to measure the hadronic cross sections: the energy scan (Fig. 5(b)), and the radiative return method, which uses initial state radiation with a fixed beam energy to measure the cross section for energies below the total center-of-mass energy of the colliding beams (Fig. 5(c)). Several experiments around the world employ these two techniques to provide precision measurements of $\sigma(e^+e^- \rightarrow had.)$. The CMD2, and the more recent CMD3, detector at Novosibirsk and the BESIII experiment at the Beijing tau-charm factory BEPC-II us the energy scan method, while the KLOE collaboration, BaBar and BELLE ectract bare hadronic cross sections from radiative return analysis. Combining the two approaches precision measurement in the ρ region have been recently provided as input to SM calculations for a_μ^{HLO}. As pointed out above, the $\rho \rightarrow 2\pi$ channel dominates the lowest-order contribution, hence a precise agreement between different experimental values is fundamental to improve the current theoretical prediction. The most recent results from KLOE [24] agreed fairly well with the measurements from CMD-2 and SND (Novosibirslk) [25], but they present slight disagreement with data obtained from radiative return analysis from BaBar [26]. This tension has prevented a grater improvement of the error in the ρ region. In addition to this region many other exclusive channels have been measured from these experiments and an extensive compilation of $R(s)$ values [10] has been used for calculations over the past years. Results presented in section 2.2.3 for the two a_μ^{HLO} values from [10], [11] for the SM calculation of a_μ led to a 3.3-3.6σ deviation from the experimental value which did not undergo to substantial improvements. The pie diagram in Fig. 5 shows that the dominant contribution to the LO hadronic vacuum-polarisation correction to g-2 comes from the e^+e^- energy region up to 0.9 GeV, whereas the major part of the error comes from the region up to 2 GeV. A more recent work from Keshavarzi et al. [23] has used a new data combination method which led to a new evaluation of a_μ^{HLO}. Figure 11a shows the new compilation of the total hadronic $R(s)$ ratio from different final states. These values have been recalculated by [23] using more recent measurements of bare hadronic cross sections. The authors could exploit new data from the KLOE collaboration [27], [28] and from the BESIII [29] which combined with the BaBar results [26] permitted an improvement on the calculation of the total contribution of a_μ^{HLO}

$$a_\mu^{HLO} = (693.27 \pm 2.46_{\text{tot}}) \times 10^{-10}$$

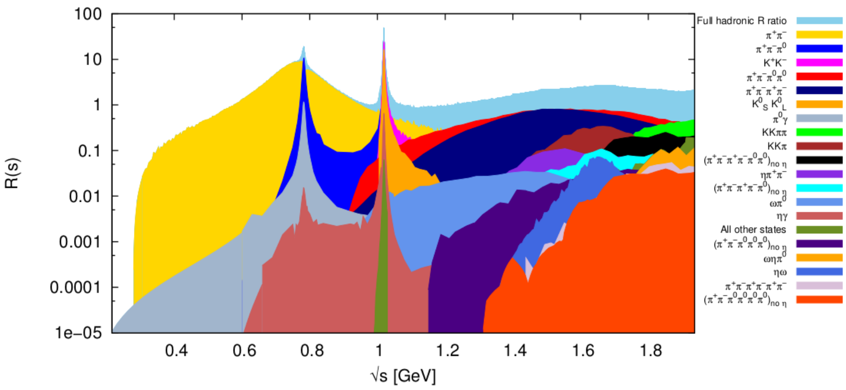

(a) Contributions to the total hadronic R ratio from different final states. Yellow histogram is the final state of 2π.

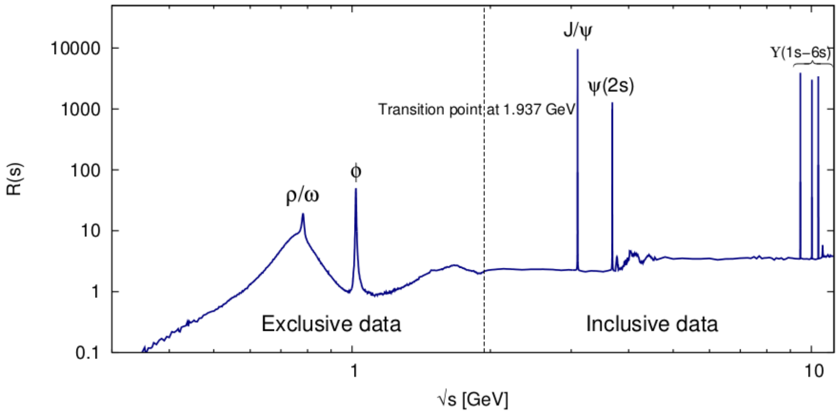

(b) Hadronic R-ratio shown in the range $m_\pi \leq \sqrt{s} \leq 11.1985$ GeV distinguishing exclusive data from inclusive ones. Prominent resonances are labelled.

Figure 11: The total hadronic R ratio from [23]. At present this is the best compilation in literature.

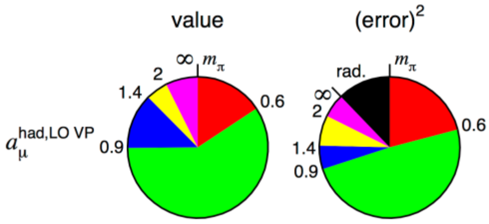

Figure 12: New values of the contributions to the dispersion integral shown in Fig. 5. Pie diagram from [23] obtained using new data from KLOE [27], [28] and BESIII [29].

This recent improvement in a_μ^{HLO} calculation sets more precise values on the fractional contributions to the total mean value of eq.(2) as shown in Fig. 12. Combining this result with the contributions from QED and the electro-weak sector, high order hadronic contributions and light-by-light effect the SM prediction of the anomalous magnetic moment of the muon was found to be

$$a_\mu^{SM} = (11659182.05 \pm 3.56) \times 10^{-10}$$

When compared to the current experimental measurement it results in a deviation of $\Delta a_\mu = (27.05 \pm 7.26) \times 10^{-10}$, corresponding to a 3.7σ discrepancy.

2.4.1 *The running of α_{em} from $R(s)$*

In section 1.2 we have seen the theory behind the scale dependence of the QED coupling constant. In particular, we have shown its dependence both from leptonic and hadronic vacuum polarisation effects that screen the electric charge

$$\alpha(q^2) = \frac{\alpha}{1 - \Delta\alpha_{lep}(q^2) - \Delta\alpha_{had}(q^2)}$$

We have also underlined the importance of knowing the value of α_{em} at the scale of the mass of the Z boson, $\alpha(M_Z^2)$. In fact, it is needed for predictions of high-energy processes and it is fundamental for precision tests of the EW sector in the SM. Due to the hadronic uncertainties ($\Delta\alpha_{had}(q^2)$), it is the least well known of the EW SM parameters. In section 1.2 we mentioned the possibility to evaluate the hadronic contributions of the QED coupling exploiting dispersion integral. More precisely, using the same compilation of hadronic data needed to evaluate a_μ^{HLO}, combined with pQCD, it is possible to calculate with the best possible precision $\Delta\alpha_{had}(q^2)$ via the following dispersion integral

$$\Delta\alpha_{had}(q^2) = -\frac{\alpha q^2}{3\pi}\mathcal{P}\left(\int_{s_{th}}^{\infty} \frac{R_{had}(s')ds'}{s'(s'-q^2)}\right) \tag{5}$$

where $\mathcal{P}$ denotes the principal value of the integral. Hence, a precise evaluation of the lowest order hadronic contributions to the muon anomalous magnetic moment directly lead to the possibility of evaluating also the hadronic vacuum polarisation effects on α_{em}. The recent work from Keshavarzi also re-evaluated this quantity, previously stable at the values calculated in [10], [11], using the new compilation of total hadronic $R(s)$ ratio (Fig. 11b). The total value of the QED coupling at the Z boson mass is found to be

$$\alpha^{-1}(M_Z^2) = 128.946 \pm 0.015 \text{ [23]} \tag{6}$$

3

THE MU-ON-E EXPERIMENT

The MUonE experiment aims to measure the leading-order hadronic contributions to the muon anomalous magnetic moment with a statistical precision of 0.3%. In section 2.2.3 and more in details in section 2.4 we have outlined the usual way of calculating this term using a time-like dispersion integral. We pointed out that the most critical aspect of using eq.(2) to evaluate a_μ^{HLO} is the knowledge of the bare hadronic cross sections, especially in the low energy range where one cannot rely on pQCD. The present compilation of $R(s)$ allows a determination of the leading hadronic contribution with an uncertainty of the order of 0.4-0.5%. However since the estimate of systematic uncertainties coming from this method is extremely delicate, a cross-check based on independent techniques is needed. In section 2.4.1 it has been observed the strict link between the QED coupling and the muon anomalous magnetic moment, as there is the possibility to compute both of them in a time-like approach using a compilation of e^+e^- annihilation data (eg. Fig. 11b). The MUonE idea is competitive and complementary with this one, aiming to determine a_μ^{HLO} from a measurement of the effective electromagnetic coupling constant in the space-like region using a $\mu - e$ scattering process. In the following is detailed the project of this innovative experiment, as well as the theoretical framework on which it relies.

3.1 THEORETICAL FRAMEWORK

The time-like dispersion integral presented in section 2.2.3 has been commonly used during the past years to evaluate the leading order hadronic contributions to the muon g-2. However eq.(2) presents limitations:

- The integrand function $R(s)$ is highly fluctuating, especially at low energies, due to resonance and threshold effects (see Fig.11a);
- The integral has to be calculated using experimental values of $R_{had}(s)$ in the low energy tails and perturbative QCD in its high energy component

Alternatively a_μ^{HLO} can be calculated exploiting an alternative formula in the space-like region [30], namely

$$a_\mu^{HLO} = \frac{\alpha}{\pi} \int_0^1 dx (1-x) \Delta\alpha_{had}[t(x)] \tag{7}$$

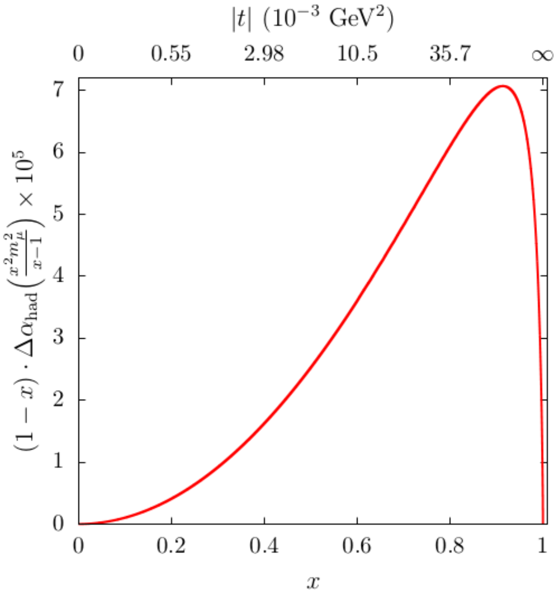

Figure 13: Integrand $(1-x)\Delta\alpha_{had}[t(x)] \times 10^5$ as a function of x and t from [31]. The peaks are $x_{peak} \simeq 0.914$ and $t_{peak} \simeq -0.108$ GeV^2.

where

$$t(x) = \frac{x^2 m_\mu^2}{x-1} < 0$$

is a space-like squared four-momentum and $\Delta\alpha_{had}(t)$ is the hadronic contribution to the running of the QED coupling, as already discussed in sections 1.2, 2.4.1. The main advantage of this expression with respect to the dispersion integral (2) is that the integrand function used here is smooth and free of resonances and can be extracted from data. Fig. 13 graphically shows the t and x dependence of the integrand in eq.(7).

In section 2.4.1 we have outlined how to extract the value of $\Delta\alpha_{had}(t)$ from bare hadronic cross section measurements, stressing the intrinsic difficulty and limitation of this method. An innovative technique which aims to extract this observable from small angle Bhabha scattering has been recently proposed in [30], similarly to what was done at LEP and documented in [3]. With this technique it would be possible to extract a measurement of a_μ^{HLO} from space-like data competitive with the current time-like evaluations. However, the use of Bhabha scattering data has some intrinsic limitations:

- Inevitable mixing of s and t channels leads to a non-trivial numerical procedure to extract $\Delta\alpha_{had}(t)$ from data;

- It follows that the precision on $\Delta\alpha_{had}(s>0)$ can limit theoretical accuracy of the a_μ^{HLO} prediction;

- There is the need of another process, independent from $\Delta\alpha_{had}(t)$ and known with high-accuracy, to normalize for systematic errors cancellation. Two possible processes could be:
  - The $e^+e^- \to \gamma\gamma$ at least up to next-to-next-leading order, but it is difficult to control with needed accuracy;
  - The Bhabha scattering itself at $t \sim 10^{-3}$ GeV^2 ($x \sim 0.3$), where the dependence of $\Delta\alpha_{had}$ is of $\mathcal{O}(10^{-5})$ and can be safely neglected. The main difficulty using this process is the impossibility to adapt current experiments with a suitable luminometer to achieve the needed precision and to avoid acceptance problems.

The MUonE project is an innovative technique to determine a_μ^{HLO} from the measurement of $\Delta\alpha_{had}(t)$ in the space-like region, without having to deal with these problems.

3.2 EXPERIMENTAL PROPOSAL

The innovative technique proposed by the MUonE experiment consist of using a muon beam with $E_\mu \simeq 150$ GeV scattering on a atomic electrons of a low-Z target. Thus, we intend to determine a_μ^{HLO} from eq.(7) using experimental measurement of $\Delta\alpha_{had}(t)$. The use of the $\mu e \to \mu e$ process is extremely appealing for the following reasons:

- It is a pure t-channel process and the t-dependence of the differential cross section is proportional to $\mid \alpha(t)/\alpha(0) \mid^2$:

$$\frac{d\sigma}{dt} = \frac{d\sigma_0}{dt}\left|\frac{\alpha(t)}{\alpha(0)}\right|^2$$

- The closed kinematics of the two bodies scattering allows to write the Mandelstam's variables s and t as

$$t = (p_\mu^i - p_\mu^f)^2 = (p_e^i - p_e^f)^2 = 2m_e^2 - 2m_e E_e^f,$$

$$s = (p_\mu^f + p_e^f)^2 = (p_\mu^i + p_e^i)^2 = m_\mu^2 + m_e^2 + 2m_e E_\mu^i$$

  where

$$E_e^f = m_e \frac{1 + r^2\cos^2\theta_e}{1 - r^2\cos^2\theta_e}, \; r^2 \equiv \frac{(E_\mu^i)^2 - m_\mu^2}{(E_\mu^i + m_e)^2}$$

- It follows that for $E_\mu^i = 150$ GeV, $s \simeq 0.164$ GeV^2 and -0.143 GeV$^2 \leq t < 0$GeV or, equivalently, $0 < x \leq 0.93$: meaning that t spans the peak region (see Fig. 13), corresponding to an electron scattering angle of $\theta_e^f \simeq 1.5$ mrad;

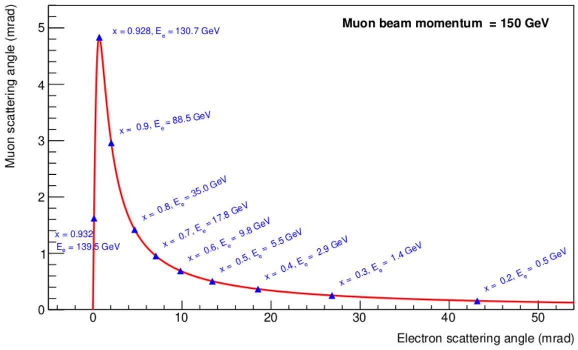

Figure 14: Elastic scattering theoretical curve: muon and electron scattering angles for 150 GeV incoming muons.

- The electron scattering angle θ_e^f spans the range (0-31.85) mrad for the energy E_e^f in the range (1-139.8) GeV. The boosted kinematicks of the collision guarantees that the scattering angles are completely contained in the acceptance of a single detector element in the laboratory system. This implies that many *systematic errors will cancel out* in the relative ratios of event counts in the high and low q^2 regions (signal and normalization regions);
- There is a kinematical correlation between the angle of the final scattered electron and muon, as shown in Fig. 14 from [31]. This constraint turns out to be extremely useful when selecting elastic events, rejecting background from radiative or inelastic processes.

We expect to achieve a ∼0.3% statistical precision on a_μ^{HLO} after two years of data taking, using $\sim$ 30 experimental points in x and a muon beam of 150 GeV with an average intensity of $\sim 1.3 \times 10^7\ \mu/s$. The choice of a 150 GeV muon beam has several advantages. First of all allows to design an apparatus which consists of series of a simple module, each one working as a standalone detector. The use of low-Z targets reduces the rate of multiple scattering of the final particles and other possible μ interactions, such as pair production and bremsstrahlung. Moreover there is the great advantage of using the $\mu e \to \mu e$ process itself for the final normalization. More precisely we intend to use the region $x \lesssim 0.3$ for the normalization since here the hadronic corrections to α are negligible. By exploiting the same process we expect that the theoretical uncertainties will be reduced to the level of $\mathcal{O}(10^{-5})$. Using 150 GeV muons we cover a region which accounts for $\sim$ 87% of the integral and fully contains the peak of the integrand in eq.(2) (see Fig. 13), which is at $x_{Peak} = 0.914$ ($t_{Peak} \simeq -0.108$ GeV^2) corresponding to $\Delta\alpha_{had}(t_{Peak}) \simeq 7.86 \times 10^{-4}$. The missing region ($0.932 \lesssim x \leq 1$) can be covered with pQCD calculations, by the use of time-like data and with lattice QCD calculations.

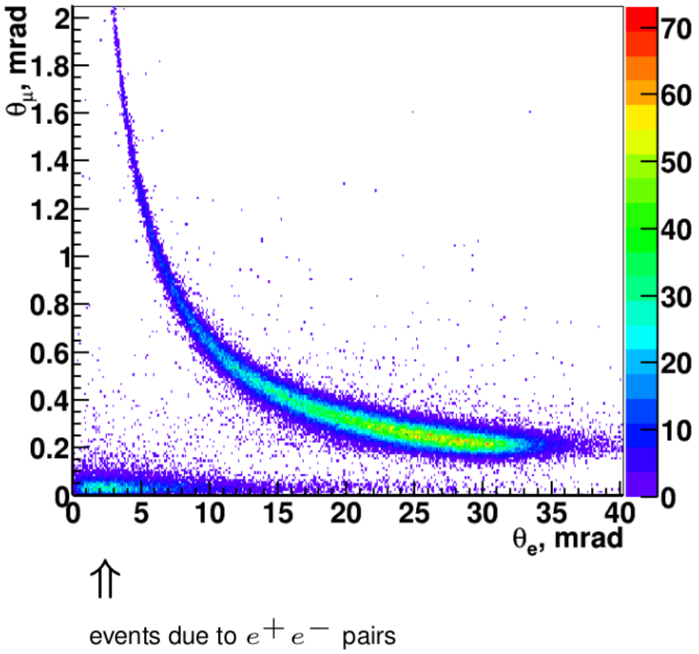

Figure 15: Scatter $\theta_e - \theta_\mu$ plot for 150 GeV muons. Scatter plot of Fig. 14 produced with theoretical NLO generator. Plot from C. C. M. Calame, *International Symposium-Advanced Dark Matter and Particle Physics*

3.2.1 *Detector set-up*

The boosted kinematics constrains the scattering within the forward direction, so that the transversal dimensions of the detector can be limited, e.g. of the order of $\sim 10 \times 10$ cm^2. The strategy to extract the final measurement of a_μ^{HLO} from eq.(7) can be summarized as follows:

- Measure the differential cross section of the $\mu - e$ scattering in the allowed kinematic range;
- Extract large values of $\mid t \mid$ from perturbative QCD (pQCD) and time-like data;
- Obtain a measured value of $\Delta\alpha_{had}(t)$ from a fit of the experimental points at the measured $\mid t \mid$ values;
- Use this value of $\Delta\alpha_{had}(t)$ to derive the leading hadronic corrections to a_μ from eq.(7).

Fig. 16 gives an example with pseudo-data of the strategy described above. Collecting $\sim$ 30 value of $\Delta\alpha_{had}(t)$ we intend to extract the value of the integrand in eq. (7) from a fit and to use it to retrieve a measurement of a_μ^{HLO}. We intend to perform this measurement with a dedicated detector which will measure:

- The direction and momentum of the incident beam;

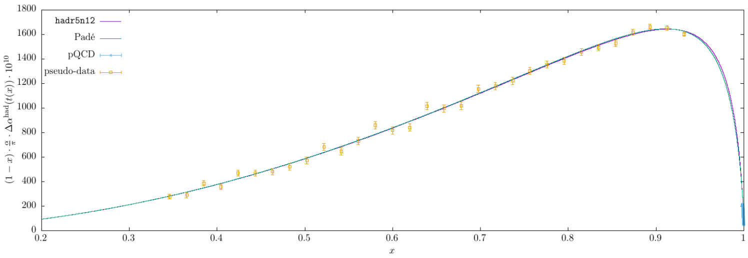

Figure 16: Pictorial representation of the distribution of the integrand in eq. (7). Final measurement of a_{μ}^{HLO} is intended to be extracted from a theoretical fit of this distribution. Image by Carlo C.M. Calame.

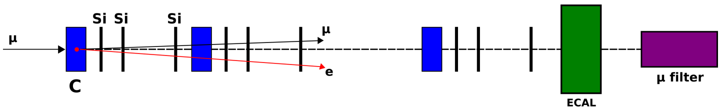

(a) Schematic view of the final apparatus set-up.

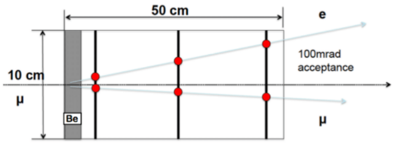

(b) Detailed view of a single module.

Figure 17: 17a schematic view of the final detector. Eventually we plan to use 20 modules, as the one shown in 17b.

- Outgoing particle directions.

As stated above, we plan to use a 150 GeV muon beam with an intensity rate of $\sim 1.3{\times}10^{7}\mu/s$. Such a beam is available at CERN and has the characteristics needed for such a measurement. In fact it provides both positive and negative muons and has a very small electrons contamination.

We plan to use a modular apparatus consisting of a low-Z target and two silicon tracking stations located at a distance of one meter. The detector should consist of 60 modules and possibly two downstream particle identifiers: an electromagnetic calorimeter and a muon detection system. These are fundamental to avoid ambiguities in the reconstruction of tracks with small scattering angles (θ_e, θ_μ below 5 mrad). Fig. 17 shows a scheme of the planned detector layout. As previously mentioned, the advantages of such a detector are several: it allows to cover almost entirely the acceptance of the elastic interaction. It can achieve extremely precise angular resolution (~0.02 mrad) and it covers both the signal and the normalization regions.

4

TEST BEAM ANALYSIS

In order to prove the feasibility of the final experiment we had two test beams in the past year. The first test beam was performed in October 2017 and a second one has started in April 2018 and will run continuously until October 2018. The aim of these tests is to have a first proof of concept of the final apparatus as well as to study the effect of the multiple scattering on the angular distributions, from which we intend to extract our measurement. This chapter presents the data analysis of these test beams.

4.1 BEAM ENERGY KNOWLEDGE

One of the most crucial aspects of the MUonE experiment is to control systematics at the same level of statistical uncertainty. The statistical precision expected is 0.3% and a similar systematic uncertainty is necessary for the final measurement. One of the possible sources of systematic in the determination of $\frac{d\sigma}{d\theta_e}$ is the measurement of the beam momentum. We expect to use the M2 beam at CERN, which has the following properties:

- Energy spread: 3%;
- Spectrometer precision on single muon energy: 0.8%

The spectrometer resolution is acceptable to maintain under control systematics related to energy determination. The final measurement is going to be extracted from a fit over several values of $\Delta\alpha_{had}(t)$ at different t and the knowledge of the single muon energy at 0.8% level would allow an estimate of differential cross section at 10 ppm. However one has to deal with the energy loss effect in the apparatus. For the configuration described in this section we expect

$$E_{loss}(20 \times 1 \text{ cm Be})/E_0 \simeq 10^{-3}$$

Assuming this energy variation to be the largest in our set-up, we can try to understand how it will affect the precision on the value of cross-section. Once understood this point it will be useful to evaluate the effect of the energy error on the differential cross-section $\frac{d\sigma}{d\theta_e}$. These two studies allow us to understand whether the beam available from M2 satisfies our requirements or not. The leading-order $\mu e \to \mu e$ cross section with full mass dependence can be expressed as:

$$\frac{d\sigma}{d\theta_e} = \frac{d\sigma}{dt} \times \frac{8m_e^2 r^2 \mid \cos\theta_e \sin\theta_e \mid}{(1 - r^2\cos^2\theta_e)^2} \tag{8}$$

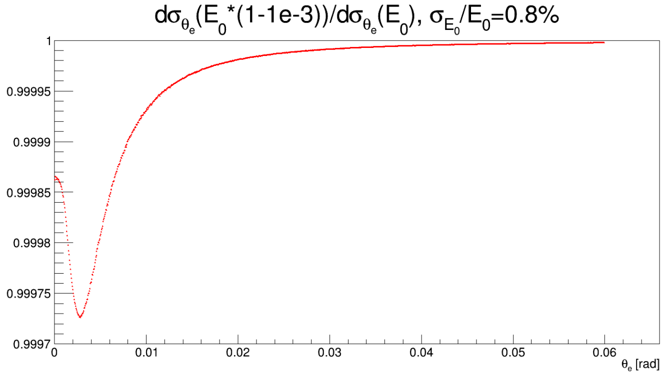

Figure 18: Relative effect of an energy miscalibration of 10^{-3} on the differential cross section $d\sigma/d\theta_e$.

Where:

$$\frac{d\sigma}{dt} = \frac{\mathcal{C}}{4\sqrt{(p_1 p_2)^2 - m_e^2 m_\mu^2}} \frac{1}{\sqrt{\lambda}} \times \mid M(s,t) \mid^2$$

Fig. 18 shows the relative effect of a 10^{-3} mis-calibration in the beam energy on the leading-order differential cross section assuming a beam with energy resolution $\sigma_E/E = 0.8\%$ as the one provided by M2 (see Fig. 19). Hence a possible mis-calibration at a 10^{-3} level due to energy loss induces a maximum relative variation effect on the differential cross-section with respect to the case of the nominal energy of $\sim 2.5 \times 10^{-4}$. It is interesting to note that this effect is maximum in the signal region, while effects are smaller in the normalization region. Having at disposal the nominal resolutions on mean energy and single muon energy determination from M2 one can try to exploit these informations to reconstruct the kinematics of the two body event. This would be extremely useful to exploit the very precise angular resolution of the apparatus to determine the muon energy *a posteriori*. The energy reconstructed in such a way can be used to keep under control systematic uncertainties and to estimate the differential cross section at a 10 ppm level.

For the $\mu - e$ process the relation between the final momenta and the scattering angles is given by:

$$p'_\mu \sin\theta_\mu = p'_e \sin\theta_e \tag{9}$$

An interesting case is the equal angles scattering for which holds

$$\sqrt{(E'_\mu)^2 - m_\mu^2} = \sqrt{(E'_e)^2 - m_e^2}$$

Using the energy conservation and solving for E'_e one gets

$$E'_\mu = E_\mu + m_e - E_e \tag{10}$$

$$E'_e = \frac{(E_\mu + m_e)^2 - m_\mu^2 + m_e^2}{2(E_\mu + m_e)}$$

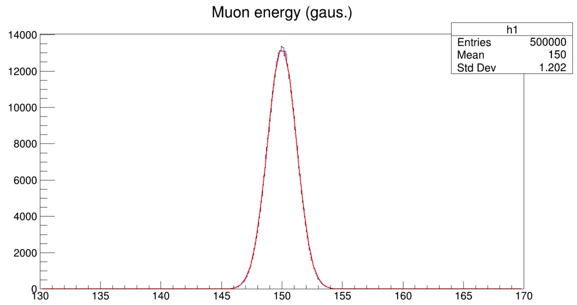

Figure 19: Incoming muons energy distribution of 5×10^4 events. Nominal resolution of 0.8%.

From which can be derived the muon final energy

$$E'_\mu = \frac{(E_\mu + m_e)^2 + m_\mu^2 - m_e^2}{2(E_\mu + m_e)}$$

Since the electron energy and the electron angle are correlated by

$$E'_e = m_e \frac{1 + r^2 \cos^2\theta_e}{1 - r^2 \cos^2\theta_e}, \; r^2 \equiv \frac{E_\mu^2 - m_\mu^2}{(E_\mu + m_e)^2}$$

Requiring the identity of the two expressions for E'_e we get

$$\cos^2\theta_e = \frac{x-1}{x+1} \times \frac{1}{r^2}, \tag{11}$$

$$x \equiv \frac{(E_\mu + m_e) - m_\mu^2 + m_e^2}{2m_e(E_\mu + m_e)} \tag{12}$$

Hence one can calculate the scattering angle and energies starting from the initial muon energy E_μ.
With a simple Monte Carlo we can simulate a run to study the problem of energy determination starting with a nominal muon energy. We assume $\sigma_{E_\mu}/E_\mu = 0.8\%$ and we simulate 5×10^5 events and for each one we reconstruct the scattering angles and final energies using the kinematic constraints (11), (12). Fig. 19 shows the initial energy distribution of the muons assuming a 0.8% resolution. In the equal angles condition, from eq. (11) we obtain for the scattering angles θ_μ, θ_e distributions shown in Fig. 20. The kinematics of the $\mu - e$ scattering gives $\theta_{e,\mu} \simeq 2.5$ mrad, which correspond to an energy of $E_{e,\mu}^{fin} \simeq 75$ GeV. Results are shown in Fig. 21. The region selected by the equal angle condition corresponds to the angular region where the differential cross-section is most sensible to possible effects of energy mis-calibration. However we know that the differential cross section is sensible to a level of 2.5×10^{-4} to a 10^{-3} energy discrepancy from the nominal value, as shown in Fig. 18. Eventually we can reconstruct the initial muon beam energy using these quantities and the kinematic

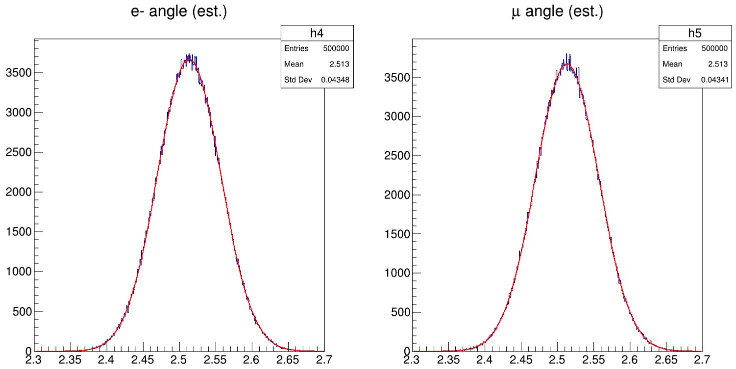

Figure 20: The angular distributions of scattered electrons and muons in the equal angle condition. Distributions obtained from eq. 11 taking into account the smearing for multiple scattering and detector angular resolution.

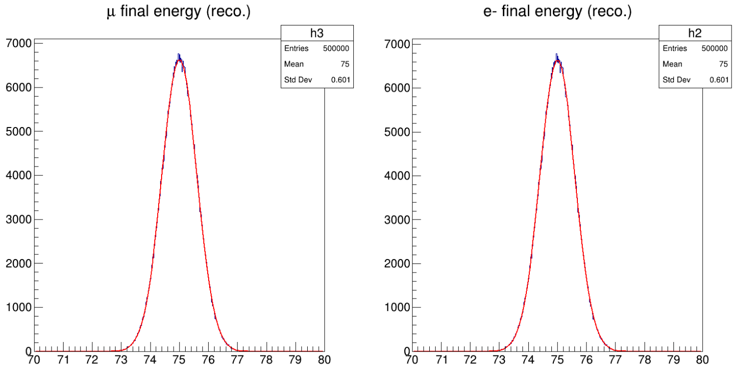

Figure 21: Final reconstructed energies for outgoing μ and e^- in the equal scattering assumption. Fit of the distributions in the gaussian hypothesis returns $E_\mu = (75.0014 \pm 0.0008)$ GeV.

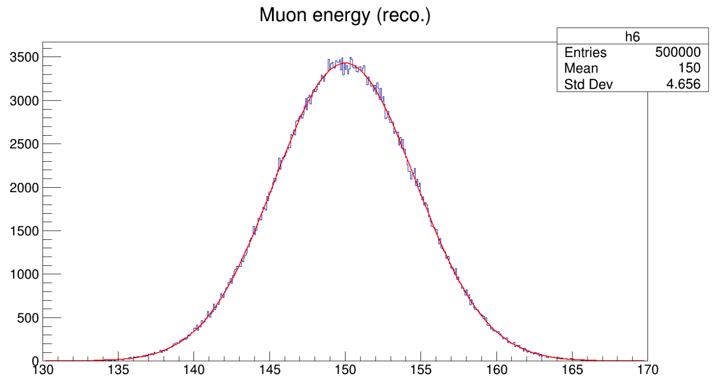

Figure 22: Reconstructed muons incoming distributions for 5×10^5 events. Fit in the gaussian hypothesis returns a value of $E_\mu = 150.003 \pm 0.006$ GeV.

relations derived at the beginning of this section. Fig. 22 shows the result of the reconstruction, assuming the energy mean value is known with 3% resolution. Hence, assuming the angular distribution to be gaussian with $\sigma_\theta = 0.03$ mrad, a sample of the order of 10^5 scattering events allows to control the precision on the mean value to a 10^{-5} level also in the signal region, where a possible energy mis-calibration can introduce non negligible systematics on $\frac{d\sigma}{d\theta}$. In order to corroborate this result we explicitly determine the effect of E_μ and θ_e on the final error on $d\sigma_{\theta_e}$. To do so we write the leading-order differential cross section explicitly in terms of the muon beam energy and we compute the partial derivative within respect this variable. In the assumption that θ_e and E_μ can be considered as statistically independent we have that

$$(\sigma_{d(CS)})^2 \propto \left(\frac{\partial dCS}{\partial E_\mu}\right)^2 \sigma^2_{E_\mu}$$

In the following we calculate also the effect of θ_e on the final error on $d\sigma_{\theta_e}$ and we compute the covariance as well as the correlation parameter for these two variables

$$Cov(\partial_{E_\mu} dCS, \partial_{\theta_e} dCS) = 3.1 \times 10^{-4}$$

$$\rho_{(\partial_{E_\mu} dCS, \partial_{\theta_e} dCS)} = 0.36$$

We will discuss in more details these results, but on this basis we can use the assumption for which the two contributions can be considered as statistically independent and their effect on the final error on the cross-section can be treated separately. Hence, we rewrite $\frac{d\sigma}{d\theta_e}$ explicitly in terms of E_μ. In the lab reference frame, the relations between useful kinematic variables are:

$$s = M_e^2 + m_\mu^2 + 2m_e E_\mu, \ t = 2m_e^2 - 2m_e E_e \tag{13}$$

Where E_e depends on E_μ as:

$$E_e = m_e \frac{1 + r^2 \cos^2\theta_e}{1 - r^2\cos^2\theta_e}, \; r = \frac{\sqrt{E_\mu^2 - m_\mu^2}}{E_\mu + m_e} \tag{14}$$

We also express $p_1 p_2$ in terms of E_μ using the above definition of s:

$$p_1 p_2 = \frac{s - m_e^2 - m_\mu^2}{2} = m_e E_\mu$$

For what concerns $\mid M(s,t) \mid^2$ we have:

$$\mid M(s,t) \mid^2 = \frac{4\pi\alpha^2}{t^2}(t^2 + 2st + 2s^2 + 2m_\mu^4 - 4m_\mu^2 s + 2m_e^4 - 4m_e^2 s + 4m_e^2 m_\mu^2)$$

Using (13) we have:

$$\begin{aligned} \mid M(s,t) \mid^2 = \frac{4\pi\alpha^2}{t^2}(8m_e^4 - 12m_e^3 + 4m_e^2E_e^2 - 4m_\mu^2 m_e E_e + 8m_e^3 E_\mu + \\ + 8m_e^2 E_\mu^2 + 4m_e^2 m_\mu^2 - 8m_e^2 E_e E_\mu) \end{aligned}$$

Hence, we rewrite $\frac{d\sigma}{d\theta_e}$ explicitly in terms of E_μ. Eventually, $\frac{d\sigma}{d\theta_e}$ can be expressed as:

$$\frac{d\sigma}{d\theta_e} = \frac{\mathcal{C} 2 m_e}{\sqrt{\lambda(E_\mu)}} \mid M(E_\mu, \theta_e) \mid^2 \frac{\sqrt{E_\mu^2 - m_\mu^2} \mid \cos\theta_e \sin\theta_e \mid}{(E_\mu + m_e)^2 \left(1 - \frac{E_\mu^2 - m_\mu^2}{(E_\mu + m_e)^2}\cos^2\theta_e\right)^2}$$

At this point it is possible to calculate the partial derivative of the differential cross section within respect to E_μ and to evaluate the contribution of a possible mis-calibration on the final error on $d\sigma_{\theta_e}$. Eventually we have:

$$\begin{aligned} \frac{1}{\mathcal{K}} \frac{\partial(dCS)}{\partial E_\mu} &= \frac{\mid M(E_\mu, \theta_e) \mid^2 \left|\sin(\theta_e)\cos(\theta_e)\right|}{\sqrt{\lambda(s, m_e^2, m_\mu^2)}} \times \\ &\times \left[\frac{2m_\mu^2 m_e - m_\mu^2 E_\mu \cos^2\theta_e + 2m_\mu^2 E_\mu + m_e^2 E_\mu + E_\mu^3 \cos^2\theta_e - E_\mu^3}{\sqrt{E_\mu^2 - m_\mu^2}\left(m_\mu^2 \cos^2\theta_e + m_e^2 + 2m_e E_\mu - E_\mu^2\cos^2\theta_e + E_\mu^2\right)^2} \right] + \\ &+ \frac{1}{\sqrt{\lambda(s, m_e^2, m_\mu^2)}} \frac{\partial \mid M(E_\mu, \theta_e) \mid^2}{\partial E_\mu} \frac{\sqrt{E_\mu^2 - m_\mu^2} \left|\sin(\theta_e)\cos(\theta_e)\right|}{\left(1 - \frac{E_\mu^2 - m_\mu^2}{\left(E_\mu + m_e\right)^2}\cos^2\theta_e\right)^2 \left(E_\mu + m_e\right)^2} + \\ &- \frac{4m_e^2 E_\mu}{\lambda(s, m_e^2, m_\mu^2)^{3/2}} \mid M(E_\mu, \theta_e) \mid^2 F(E_\mu, \theta_e) \end{aligned}$$

Using the same Monte Carlo implemented above, we have generated a new sample of 5×10^5 events and we used the muon energy reconstructed (Fig. 22) using the kinematical constraint of the equal angles

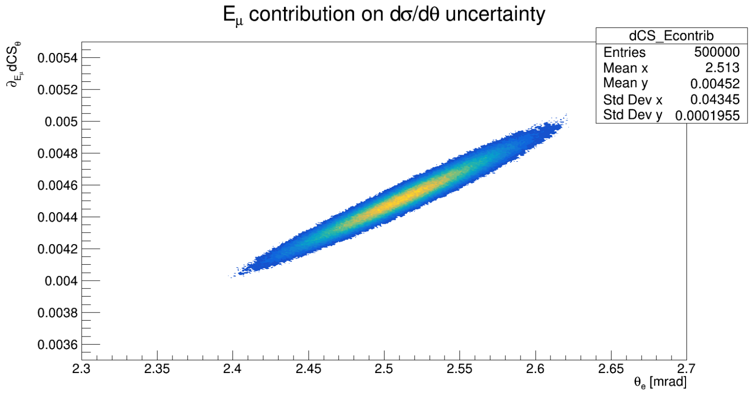

Figure 23: Effect of the muon energy error on the differential cross-section versus the final electron angle. Assuming an initial resolution of $\sigma_{E_\mu}/E_\mu = 1\%$ and a final energy spread of 3%.

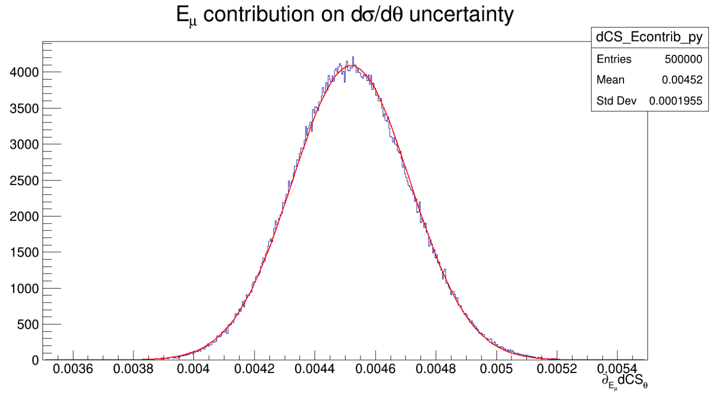

Figure 24: y-projection of the plot 23. Distribution of $\partial_{E_\mu} d\sigma_{\theta_e}$ for 5×10^5 events. Gaussian fit returns $\partial_{E_\mu} d\sigma_{\theta_e}(E_\mu) = 0.00452$

scattering to evaluate $\partial_{E_\mu} d\sigma_{\theta_e}(E_\mu)$. Assuming an initial beam of 150 GeV with the nominal resolution from M2 beamline of $\sigma_{E_\mu}/E_\mu = 0.8\%$ we find that the mean value of $\partial_{E_\mu} d\sigma_{\theta_e}(E_\mu)$ correspond to

$$\partial_{E_\mu} d\sigma_{\theta_e}(E_\mu) = 0.00452$$

Fig. 24 shows the result of the Monte Carlo run with 5×10^5 events to evaluate the effect of the energy beam uncertainty on the overall differential cross section error. Hence, the statistical contribution to the cross-section error due to the muon energy error is $\sigma_{stat} = \partial_{E_\mu} d\sigma_{\theta_e}(E_\mu) \times \sigma_{E_\mu} \sim \mathcal{O}(10^{-4})$. The systematic contribution is maximum in the signal region and it is of the order of 10^{-4} as well. It is important to observe that a possible mis-calibration of the energy does not affect the $\partial_{E_\mu} d\sigma_{\theta_e}(E_\mu)$ value found with this analysis, even if we are in the region where the cross-section is most sensitive to possible systematics. Fig. 25 shows the relative ratio of the $\partial_{E_\mu} d\sigma_{\theta_e}(E_\mu)$ value in case of an energy mis-calibration of a 10^{-3} level. This result suggests that the uncertainty on the final value of the differential cross-

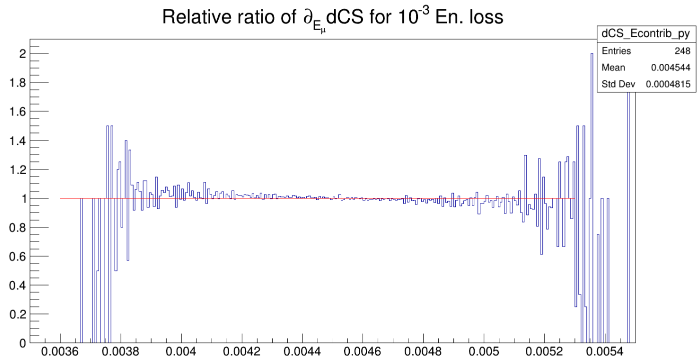

Figure 25: $\partial_{E_\mu} d\sigma_{\theta_e}(E_\mu)$ ratio when evaluated at the correct E_μ value and when a 10^{-3} mis-calibration is introduced.

section due to σ_{E_μ} can be kept under control even if a systematics is introduced in the energy determination. The systematic and statistical contributions to the cross-section error due to the beam energy error are independent, without correlation. For completeness we determine the contribution of θ_e to the cross section error, following the same strategy used for the E_μ contribution. First of all, we express $\frac{d\sigma}{d\theta_e}$ in terms of θ_e and we note that:

$$\frac{d\sigma}{d\theta_e} = \underbrace{\frac{\mathcal{C}}{flux\sqrt{\lambda}}}_{\theta_e\text{-independent}} \underbrace{\mid M(s,\theta_e) \mid^2 \frac{8m_e^2 r^2 \mid \cos\theta_e \sin\theta_e \mid}{(1-r^2\cos^2\theta_e)^2}}_{t=t(\theta_e)}$$

We express t in terms of θ_e using (14):

$$t = 2m_e^2 - 2m_e E_e = 4m_e^2 \frac{r^2\cos^2\theta_e}{r^2\cos^2\theta_e - 1}$$

From which follows that:

$$\mid M(s,t) \mid^2 = \mid M(s,\theta_e) \mid^2 = \frac{4\pi\alpha^2}{t^2}\left(t^2 + 2st + c\right) =$$
$$= 4\pi\alpha^2 + \frac{2\pi\alpha^2 s}{m_e^2} - \frac{2\pi\alpha^2 s}{m_e^2 r^2 \cos^2\theta_e} + \frac{\pi\alpha^2 c(r^2\cos^2\theta_e - 1)^2}{4m_e^4 r^4 \cos^4\theta_e}$$

Where $c = 2s^2 + 2m_\mu^4 - 4m_\mu^2 s + 2m_e^4 - 4m_e^2 s + 4m_e^2 m_\mu^2$.

Proceeding as above, we need to evaluate $\frac{\partial |M|^2}{\partial\theta_e}$:

$$\frac{\partial \mid M \mid^2}{\partial\theta_e} = \frac{\pi\alpha^2 \sin\theta_e}{m_e^2 r^2}\left[\frac{16c}{10\cos\theta_e + 5\cos(3\theta_e) + \cos 5\theta_e} + \right.$$
$$\left. + \frac{4c}{3\cos\theta_e + \cos 3\theta_e} + \frac{16s}{3\cos\theta_e + \cos 3\theta_e}\right]$$

For completeness, we evaluate the partial derivative within respect to θ_e of the second factor in $\frac{d\sigma}{d\theta_e}$:

$$\mathcal{F}(\theta_e) = \frac{8m_e^2 r^2 \mid \cos\theta_e \sin\theta_e \mid}{(1-r^2\cos^2\theta_e)^2}$$

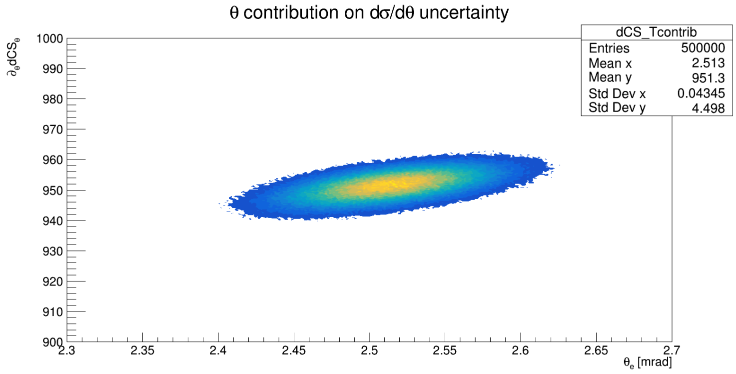

Figure 26: Effect of the scattering angle error $\delta\theta_e$ on the differential cross-section versus the final electron angle. Initial distributions smeared for detector and multiple scattering effects. Run of 5×10^5 events.

$$\frac{\partial \mathcal{F}(\theta_e)}{\partial \theta_e} = \frac{32 m_e^2 r^4 \cos\theta_e \sin\theta_e \mid \cos\theta_e \sin\theta_e \mid}{(r^2\cos^2\theta_e - 1)^2} + \\ + \frac{4 m_e^2 r^2 \sin(4\theta_e)}{(1 - r^2\cos^2\theta_e)^2 \mid \cos\theta_e \sin\theta_e \mid}$$

Eventually we have:

$$\frac{1}{\mathcal{K}}\frac{\partial(dCS)}{\partial\theta_e} = \frac{\partial \mid M(s,\theta_e) \mid^2}{\partial\theta_e}\frac{8 m_e^2 r^2 \mid \cos\theta_e \sin\theta_e \mid}{(1 - r^2\cos^2\theta_e)^2} + \\ \mid M(s,\theta_e) \mid^2 \frac{\partial \mathcal{F}(\theta_e)}{\partial\theta_e}$$

Using the same Monte Carlo and the same procedure adopted for the E_μ calculation, we can derive the value of $\partial_{\theta_e} d\sigma_{\theta_e}$ in the region of equal angles scattering. Fig. 27 shows the result of this calculation and returns a value of

$$\partial_{\theta_e} d\sigma_{\theta_e} = 951.2 \text{ b/mrad}$$

This contribution is found to be stable also when an energy miscalibration of 10^{-3} is introduced, suggesting that the energy and angle error contributions to the final cross-section error are statistically independent. Even if the two contributions depend both on E_μ and on θ_e they are uncorrelated one with the other. Fig. 28 shows the scatter plot of the two different contributions on the cross-section error: the distribution is almost flat and this is a first hint of non correlation between the two variables. Moreover we can extract the covariance using the `TH2::GetCovariance()` method in `ROOT` and we get

$$Cov(\partial_{E_\mu} dCS, \partial_{\theta_e} dCS) = 3.1 \times 10^{-4}$$

Then we can use this quantity to compute the correlation parameter ρ, which is defined for two generic variables (x, y) as

$$\rho_{(x,y)} = \frac{Cov(x,y)}{\sqrt{Var(x)Var(y)}}, \; -1 \leq \rho \leq 1$$

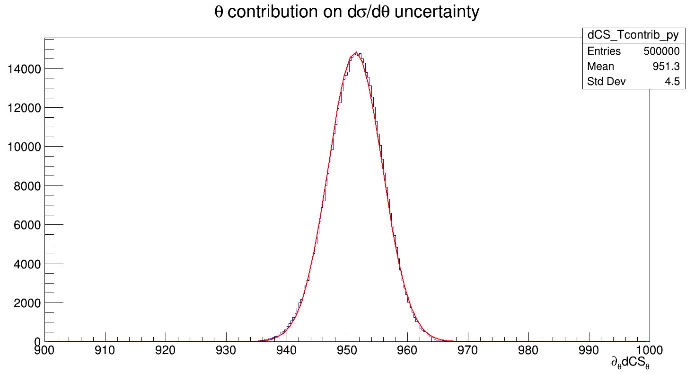

Figure 27: y-projection of the plot 26. Distribution of $\partial_{\theta_e} d\sigma_{\theta_e}$ for 5×10^5. Gaussian fit returns $\partial_{\theta_e} d\sigma_{\theta_e}(E_\mu) = 951.22$ b/mrad

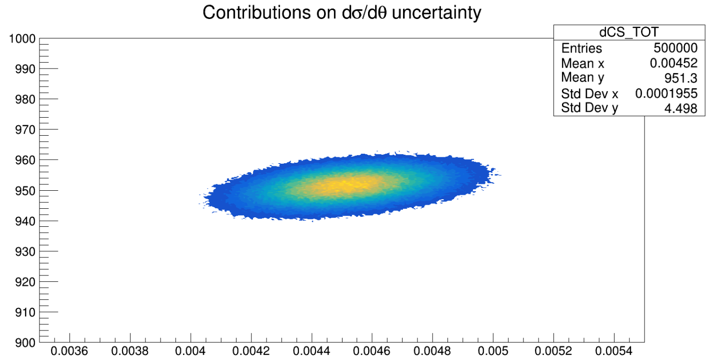

Figure 28: Scatter plot of $(\partial_{E_\mu} dCS, \partial_{\theta_e} dCS)$.

In our case we obtain

$$\rho_{(\partial_{E_\mu} dCS, \partial_{\theta_e} dCS)} = 0.356$$

A good index of non correlation between the two sources of statistical error on the differential cross-section uncertainty.

This study is based on a completely analytical approach and it confirms previous results: in order to control the final error on the differential cross section we can rely on statistics and on current features of the apparatus. Reconstructing the muon energy for 5×10^5 events with a precision on $\langle E_\mu \rangle$ of 3%, its effect on the differential cross section is of the order of 4.5×10^{-3} b/GeV, while the effect of $\delta\theta_e$ is equal to 9.52×10^2 b/mrad. Both these effects are not affected by the systematics introduced by a possible energy mis-calibration, even when evaluated in the region where the differential cross-section is most sensitive to the energy loss in the apparatus, as previously shown in Fig.18.

4.2 TEST BEAM 2017

For the final experiment it will be crucial to have a complete and sound understanding of the effect of multiple scattering and to have at disposal a full simulation of the experimental apparatus. The work of my thesis is focused on these two aspects. The data analysis is performed on data from a dedicated test beam we had in October 2017, using the H8 line at CERN. The experimental set-up employed for this test beam is commonly used by the UA9 collaboration [32] to calibrate scintillating crystals with high-energy π beams.
The aim of the test beam was to collect data in order to study the effect of multiple scattering in low-Z targets with direct comparison to Monte Carlo simulations and to have a first appraisal of a single module of the final detector. Since we expect each module to work standalone in the final apparatus, this test beam also provides a good proof-of-concept of our apparatus. The set-up used consists of two upstream planes of Si trackers distant ∼10 m one from the other, a target and three downstream tracking planes covering ∼ 1 m. Each silicon tracker is composed by two layers 320 μm thick, with a $3.8 \times 3.8\,\text{cm}^2$ active area, to measure both the x and y coordinates. Fig. 29 represents the test beam set-up with the distances, in mm, taken by the UA9 collaboration. We had at disposal a total of five targets (C, Al) of different thicknesses and all of them were tested. The week of data taking was very efficient and we could exploit all the possible configurations available at H8 line. Tables 3, 4 give a summary of the acquired data. We refer as *alignment runs* to those acquisitions without target, for each beam configuration. Eventually these data turned out to be fundamental for the preliminary alignment procedure we had

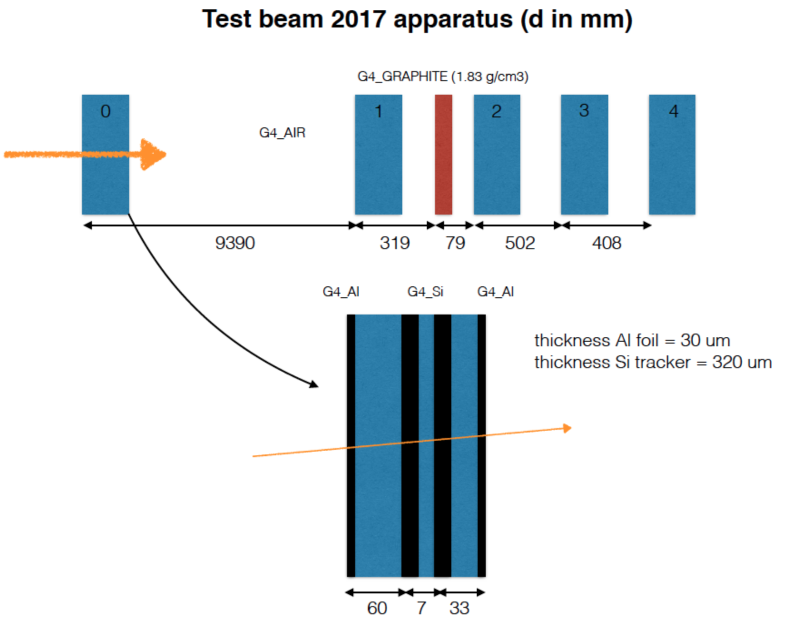

Figure 29: Test beam 2017 detector set-up. Distances in mm measured by UA9 collaboration.

to develop to eliminate shifts in angular distributions, coming from set-up misalignments.

Data analysis is presented in details in the next sections. This test beam was extremely fruitful, as the large quantity and variety of acquired data allowed us to study in details the effect of multiple scattering: using both a detailed simulation of the apparatus and a more analytical approach based on a fit of the angular deflection distributions. Moreover we could exploit the run at 160 GeV μ^+ to perform also a first reconstruction of $\mu - e$ elastic events, defining possible cuts to be used for the final experiment and using the simulation to study background effects to control the signal/background ratio.

4.2.1 *Fiducial cuts*

Each silicon tracker registered hits as clusters: starting from hit clusters per plane we had an iterative alignment procedure based on residuals with the final aim of eliminating set-up misalignments present in data. We used data without target, i.e. *alignment runs* (see Tab. 4), to extract the constants for the alignment and then, with a fit on hits for the up/down-stream planes separately, we aligned data with targets. The analysis was performed on data collected into `TTree` which recorded informations of hits per plane, chi-squared values and residuals for the two coordinates from alignment and the reconstructed angles for the incoming and outgoing tracks.
However events close to the edge of the active area could be affected

Run	**Beam**	**Target Type**	**N events**$\times 10^6$
5328	12GeV e^-	2mm Al	7
5317,18	20GeV e^+	2mm Al	1.6
5333,34	12GeV e^-	2mm C	14
5311,12,13,14,15	20GeV e^+	2mm C	5
5341	12GeV e^-	4mm C	15
5344	20GeV e^-	4mm C	15
5348	12GeV e^-	8mm C	15
5352	20GeV e^-	8mm C	12
5355+5360	20GeV e^+	8mm C	3
5330,38	12GeV e^-	20mm C	15
5302,5,6,7,8,9+5358	20GeV e^+	20mm C	7(day1/2)+8(day6/7)
5367,68,70,71,72,73,74	160GeV μ^+	8mm C	10/run

Table 3: Data summary: Normal Runs

Run	**Beam**	**N events**$\times 10^6$
5286	180GeV π^+	all night day1
5298,5299	20GeV e^+	500+500 (day1, 2 runs) + 1 (day6)
5351	20GeV e^-	1 (day6)
5357	20GeV e^+	1 (day6)
(5337+)5349	12GeV e^-	1
5363,69	160GeV μ^+	2 total
5303,10,16,56,59	180GeV π^+	1/run

Table 4: Data summary: Alignment Runs (no target)

by worse resolution, different acceptance and other effects. Therefore some cuts have been studied to reject these particles and to keep only events inside specific fiducial cuts. These cuts are geometrical cuts on the first two planes active area, since from these two trackers we retrieve the direction of the incoming particle before the scattering inside the target. A fiducial cut on the first two planes affects overall statistics and acceptance on the downstream planes but it is necessary to ensure good quality events for the data analysis. Fig. 30-33 show the profile plots for the hits distribution on the upstream planes for 20 GeV electrons beam. As one can see profiles tend to get far from uniformity approaching Si trackers edges. To ensure uniformity in

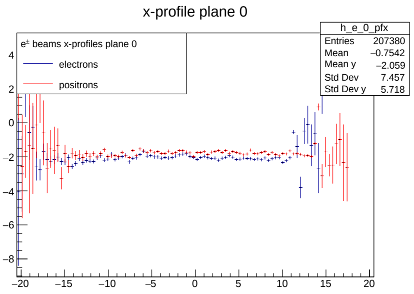

Figure 30: x profile, first plane.

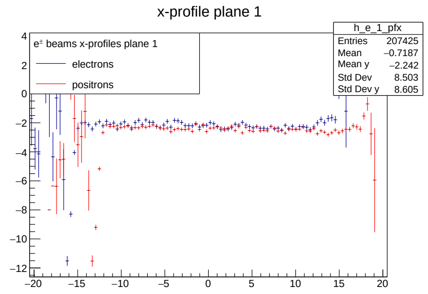

Figure 31: x profile, second plane.

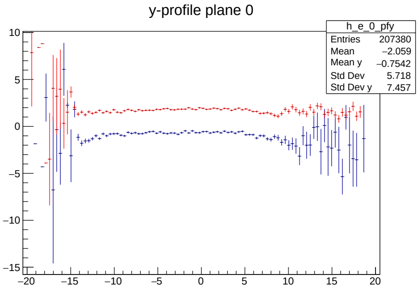

Figure 32: y profile, first plane.

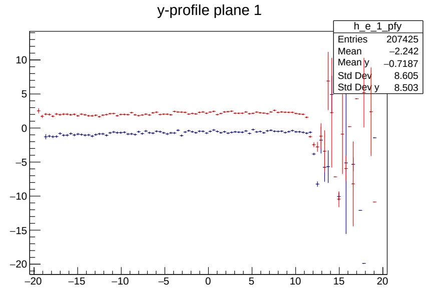

Figure 33: y profile, second plane.

acceptance and resolution over the entire dataset, it has been necessary to introduce fiducial cuts on these distributions. More precisely, this cut was decided with a comparison of its effect on the Monte Carlo simulation of the apparatus: the final aim is to find a compromise between statistics reduction and uniformity in acceptance and distribution. Eventually we decided to take as *selection region* the active area $(-10; 10)$ mm on both the upstream planes. Fig. 35 show the effect of the fiducial cut on the angular distributions of a run with 12 GeV electrons without target. The asymmetry observed in the distribution before the application of the cut is entirely an effect of the detector, presumably due to effects at the edge of Si trackers. The selection of a region where the incoming beam profile is uniform (see Fig. 30-33)

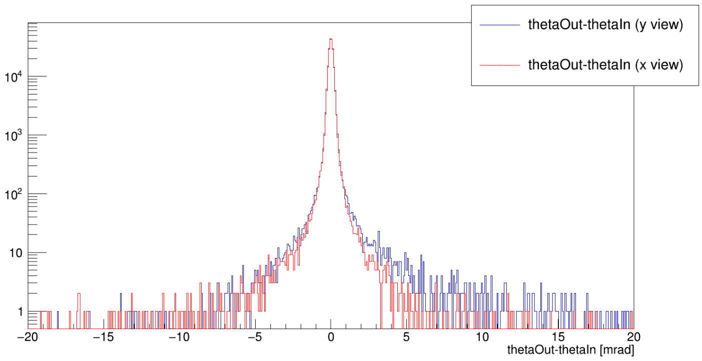

Figure 34: Angular deflections in both views without fiducial cut. Presence of asymmetry in the x-view distribution.

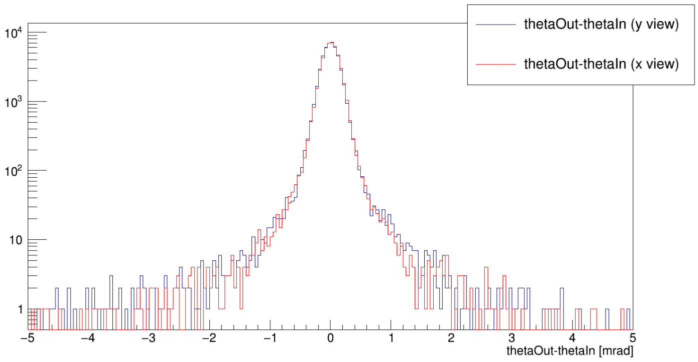

Figure 35: Angular deflections in both views after the application of the fiducial cut. Asymmetry vanishes and distributions are more regular.

removes the presence of these asymmetries in angular distributions and regularizes data for the analysis.

The result presented here for the 12 GeV case holds for the 20 GeV data as well. This fiducial cut has to be applied both to experimental and simulated data. For the final precision required by our experiment, this cut is going to be fundamental to reduce possible systematics coming from detector inefficiencies. Working in regions where the beam properties are well known and where the detector can be exploited at its nominal efficiency is a crucial point for our measurement. To maximize these two effects we also introduced an angular fiducial cut. This further selection criterion is justified by Fig. 36, which shows the profile histogram of the angular deflection (thetaOut-thetaIn) against the incoming angle thetaIn, for 12 GeV electrons . We decided to select only those events with incoming angular distribution in the range $(-2, 2)$ mrad to avoid possible board effects. The net effect of this cut is almost negligible on the overall statistics and on the analysis results. While the previous geometrical cut is certainly needed in the final experiment, this second selection criterion could be unnecessary according to the detector specifics and

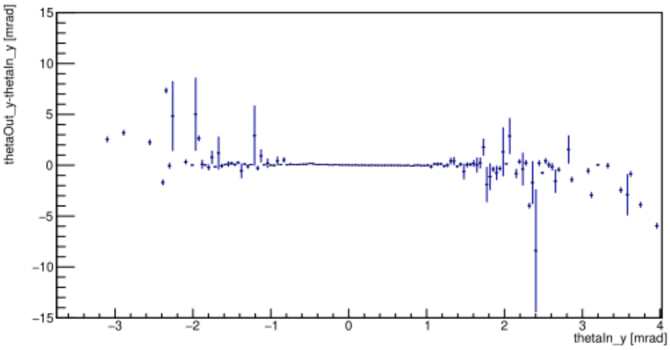

Figure 36: Run of 12 GeV electrons without target. Profile histogram of the angular deflection against the incoming angular distribution, y-view.

the precision of alignment. Hence, a study *a priori* of the beam profile is required to understand whether these cuts have to be applied or not and to decide the selection intervals.

4.2.2 *Monte Carlo simulation*

One of the fundamental tools needed in the analysis is the Monte Carlo simulation of the full apparatus. A dedicated simulation of the test beam set-up was developed using the `GEANT4` software [33]. Several efforts have been made during the work of this thesis to understand the best physics model to achieve the most accurate description of the experimental set-up. In particular a proper choice of the `PhysicsList` has been fundamental: we decided to work with the standard electromagnetic `option 4` from `Geant4.10.4`, as it includes a selection of most accurate physics models from Standard and Low Energy sets of models implemented in `GEANT4`. The final simulation was built on top of the `GEANT4` example `TestEm5`, with modifications of some user defined classes: `DetectorConstruction`, `SteppingAction` and `PrimaryGeneratorAction`. For what concerns the geometry, we constructed a silicon telescope consisting of two upstream Si trackers and three downstream ones, with a graphite target in between. Each silicon tracker implemented has the nominal thickness of 320 μm and it is followed by an Al foil 30 μm thick as shown in Fig. 29. For these components we used the standard materials from `G4Element` class. The Si trackers resolution on measured hits is 6.9 μm for the second and third planes (the first two downstream planes) and 40 μm for the last downstream plane. The last plane has a different resolution, since in the original configuration of the apparatus it is positioned at $\sim$ 10 m from the fourth plane and it is used with a different scope. The target studied in the simulation is the C target. More precisely it consists of a graphite and it was specifically built for the Test Beam. It is simulated using the `G4NistManager` to adapt it to the nominal

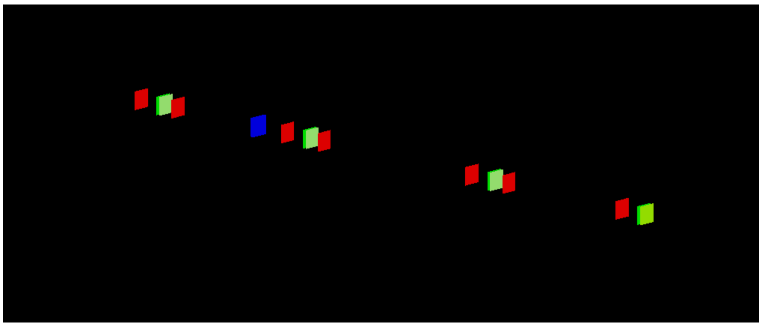

Figure 37: GEANT4 representation of the experimental apparatus used in Test Beam 2017. The first upstream plane is not shown. Green: Si trackers, Blue: Target, Red: Al foils.

density of the experimental target which is $1.83\,\mathrm{g/cm^3}$. The result of the representation of the geometry in GEANT4 is shown in Fig. 37, where the Si trackers are in green, the Al planes in red and the target in blue.

The simulation runs in multi-thread and provides n `.txt` output files, where n is the number of cores used. Each output file contains the same information stored in the experimental run, i.e. hits per plane, and some additional information needed for detailed studies, such as energy of the incoming beam, energy deposit in the target and type of interactions of the primary particle. The generation of initial beam profiles, according to the specifics of the H8 line beam optics, is implemented in the `PrimaryGeneratorAction` class. To do so, we extract the cumulative distribution functions (CDF) of each *alignment run* and we use them to generate particles randomly distributed according to the original probability distribution function (PDF) in the `GeneratePrimaries()` method of this class. In such a way we explicitly take into account the smearing due to the hits resolution and the spread of the incoming beam momentum. As an example, Fig. 38 shows the cumulative used to simulate the μ run. The initial beam energy is set in the simulation with a 2% resolution, as quoted by the H8 beam experts. Eventually `.txt` files are processed with a `ROOT` macro which creates a `TTree` with the same structure of the one used for data.

Fig. 39, 40 and 41 present the results of the comparison between data and simulation for runs of 12 GeV e^-. Plots are generated with a 0.02 mrad bin width. The overall agreement between data and Monte Carlo is qualitatively good for all the configurations simulated. The effect of the target is directly related to the correlation between the multiple scattering inside the target and the description of the apparatus in the simulation. It is clear that increasing target thickness leads to a better agreement between data and Monte Carlo: data without target are systematically lower than simulated ones in the core region ((-0.5, 0.5) mrad), while this behavior changes in tails

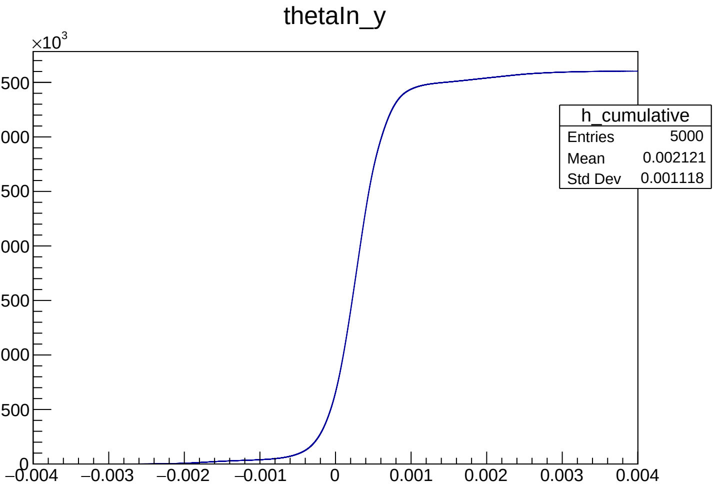

Figure 38: Cumulative distribution function extracted from data and used to simulate μ runs.

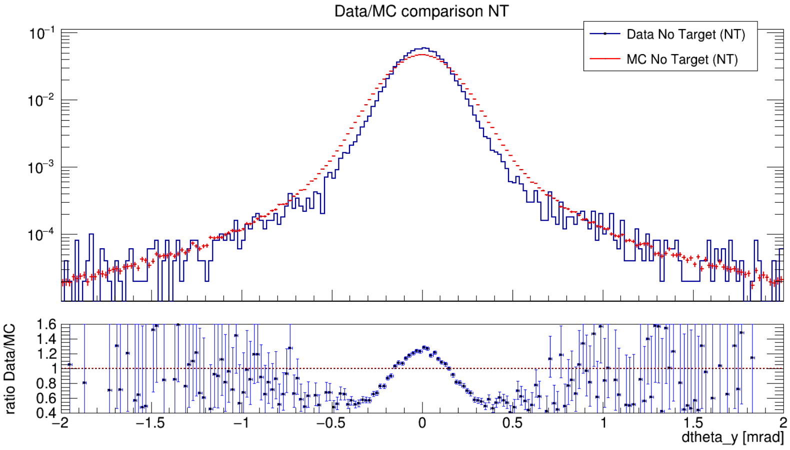

Figure 39: Data/MC comparison and ratio for run without target (only apparatus). Bin width 0.02 mrad.

(see Fig. 39). This effect is still present but becomes more and more negligible increasing target thickness to 8 mm or 20 mm. These differences can be studied quantitatively exploiting the ratio of the two histograms in order to quantify the discrepancy between simulation and experimental data. Lower part of Fig. 39, 40 and 41 shows the profile histograms for the ratio MC/Data. For all the cases the two distributions are in good agreement in the core region, i.e. in the interval $(-0.5, 0.5)$ mrad, while the agreement worsens in tails accounting to fluctuations up to $\sim$ 40%, especially because of the poor statistics in these bins. However it is worth to underline that core region contains $\sim$ 90% of the events and here we obtain a $\sim$ 1% agreement between data and Monte Carlo, with fluctuations of only few percents. More in detail, Fig. 42, 43, 44 show the ratio

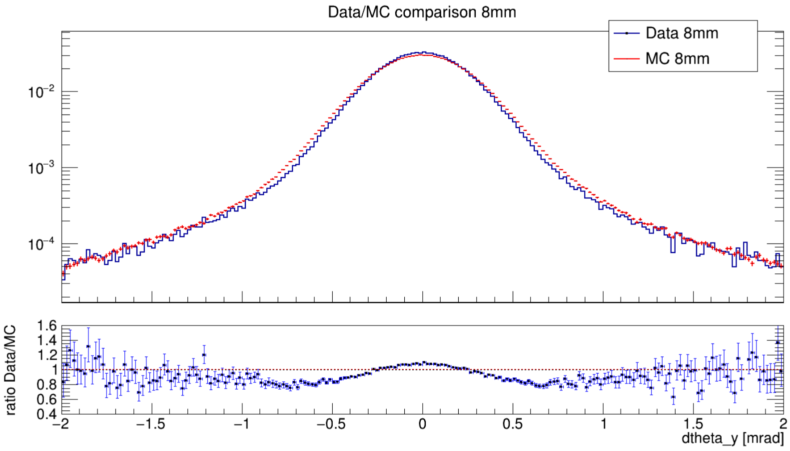

Figure 40: Data/MC comparison and ratio for run with 8mm thick C target. Bin width 0.02 mrad.

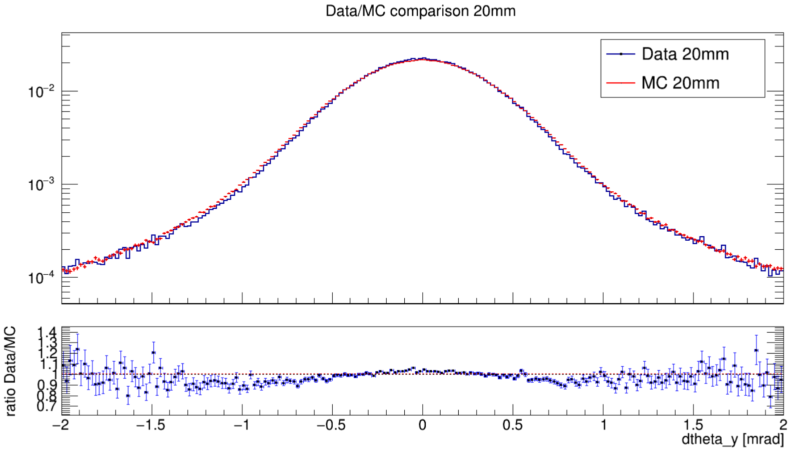

Figure 41: Data/MC comparison and ratio for run with 20mm thick C target. Bin width 0.02 mrad.

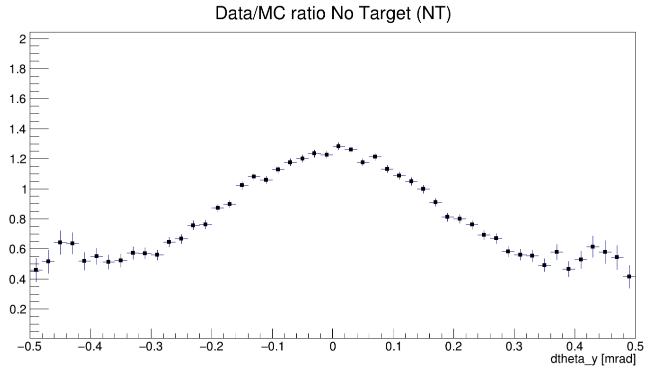

Figure 42: Data/MC ratio for run without target (only apparatus). Core region: -0.5, 0.5 mrad. Maximum fluctuations of ∼ 20% in the entire region.

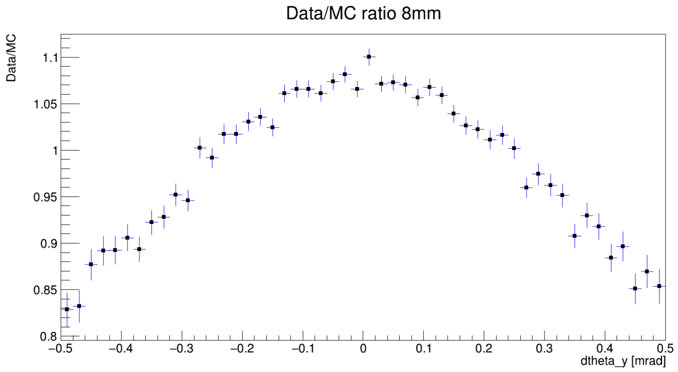

Figure 43: Data/MC ratio for run with 8mm thick C target. Core region: -0.5, 0.5 mrad. Maximum fluctuations of ∼ 8% around peak and ∼ 15% slightly outside peak.

Data/MC, with bin width of 0.02 mrad, in the core region and the effect outlined above is clearly evident. The worse comparison is obtained for the situation without target, where Data and MC are in agreement but with fluctuations contained to a 20% level. The effect of multiple scattering becomes predominant on an accurate description of the apparatus when targets are introduced, leading to a better agreement with data. Fig. 43 and 44 confirm good agreement between Data and MC: fluctuations are limited to a few percent in core region for these two cases. As we have observed the simulation becomes more accurate in describing data when the target is thicker, indicating an inaccurate description of the apparatus. Currently we are working on a more proficient representation of the Si trackers, since at the current state of art they are implemented as uniform silicon blocks and we expect this to be the main issue in the description of experimental data. This `GEANT4` simulation was designed specifically to study the 2017 Test Beam, but hopefully it is a good starting point for the design of the final apparatus simulation. Several efforts have been made to understand how to tune specific `GEANT4` parameters

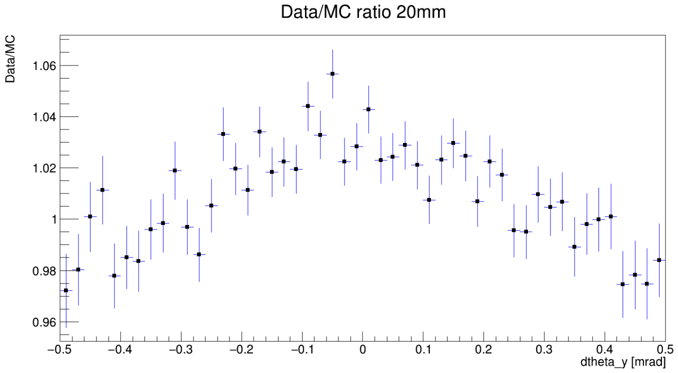

Figure 44: Data/MC ratio for run with 20mm thick C target. Core region: -0.5, 0.5 mrad. Maximum fluctuations of $\sim$ 4%.

to obtain results in agreement, in core region, at the level of $\sim$ 1% and we do expect to exploit this work for future test beams and for the final experiment. Even if the approach of a full simulation of the apparatus has to be preferred, as it should be free from the introduction of systematics in the analysis, it depends on many *ad hoc* parameters to be tuned. Some members of the collaboration worked on an alternative approach, based on the deconvolution of the apparatus effect from data, obtaining more stable and precise results on the entire angular range and not only in the core region. Current work is ongoing to develop full apparatus simulations both for the 2018 Test Beam and the final set-up with the intent to describe in detail silicon trackers, their electronic read-out and the signal formation phase to achieve a final agreement MC/Data of $\sim$ 1% also with the full-simulation approach. Notwithstanding these discrepancies present in the MC/Data comparison, this simulation was precise enough to describe large part of the data and it was used to study the effect of multiple scattering on angular deflection distributions, as presented in section 4.2.3. The analysis on multiple scattering effects returned results in good agreement with theoretical predictions and nominal (i.e. from the experiment set-up) values, validating the simulation developed.

4.2.3 *Multiple scattering*

A charged particle passing through matter is affected by random deviations from the nominal trajectory due to multiple scattering effects. These effects are described by the Möliere theory [34], which shows that traversing a thickness x, the particle undergoes successive small-angle deflections, symmetrically distributed around the incident direction

$$\theta_0 = \frac{13.6\text{ MeV}}{p\beta c} z_c \sqrt{\frac{x}{X_0}} \left[1 + 0.038 \ln\left(\frac{x}{X_0}\right) \right] \tag{15}$$

where p, β, c and z_c are the momentum, velocity and charge of the incoming particle and X_0 is the radiation length of the traversed material. The logarithmic term was introduced by Highland to take into account the length dependence of the deflections due to multiple scattering. More in general eq. (15) can be expressed as (see [35])

$$\theta_0 = \frac{S_2}{p\beta c}\sqrt{\frac{x}{X_0}}\left[1 + \epsilon \log\left(\frac{x}{X_0}\right)\right]$$

With S_2 and ϵ parameters to be determined according to the scattering medium properties. The improved Highland formula presented in [35] uses $S_2 = 13.6$ and $\epsilon = 0.088$ with good agreement for all Z.

On a large number of independent scattering events, according to the central limit theorem, the Moliere distribution of the scattering angle can be approximated by a Gaussian. It has been shown that this approximation is valid for the central 98% of the angular distribution on the plane. Under this assumption, the root mean square of the scattering angle eq. (15) represents the width of the gaussian. Namely, the plane projected angles θ_{xOz} and θ_{yOz} show an approximately Gaussian angular distribution of the form

$$\frac{1}{\sqrt{2\pi}\theta_0} \exp\left[-\frac{\theta^2_{Plane}}{2\theta_0^2}\right] d\theta_{Plane} \tag{16}$$

Moreover deflections on the x and y planes are statistically independent and identically distributed, and the deflection angle θ can be expressed as

$$\theta^2 = \theta^2_{xOz} + \theta^2_{yOz}$$

The experimental apparatus used in the 2017 test beam provided the trajectory measurements trough hits in the Si trackers. The precision of the track reconstructed depends on the number and position of the detector layer elements. Statistically the hits distribution has the same expression as eq. (16)

$$\frac{1}{\sqrt{2\pi}\sigma_{x_i}} \exp\left[-\frac{x_i^2}{2\sigma^2_{x_i}}\right] dx_i$$

Starting from all the hits on plane, after the alignment phase, we studied multiple scattering effects on different configuration of energy and target thickness. As expected these effects become more and more appreciable increasing the target thickness, while are reduced increasing the energy of the beam. Fig. 45, 46, 47 show an appreciable increase of angular deflection widths. The deflection angle given in eq. (15) can be quantified from the difference of angular distribution widths for a specific target and for the apparatus without target (*alignment runs* in Tab. 4).

$$\theta_0 = \sqrt{\sigma^2_{target} - \sigma^2_{NT}}$$

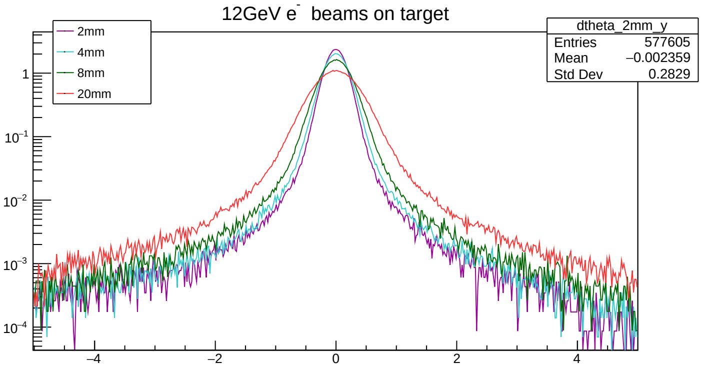

Figure 45: Effect of multiple scattering on 12 GeV e^- beam. Angular deflection distributions for different target thicknesses. Results for θ_{yOz}.

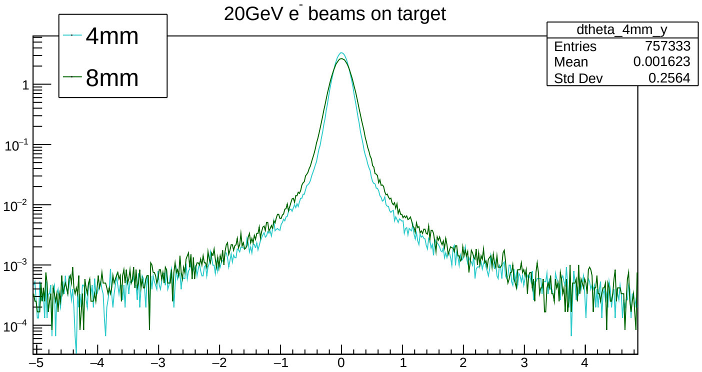

Figure 46: Effect of multiple scattering on 20 GeV e^- beam. Angular deflection distributions for different target thicknesses. Results for θ_{yOz}.

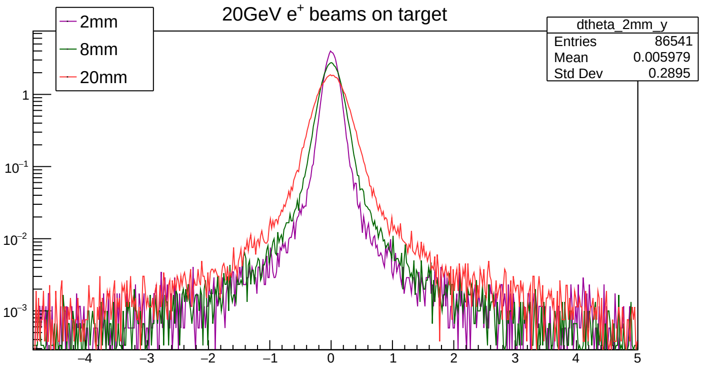

Figure 47: Effect of multiple scattering on 20 GeV e^+ beam. Angular deflection distributions for different target thicknesses. Results for θ_{yOz}.

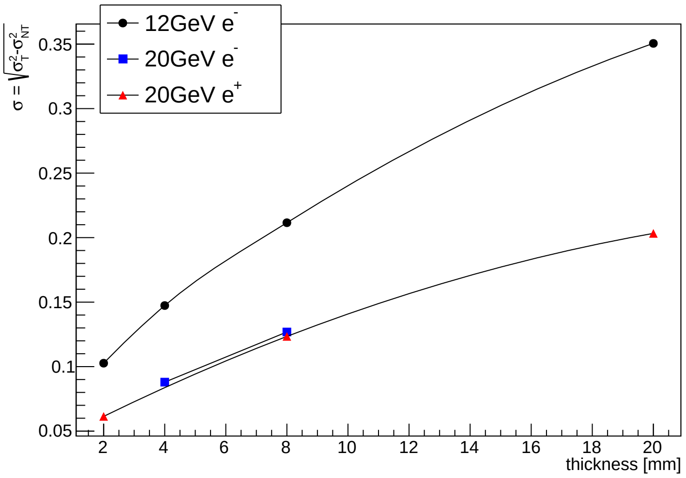

Figure 48: Multiple Scattering angle obtained from gaussian fit on the core (98%) of angular distributions. $\theta_{MS} = \sqrt{\sigma^2_{target} - \sigma^2_{NT}}$.

	$\theta_{MS}(20GeV, e^-)$ [mrad]	$\theta_{MS}(20GeV, e^+)$ [mrad]	$\theta_{MS}(12GeV, e^-)$ [mrad]
2 mm		0.0614 ± 0.0006 (0.0630)	0.103 ± 0.008 (0.1050)
4 mm	0.0879 ± 0.0004 (0.0891)		0.147 ± 0.006 (0.1485)
8 mm	0.1268 ± 0.0003 (0.1260)	0.124 ± 0.005 (0.1260)	0.212 ± 0.005 (0.2100)
20 mm		0.2033 ± 0.0006 (0.1992)	0.3205 ± 0.005 (0.3320)

Table 5: Multiple scattering deviations obtained from gaussian fit on angular distributions. Results for θ_{yOz} and theoretical values from eq. (15) in brackets.

Fig. 48 shows the result of this analysis: multiple scattering effects on two different particles with same momentum, traversing the same scattering medium is the same; the effect is more appreciable for lower energies and thick targets, as the case at 12 GeV $e-$ on 20 mm of graphite shows. Results are presented in Tab. 5 with the corresponding theoretical value from eq. (15). We have evaluated the agreement between the gaussian approximation and the theoretical expression from Moliere (15) both on data and MC. Retrieving θ_{MS} from a gaussian fit of the core for a beam of a given energy traversing several thicknesses, the fit of these points with eq. (15) returns results in agreement with expected values. Fig. 49 shows the fit on angular deflection distributions for data and Monte Carlo, obtained as described above, with the Moliere/Highland expression eq. (15). The fit values of energy and interaction length are:

$$E^{fit,MC} = 12.2 \pm 0.2 \text{ GeV}, \; X_0^{fit,MC} = 24.2 \pm 0.8 \text{ cm}$$

$$E^{fit,Data} = 12.2 \pm 0.2 \text{ GeV}, \; X_0^{fit,Data} = 23.4 \pm 0.7 \text{ cm}$$

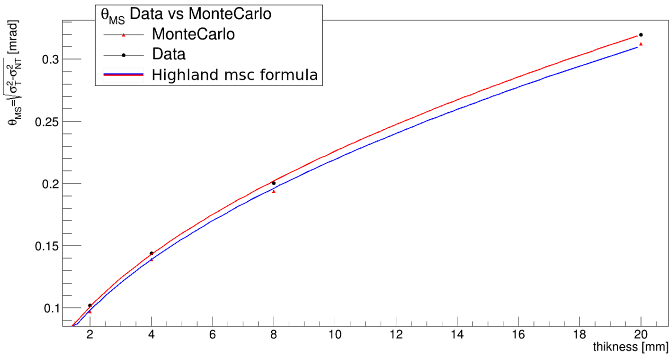

Figure 49: Data and MC for 12 GeV e^- on 2, 4, 8, 20 mm graphite targets. θ_{MS} obtained from gaussian fit of the core distribution. Fit with Highland/Moliere distribution (15).

The expected value for the energy is the nominal one at $E_0 = 12$ GeV while for the interaction length X_0 the one quoted by target producers and used in the simulation is

$$X_0^{exp} = 23.3 \text{ cm}$$

Fit parameters both for Monte Carlo and Data are in statistical agreement with the theoretical ones. Hence the gaussian approximation of the core distribution describes in a good way the $(\theta_{out} - \theta_{in})$ angular deflection. This observable can also be used to retrieve the effective resolution of the apparatus. Namely the experimental set-up resolution depends both on the hits resolution and the effect of multiple scattering in Si trackers. More precisely, these two effects are statistically independent and so the net effect is given by the sum of their squared values:

$$\Delta\theta = \sqrt{\theta^2_{\text{intr.}} + \theta^2_{MS}}$$

Where θ_{MS} is the one predicted by the Moliere theory of multiple scattering 15, while $\theta_{\text{intr.}}$ is the intrinsic angular resolution of the apparatus given by

$$\theta_{\text{intr.}} = \frac{\delta x_i \sqrt{2}}{D}$$

Where δx_i is the resolution on hits measurement and D is the distance between the interaction point and the Si tracker: in our case we had at disposal one single module of $D = 50$ cm and the intrinsic angular resolution of the TB2017 apparatus was:

$$\theta_{\text{intr.}} = 0.02 \text{ mrad}$$

Hence, using data we could measure the resolution of the experimental set-up. Fig. 50 shows the energy dependence of the resolution. The UA9 apparatus used for this test beam, was not developed specifically

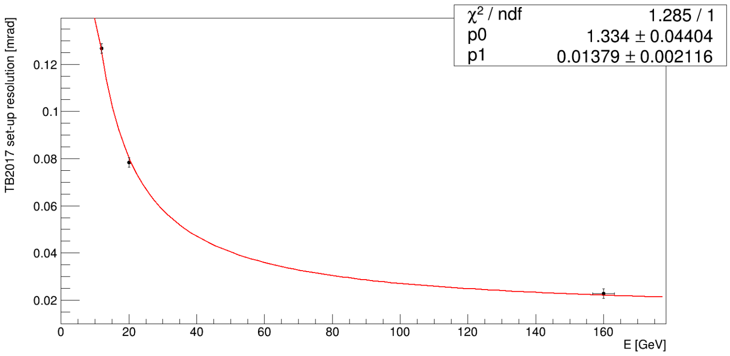

Figure 50: Apparatus resolution as a function of the beam-energy.

to accomplish our requests but it was designed for single track deflection measurements of high-energy particles in crystals. However Fig. 50 shows that with 160 GeV μ^+ we could obtain an overall angular resolution compatible with 0.02 mrad, which is the resolution we expect to achieve using a $\sim 150 - 180$ GeV beam in the final experiment. The fitting function used to estimate the energy dependence of the overall resolution is

$$\sigma = \frac{p[0]}{E} + p[1]$$

It is important to underline that this resolution measurement was possible thanks to the large dataset acquired during alignment runs. This result, based on the gaussian approximation of the multiple scattering, not only allows to confirm that in a single module of the final experimental set-up we can obtain an overall resolution of 0.02 mrad, but also can be used to separate multiple scattering and intrinsic effects on resolution. More precisely, we could verify that $E\sigma = const$ and from the limit at high (infinite) energy, given by $p[1]$, we could also give an estimate of the intrinsic resolution of the full apparatus. However an accurate description of the multiple scattering effect is mandatory to achieve the desired precision on a_μ^{HLO}. More precisely we have that the final resolution on the angular measurement is given by the convolution of the intrinsic resolution of the trackers and the effect from multiple scattering. These two contributions are statistically independent, thus we have

$$\sigma_\theta = \sqrt{\sigma_{MS}^2 + \sigma_{intr.}^2}$$

Multiple scattering angular distribution has a gaussian core, as shown above, and tails which need to be described with an additional component to the normal distribution. Hence, to describe better the multiple scattering, we studied an analytical function capable to fit the entire shape of the angular distribution. In literature there are few works concerning this subject, especially because of the difficulty in retrieving an analytical expression to describe experimental data with good agreement outside core region. Works by Früwirth and Regler [36] and Liendl [37] use complex models based on two gaussians or one gauss distribution and a cos-like function to describe tails. These models have been implemented in our analysis but rely only on specific use-cases and are strongly dependent on input parameters and on target properties. A more elegant model proposed by Berger et al. [38] exploits the convolution of a gaussian distribution and a Student's t distribution to parametrize both the effect of the apparatus and the multiple scattering to describe with good accuracy experimental data. In this work we adapted the latter model to our case with proper adjustments and we obtained an analytical function capable to describe data both in core and tails.

In this model we take into account separately the effect of the silicon telescope and the effect of the target. More precisely the analytical function used to fit data is given by the convolution of these two contributions:

$$f(\theta) = f_{\text{telescope}}(\theta) \otimes f_{\text{target}}(\theta)$$

The contribution of the experimental set-up was studied using alignment runs, which have a statistic lower than runs with target: this could affect the result of the fit, especially in tails where statistics is very poor. Hence, in order to validate the model, it was also applied to Monte Carlo simulations and returned result in agreement with those obtained with data. As already observed in eq. 16 the core of the distribution is modeled with a gaussian centered at zero and with σ depending on the multiple scattering effect and equal to eq. 15, the large tails are taken into account using a Student's t distribution:

$$\begin{aligned} f_{\text{telescope}}(\theta) = N \Bigg(& (1-a)\frac{1}{\sqrt{2\pi}\sigma_G} e^{-\frac{(\theta-\mu)^2}{2\sigma_G^2}} + \\ & + a \frac{\Gamma(\frac{\nu+1}{2})}{\sqrt{\nu\pi}\sigma\Gamma(\frac{\nu}{2})} \left(1 + \frac{(\theta-\mu)^2}{\nu\sigma^2}\right)^{-\frac{\nu+1}{2}} \Bigg) \end{aligned} \tag{17}$$

Where N is the overall normalization, σ and σ_G the width of the Student's t and gaussian distributions respectively, ν the tail parameter of the t distribution and μ the common mean and a which is the relative fraction of the Student's t. Using `ROOT` for the analysis we have a function with 7 parameters since we used the `gaus` function of the `TF1` class:

```
fNT = [0]*((1-[1])*gaus(2)+[1]*TMath::Gamma(([5]+1)/2)/
(sqrt([5]*TMath::Pi())*[6]*TMath::Gamma([5]/2))*
pow(1+pow(x-[3],2)/([5]*[6]*[6]), -([5]+1)/2))
```

Thus, in our case the overall relative fraction will be given by the product of the parameter $(1-a)$ with the normalization factor of the

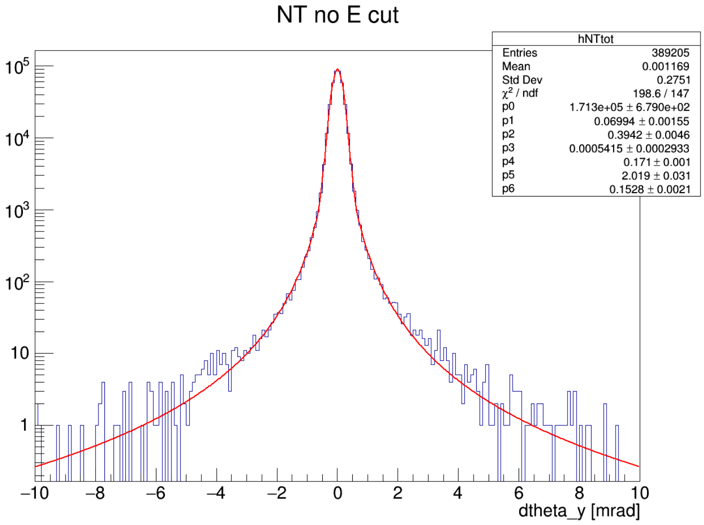

Figure 51: Fit with (17) of the yOz angular distribution of 12 GeV e^- in the apparatus without target.

`gaus()` function. Fig.51 shows the fitted yOz angular distribution for the Monte Carlo simulation of 12 GeV electrons without target. The result of the fit shows good agreement between the analytical model and data, with a good value of $\chi^2/NDF = 198.6/147$. All the fitting parameters are consistent within their uncertainties. The goodness of fit is confirmed by the meaning of the parameters itself, especially a: namely `p[1]`. We recall that the relative fraction of the gaussian is $1 - a$, in this case

$$p[1] = a = 0.069 \pm 0.002$$

Which means that from the Monte Carlo simulation we can estimate the expected fraction of the multiple scattering effect coming only from the experimental set-up. In this case we retrieve a 7% contribution from multiple scattering, while the gaussian approximation for the core is valid with a relative fraction of 93%. The presence of the target has to be taken into account using the convolution of eq. (17), which accounts for the Si telescope and air, with a Student's t distribution:

$$f(\theta) = N \int f_{\text{telescope}}(\theta - \tau) \frac{\Gamma(\frac{\nu+1}{2})}{\sqrt{\nu\pi}\sigma\Gamma(\frac{\nu}{2})} \left(1 + \frac{\tau^2}{\nu\sigma^2}\right)^{-\frac{\nu+1}{2}} d\tau \quad (18)$$

Which depends on 3 additional parameters: the overall normalization N, the width σ and the tail parameter ν of the Student's t distribution. We have implemented the convolution of the two functions using the `TF1Convolution` object of the `TF1` class in `ROOT`, which takes as arguments two `TF1` and computes their convolution. Thus, in our case we have

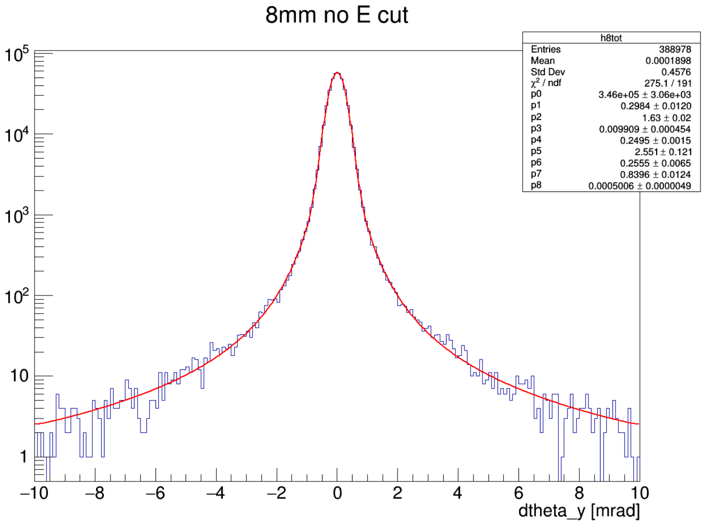

Figure 52: yOz angular distribution fit with (18). Monte Carlo simulation of 12 GeV e^- on 8mm C target.

```
TF1Convolution *f8_conv =
   new TF1Convolution("setup", "target", -10.,10., true);
```

In the declaration above we construct a `TF1Convolution` object, which computes the convolution of the `setup` function and the `target` one, namely those expressed in eq. (17) and eq. (18). Using this expression we obtained good fits both on experimental data and on Monte Carlo simulation. Fig. 52 and 53 show the results of the fit on simulated angular distributions, while Fig. 54 and 55 present the results on experimental data for the same cases. Fit parameters from experiment are in good agreement, within their uncertainties, with those expected from the simulation. Even if the main purpose of our study was to develop a full-simulation capable of describing data within 1% level, we also worked on this analytical approach to understand the possibility to retrieve a mathematical function which could describe data in a wider range with a better agreement outside the core region. The model proposed here fits both data and simulation in a wide range, which covers entirely the statistics available, and returns parameters in agreement for the two cases. It is worth to underline that a further understanding of the problem using this approach was limited by the precision of the `GEANT4` simulation. As we have pointed out in Sec. 4.2.2, the effect of the multiple scattering when the target is thick hides the description of multiple scattering effects in the experimental set-up and gives more precise results in the comparison with data. This imprecision reflects on the results of the fit, since their agreement improves increasing target thickness as shown in Fig. 56 for the ratio MC/data of the gaussian normalization and width.

This observation points toward an inaccurate description of the experimental set-up, which dominates on the multiple scattering effect

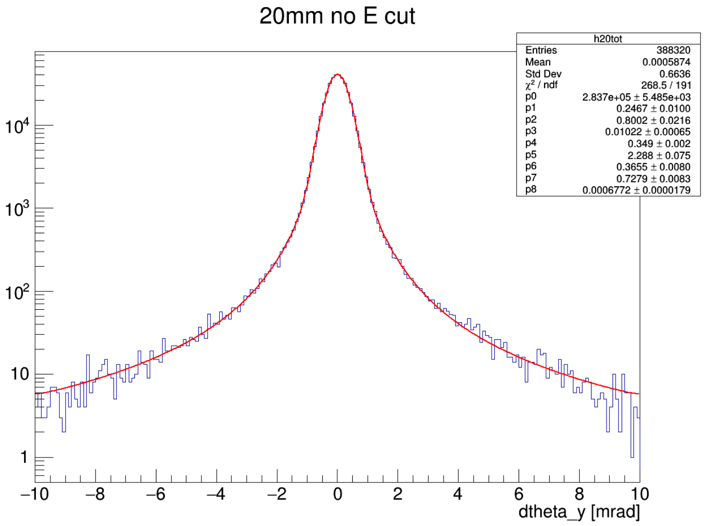

Figure 53: yOz angular distribution fit with (18). Monte Carlo simulation of 12 GeV e^- on 20mm C target.

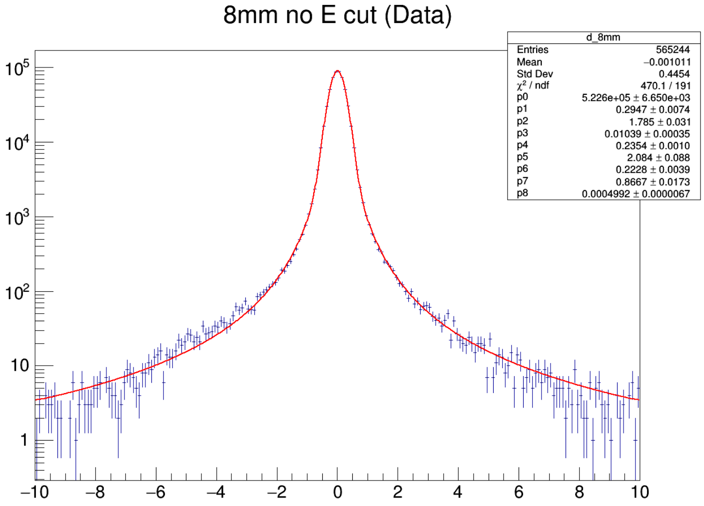

Figure 54: yOz angular distribution fit with (18). Experimental data: 12 GeV e^- on 8mm C target.

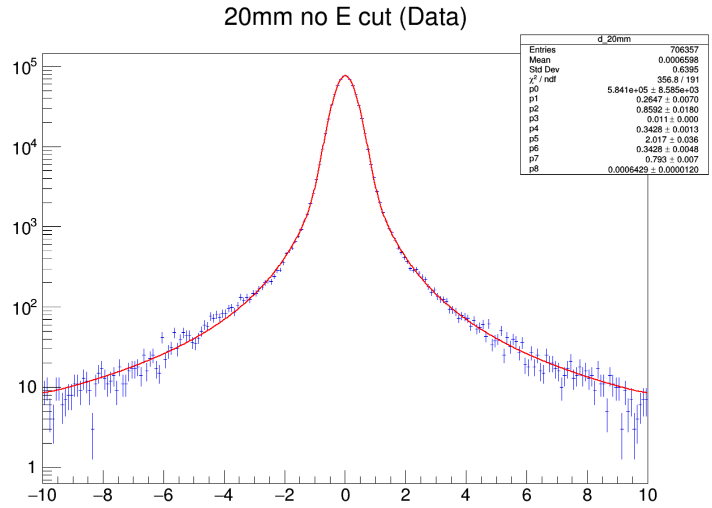

Figure 55: Fit with (18). Experimental data: 12 GeV e^- on 8mm C target.

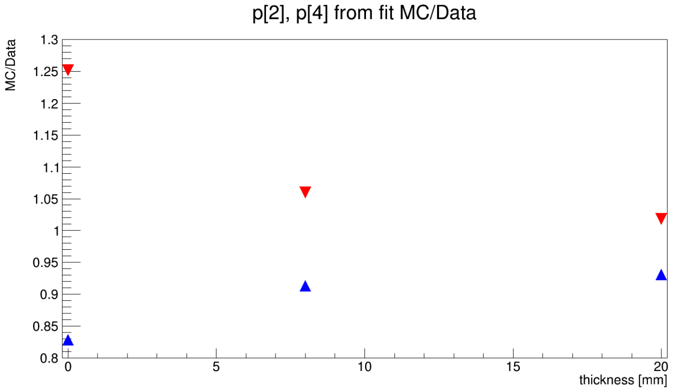

Figure 56: MC/Data ratio of $p[2]$ and $p[4]$ from eq. (18). Blue is $p[4]$ and red is $p[2]$ and represent the normalization parameter of the gaussian distribution and its width σ_G.

in low thickness targets. Hence the analytical approach turns out to be an useful tool to understand better the multiple scattering effect on the angular distribution.

4.2.4 $\mu - e$ *elastic scattering*

The multiple scattering effect has to be taken into account also in tracking. More precisely, one has to reconstruct trajectories starting from hits recorded on Si trackers and these hits are affected by the multiple scattering in target, but also in trackers. The result is that errors are correlated from one layer to the other. There exist two different approaches in tracking [39]:

- **Standard fit:** Takes into account only the measurement errors and their covariance matrix for reconstruction. Eventually contributions from multiple scattering are added;
- **Optimal fit:** Multiple scattering errors are taken into account from the beginning using the complete $n \times n$ covariance matrix.

It is clear that the second approach, when applicable, has to be preferred to the first one as it allows to obtain more sound results and not to underestimate multiple scattering effects on errors. In our case, both the geometry and the physics studied were simple enough to adopt the optimal fit approach. At this point it is worth making an observation: the main purpose of this test beam was to investigate multiple scattering effects on $\mathcal{O}(10\text{ GeV})$ electrons and not to measure the $\mu - e$ elastic interaction. The muon run(s) (see Tab. 3) was collected during the last day of test beam with an apparatus built to work with single tracks and not to perform scattering measurements. What is presented in the following is the analysis of this μ^+ run, which was carried on to test the overall procedure and to understand whether this first proof-of-concept of the set-up, in this test beam not specifically developed for our purposes, confirmed the feasibility of the $\mu - e$ scattering events reconstruction or not. In detail, given n layers with distance $l_{i,j}$, the track deviation per plane is given by

$$\delta x_0 = 0$$

$$\delta x_1 = \theta_1 l_{1,0}$$

$$\delta x_n = \theta_1 l_{n,0} + \theta_2 l_{n,1} + \cdots + \theta_n l_{n,n-1} = \sum_{j=1}^{n} \theta_j l_{j,j-1}$$

Hence the covariance matrix of errors is

$$\begin{aligned} V_{i,j} &= \langle \delta x_i \delta x_j \rangle = \\ &= \int \left(\sum_{i=1}^{n} \theta_i^2 l_{n,i-1} l_{m,i-1} P(\theta_1, \ldots, \theta_n) d\theta_1 \ldots d\theta_n \right) = \\ &= \theta_0^2 \left[(z_i - z_1)(z_j - z_1) + \cdots + (z_i - z_{i-1})(z_j - z_{i-1}) \right] \end{aligned} \tag{19}$$

Where θ_0 is the multiple scattering mean angle given by eq. (15). The error correlation matrix, which depends only on the system configuration is given by

$$\rho_{ij} = \frac{\langle \delta x_i \delta x_j \rangle}{\sqrt{\langle \delta x_i^2 \rangle \langle \delta x_j^2 \rangle}}$$

The tracking procedure implemented is based on the optimal fit approach and uses directly the covariance matrix V_{ij} to reconstruct tracks starting from hits on silicon trackers. Given a beam traveling on the z direction, in absence of an external magnetic field the track is a straight line. Since the two views are independent, it is possible to obtain these coordinates from a least squares fit

$$x = x_0 + \alpha_x z$$

$$y = y_0 + \alpha_y z$$

Using hits measurements (x_i, σ_{x_i}), (y_i, σ_{y_i}), z_i and their covariance matrix V_{ij} as input data, the χ^2 for the two views can be written in matrix form as

$$\chi^2 = (X - HA_x)^T V^{-1} (X - HA_x)$$

Where

$$X = \begin{pmatrix} x_1 \\ x_2 \\ \vdots \\ x_n \end{pmatrix}, \; H = \begin{pmatrix} 1 & z_1 \\ 1 & z_2 \\ \vdots & \vdots \\ 1 & z_n \end{pmatrix}, \; A_x = \begin{pmatrix} x_0 \\ \alpha_x \end{pmatrix}$$

and the V matrix is the one defined in eq. (19). The X vector represents the measured hits and the H vector the detector geometry in case of a sequence of n layers positioned at z_i along beam axis. We assume that no error has been introduced in the measurement of the positions z_i. The least squares criterion allows to obtain an estimate of A_x. More precisely, we have to impose

$$\frac{\partial \chi^2}{\partial A_x} = 0 \Leftrightarrow H^T V^{-1} (X - HA_x) = 0$$

Which gives the fit results A_x as solution:

$$A_x = \left(H^T V^{-1} H\right)^{-1} \left(H^T V^{-1} X\right)$$

With errors on these parameters given by definition:

$$E_{A_x} \equiv \left\langle \delta A_x \delta A_x^T \right\rangle = \left(H^T V^{-1} H\right)^{-1}$$

We have implemented this procedure for the two views in a `ROOT` macro, using the `TMath` and `TMatrixD` classes to implement the operations needed to evaluate A_x. Thus, the structure of the V matrix is:

```
V(0,0) = errY2; V(0,1) = 0; V(0,2) = 0;
V(1,0) = 0; V(1,1) = errY3; V(1,2) = errY34;
V(2,0) = 0; V(2,1) = errY34; V(2,2) = errY4;
```

Where

```
double sigma2 = 0.0069; //in mm
double errY2 = pow(sigma2,2);
double thickness_Si = 0.064; //2 views, 320um each
double X0_Si = 9.368; // in cm!
double errY3 = pow(thetaMS*Dz23,2.)+errY2;
double errY4 = pow(thetaMS*(Dz23+Dz34),2.)+pow(thetaMS*Dz34,2.)+errY2;
double errY34 = Dz23*(Dz23+Dz34)*thetaMS*thetaMS;
```

Where is clear the correlation introduced by multiple scattering on planes: it is added to the measurement error on each plane. Moreover, due to the correlation effect introduced by V_{ij} we observe that on the first downstream plane the error coincides with the measurement one, while on the second and third plane is given by the sum of the measurement error on the first plane with the contributions due to multiple scattering. Hence, there is a difference between measurement error and the overall one, especially for the last plane. The UA9 apparatus is characterized by Si trackers with the following measurement errors:

$$\sigma_2 = 6.9\,\mu m$$

$$\sigma_3 = 6.9\,\mu m$$

$$\sigma_4 = 40\,\mu m$$

We would use these uncertainties directly if we had to work with the standard fit approach, but having at disposal a description of multiple scattering, along with a method to deal with it in tracking, we could work directly with the optimal fit approach, as stated above. The effect in target here is not taken into account, as we reconstruct the incoming track from the two upstream planes and the outgoing one from the downstream planes.

To detect events of $\mu - e$ scattering, we decided to study all those events with 1 hit registered by the upstream planes and 2 hits by the downstream ones. The selection of this topology is dictated by the fact that the apparatus does not have stereo planes to disambiguate hits. In fact the UA9 apparatus consists of three downstream trackers which measure x and y coordinates in the horizontal and vertical planes, but there are no stereo planes to solve ambiguities in the association (x_i, y_j). This introduces unavoidably *ghost hits*, which complicated the analysis. More precisely, raw data before the alignment have x and y views independent one from the other and only post-processing we are able to determine the correlation (x, y). Let us assume that for a raw event we have multiplicity 2 in the downstream planes. Then the tracker has registered two x-coordinates x_1, x_2 and two y-coordinates y_1, y_2. Starting from a given x, the alignment algorithm creates all

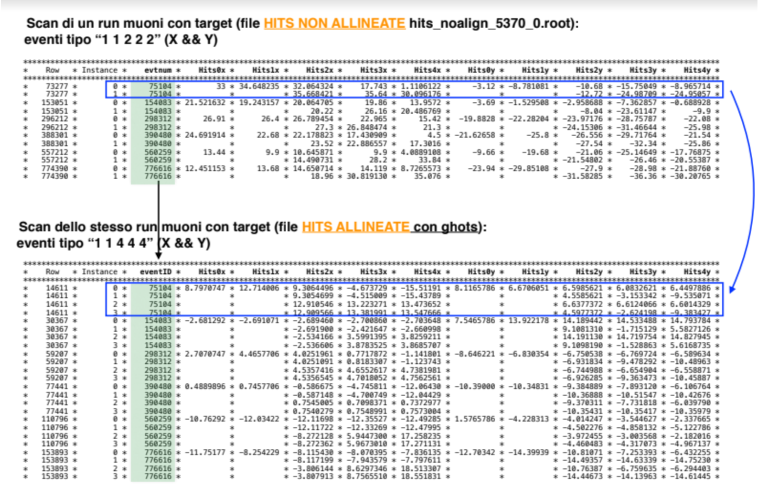

Scan di un run muoni con target (file HITS NON ALLINEATE hits_noalign_5370_0.root):
eventi tipo “1 1 2 2 2” (X && Y)

```
**********************************************************************************************************************************************************
*    Row   * Instance *   evtnum *    Hits0x *    Hits1x *    Hits2x *    Hits3x *    Hits4x *    Hits0y *    Hits1y *    Hits2y *    Hits3y *    Hits4y *
**********************************************************************************************************************************************************
*    73277 *        0 *    75104 *        33 * 34.648235 * 32.064324 *    17.743 * 1.1106122 *     -3.12 * -8.781081 *    -10.68 * -15.75049 * -8.965714 *
*    73277 *        1 *    75104 *           *           * 35.668421 *     35.64 * 30.096176 *           *           *    -12.72 * -24.98709 * -24.95057 *
*   153051 *        0 *   154083 * 21.521632 * 19.243157 * 20.064705 *     19.86 *   13.9572 *     -3.69 * -1.529508 * -2.958688 * -7.362857 * -0.688928 *
*   153051 *        1 *   154083 *           *           *     20.22 *     26.16 * 20.486769 *           *           *     -8.04 * -23.61147 *      -9.9 *
*   296212 *        0 *   298312 *     26.91 *      26.4 * 26.789454 *    22.965 *     15.42 *  -19.8828 * -22.28204 * -23.97176 * -28.75787 *    -22.08 *
*   296212 *        1 *   298312 *           *           *      27.3 * 26.848474 *      21.3 *           *           * -24.15306 * -31.46644 *    -25.98 *
*   388301 *        0 *   390480 * 24.691914 *     22.68 * 22.178823 * 17.430909 *       4.5 * -21.62658 *     -25.8 *   -26.556 * -29.71764 *    -21.54 *
*   388301 *        1 *   390480 *           *           *     23.52 * 22.886557 *   17.3016 *           *           *    -27.54 *    -32.34 *    -25.86 *
*   557212 *        0 *   560259 *     13.44 *       9.9 * 10.645871 *       9.9 * 4.0889108 *     -9.66 *    -19.68 *    -21.06 * -25.14649 * -17.76875 *
*   557212 *        1 *   560259 *           *           * 14.490731 *      28.2 *     33.84 *           *           * -21.54802 *    -26.46 * -20.55387 *
*   774390 *        0 *   776616 * 12.451153 *     13.68 * 14.650714 *    14.119 * 8.7265573 *    -23.94 * -29.85108 *     -27.9 *    -28.98 * -21.88760 *
*   774390 *        1 *   776616 *           *           *     18.96 * 30.819130 *    35.076 *           *           * -31.58285 *    -36.36 * -30.20765 *
```

Scan dello stesso run muoni con target (file HITS ALLINEATE con ghots):
eventi tipo “1 1 4 4 4” (X && Y)

```
**********************************************************************************************************************************************************
*    Row   * Instance *  eventID *    Hits0x *    Hits1x *    Hits2x *    Hits3x *    Hits4x *    Hits0y *    Hits1y *    Hits2y *    Hits3y *    Hits4y *
**********************************************************************************************************************************************************
*    14611 *        0 *    75104 * 8.7970747 * 12.714006 * 9.3064496 * -4.673729 * -15.51191 * 8.1165786 * 6.6706051 * 6.5985621 * 6.0832621 * 6.4497886 *
*    14611 *        1 *    75104 *           *           * 9.3054699 * -4.515009 * -15.43789 *           *           * 4.5585621 * -3.153342 * -9.535071 *
*    14611 *        2 *    75104 *           *           * 12.910546 * 13.223271 * 13.473652 *           *           * 6.6377372 * 6.6124066 * 6.6014329 *
*    14611 *        3 *    75104 *           *           * 12.909566 * 13.381991 * 13.547666 *           *           * 4.5977372 * -2.624198 * -9.383427 *
*    30367 *        0 *   154083 * -2.681292 * -2.691071 * -2.689460 * -2.700860 * -2.703648 * 7.5465786 * 13.922178 * 14.189442 * 14.533488 * 14.793784 *
*    30367 *        1 *   154083 *           *           * -2.691900 * -2.421647 * -2.660998 *           *           * 9.1081310 * -1.715129 * 5.5827126 *
*    30367 *        2 *   154083 *           *           * -2.534166 * 3.5991395 * 3.8259211 *           *           * 14.191130 * 14.719754 * 14.827945 *
*    30367 *        3 *   154083 *           *           * -2.536606 * 3.8783525 * 3.8685707 *           *           * 9.1098190 * -1.528863 * 5.6168735 *
*    59207 *        0 *   298312 * 2.7070747 * 4.4657706 * 4.0251961 * 0.7717872 * -1.141801 * -8.646221 * -6.830354 * -6.750538 * -6.769724 * -6.589634 *
*    59207 *        1 *   298312 *           *           * 4.0251091 * 0.8183307 * -1.123743 *           *           * -6.931834 * -9.478292 * -10.48963 *
*    59207 *        2 *   298312 *           *           * 4.5357416 * 4.6552617 * 4.7381981 *           *           * -6.744988 * -6.654904 * -6.558871 *
*    59207 *        3 *   298312 *           *           * 4.5356545 * 4.7018052 * 4.7562561 *           *           * -6.926285 * -9.363473 * -10.45887 *
*    77441 *        0 *   390480 * 0.4889896 * 0.7457706 * -0.586675 * -4.745811 * -12.06430 * -10.39000 * -10.34831 * -9.384889 * -7.893120 * -6.106764 *
*    77441 *        1 *   390480 *           *           * -0.587148 * -4.700749 * -12.04429 *           *           * -10.36888 * -10.51547 * -10.42676 *
*    77441 *        2 *   390480 *           *           * 0.7545005 * 0.7098371 * 0.7372977 *           *           * -9.370311 * -7.731818 * -6.039790 *
*    77441 *        3 *   390480 *           *           * 0.7540279 * 0.7548991 * 0.7573004 *           *           * -10.35431 * -10.35417 * -10.35979 *
*   110796 *        0 *   560259 * -10.76292 * -12.03422 * -12.11698 * -12.35527 * -12.49285 * 1.5765786 * -4.228313 * -4.014247 * -3.544627 * -2.337665 *
*   110796 *        1 *   560259 *           *           * -12.11722 * -12.33269 * -12.47995 *           *           * -4.502276 * -4.858132 * -5.122786 *
*   110796 *        2 *   560259 *           *           * -8.272128 * 5.9447300 * 17.258235 *           *           * -3.972455 * -3.003568 * -2.182016 *
*   110796 *        3 *   560259 *           *           * -8.272362 * 5.9673010 * 17.271131 *           *           * -4.460483 * -4.317073 * -4.967137 *
*   153893 *        0 *   776616 * -11.75177 * -8.254229 * -8.115430 * -8.070395 * -7.836135 * -12.70342 * -14.39939 * -10.81071 * -7.253393 * -6.432255 *
*   153893 *        1 *   776616 *           *           * -8.117199 * -7.943579 * -7.797611 *           *           * -14.49357 * -14.63339 * -14.75230 *
*   153893 *        2 *   776616 *           *           * -3.806144 * 8.6297346 * 18.513307 *           *           * -10.76387 * -6.759635 * -6.294403 *
*   153893 *        3 *   776616 *           *           * -3.807913 * 8.7565510 * 18.551831 *           *           * -14.44673 * -14.13963 * -14.61445 *
```

Figure 57: Display of hits per plane pre and post alignment. Align data present multiplicity 4 for events with two tracks.

the combinations of this x aligned with the possible y_i registered on the same plane. Hence, in our case we pass from an event with multiplicity $m = 2$ in raw data to an event $m = 4$ in processed data. Fig. 57 shows how these combinations are generated by the alignment procedure. We studied the case in which one primary particle enters the detector (i.e. $m = 1$ on the upstream planes) and exits the target accompanied by a secondary particle (i.e. $m = 4$ on the downstream planes). Starting from 7547926 events we are left with 251 events after the selection 11444 on planes. These events are tracked using the χ^2 minimization presented above: for each event we reconstruct the two particles tracks and we extract their angle with respect the z axis. Since the apparatus records independently the two quantities, one must apply the same tracking procedure to both x and y views. Using the same approach, we tried two different methods to select the $\mu - e$ tracks after the reconstruction. The first method is the most general one, commonly used to solve tracking problems with multiple hits and it works as follows:

- Reconstruct the incoming angle of the primary track using the upstream planes;
- Select an hit on the last plane, x_{4_i} where i is the multiplicity of this hit;
- Compute the χ^2_x values for all the possible combinations $(x_{2_j}, x_{3_l}, x_{4_i})$;
- For all the 64 combinations, compute the sum $\chi^2 = \chi^2_x + \chi^2_y$;
- The two lowest χ^2 values correspond to the two tracks reconstructed;

After the identification of the two tracks, we associate the lowest χ^2 value to the muon and the second lowest to the electron. We extract from fit the two angles θ_x and θ_y of the particle, i.e. the two angles of flight with respect to z. More precisely, we compute θ_μ and θ_e using the vectors in space for the incoming particle and the outgoing ones defined as follow:

$$\overrightarrow{\mu}_i = \begin{pmatrix} x_1 - x_0 \\ y_1 - y_0 \\ z_1 - z_0 \end{pmatrix}, \; \overrightarrow{\mu}_f = \begin{pmatrix} x_4^{fit} - x_2^{fit} \\ y_4^{fit} - y_2^{fit} \\ z_4 - z_2 \end{pmatrix} \Rightarrow \theta_\mu = \arccos\left(\frac{\theta_f \times \theta_i}{\| \theta_f \times \theta_i \|}\right)$$

The second method implemented for the tracking is based on the same procedure as the previous one, with an additional caveat which exploits information from the alignment procedure. In fact, if we look at the bottom part of Fig. 57 we note that the x coordinates are such that one between x_1, x_2 is a ghost hit as well as one between x_3, x_4, while for the y coordinates the same happens with y_1, y_3 and y_2, y_4. This is because of lack of stereo planes for the alignment procedure: the first two x hits are one the ghost of the other because they have been aligned within respect the same y and the same holds for the second two x hits. Hence, if one selects one pair (x_{2_i}, y_{2_j}) then the hits on the second plane associated to the second track are completely determined. The same happens for planes 3 and 4. Hence, with this second approach we introduce an additional constraint on the selection: we have to look to 32 combinations instead of 64 because when we select one pair, we already have determined hits associated to the second track. The second advantage of this method is that we can introduce a correlation between the x and y coordinates, because when we select one between x_1 and x_3 we automatically know which is the associated y (y_1 or y_2). Using this information the χ^2 minimization criterion is the following: for the 32 combinations tracked, we look for the one which has $\chi_x^2 + \chi_y^2$ lower than a certain value ($\chi^2 \leq 15$ in our case). In all the cases studied there is only one track which satisfies this criterion: we identify that track as the muon, while the second track automatically determined from this one is the one associated with the electron. Fig. 58 shows the $\theta_e - \theta_\mu$ plot produced using the two different methods. Both the tracking algorithms allow to see the correlation $\theta_e - \theta_\mu$. The main difference is in the bottom-left corner of the correlation plot, where the two procedures return consistently different reconstructions. The kinematic curve drawn in the plot represents the $\theta_e - \theta_\mu$ correlation curve for $E_\mu = 160$ GeV and it is worth to stress that it is drawn only for graphical purposes. Its analytical expression can be derived from (9) and (10):

$$\theta_\mu = \arcsin\left(\sqrt{\frac{E_e'^2 - m_e^2}{E_\mu'^2 - m_\mu^2}} \sin\theta_e\right) \tag{20}$$

Where E_e' and E_μ' refer to the electron and muon final energies respectively. It is important to note that the kinematic of the event, as well as

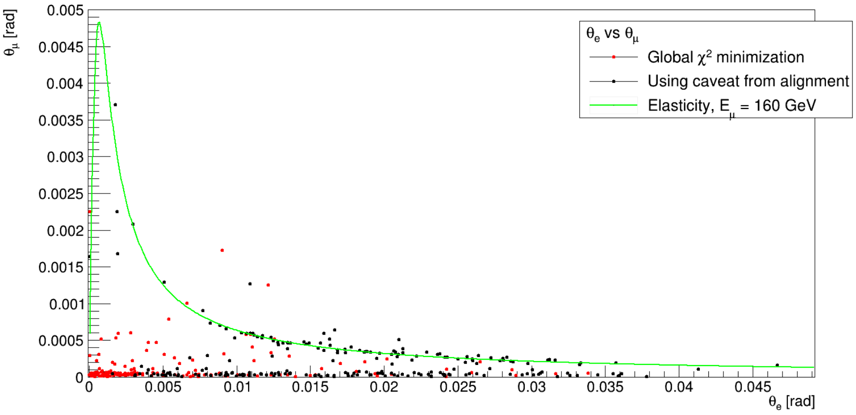

Figure 58: $\theta_e - \theta_\mu$ plot reconstructed using the tracking algorithm presented. 251 events reconstructed.

the two equations used to determine this relation, do not depend on the uncertainty on the initial muon momentum, but experimentally and in the data analysis this is one of the aspects which needs to be controlled to ensure a final systematic accuracy to a 10^{-5} level. In the Test Beam data, as well as in the final experiment, one has to take into account the energy spread of the muon beam: every point in the plot should be positioned according to the energy of the incoming muon which undergoes the $\mu - e$ scattering process. It is also important to stress the qualitative spirit of this plot: with it we aim to prove that the signal region is distinguishable with an apparatus similar to the one we intend to use. However, with such a low statistics it is impossible to perform any quantitative study on the systematics of the energy spread and the multiple scattering effects on resolution. Hence, the dispersion of the points reconstructed along the kinematic curve shown in Fig. 58 can only be explained as the natural effect of the tracking procedure and it is dominated by the severe multiple scattering of low-energy electrons and by the apparatus intrinsic resolution (see Fig. 50). Notwithstanding the differences in tracking for points at low angles, we observe that both the methods always return an electron track which has a large value of χ^2 associated. While in the second method this does not affect the selection, which always has positive results since there is always only one track with $\chi^2 < 15$, it could generate some ambiguities when using the most general method. In fact, for some events it happens that the lowest χ^2 is associated to a muon track, but that the second one, being the tracking of electrons more problematic, can return worse track parameters. If there were the possibility to eliminate ghost hits, the two procedures would have returned exactly the same results. We have repeated this study using `GEANT4` simulation and we could validate the tracking algorithm developed: the tracks identified as muon and electron by the general

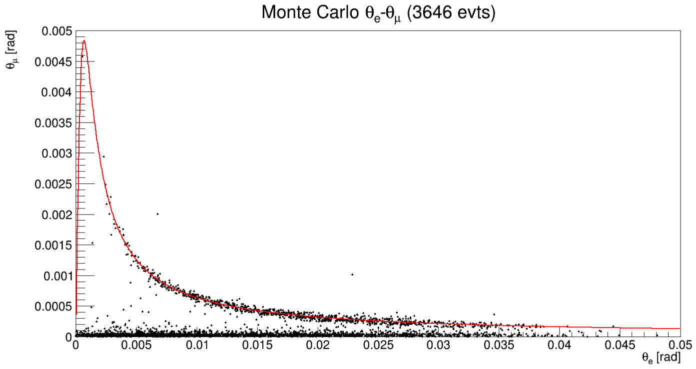

Figure 59: $\theta_e - \theta_\mu$ correlation plot from Monte Carlo. 10^8 muons simulated, 3646 events selected and reconstructed.

method, were always confirmed to be good associations using the simulation.

In order to validate this strategy, we also repeated the same analysis on simulated data. 10^8 muons were simulated in each run and the angles of the tracks coming out from the graphite target were registered. The application of the 11222 selection for tracking leaves us with 3646 events, as shown in Fig. 59. Here the selection is 11222 instead of 11444 as above, because in GEANT we have no ghost hits and the association hits-particle is unambiguous. The two tracking methods presented above converge on the same solution, as there are no ghost hits and the two tracks are completely determined by their `particleID`, uniquely defined in `GEANT4`. The simulation confirms the validity of the tracking procedure used and gives result in agreement with data. We see that the large number of events present in the bottom-left corner of Fig. 58 is still present in the Monte Carlo reconstruction. Further details are presented in the following section and in 4.2.4.2, where we present a study of the `GEANT4` simulation to describe the different classes of μ-interactions which populate the $\theta_e - \theta_\mu$ plot as well as possible kinematic cuts which allow to reject background in favor of elastic events. We see that the maximum θ_e measurable depends on the experimental set-up acceptance, given by the sensors dimensions of 3.8×3.8 cm^2, which allow to measure up to $\theta_e \simeq 40 - 45$ mrad. Electrons with angles equal or grater than this value are emitted outside the acceptance of the detector. Moreover the bottom band of the plot is highly populated due to background effects (studied in detail in sec. 4.2.4.2) but also because of multiple scattering: electrons emitted in the target at large angles ($\theta_e > 30 - 35$ mrad) could possibly re-enter the detector acceptance due to multiple scattering. The main scope of this Test Beam was to study the effect of multiple scattering of $\mathcal{O}(10$ GeV$)$ electrons in graphite target and with the UA9 set-up we did not intend to perform a measurement of $\frac{d\sigma}{d\theta_e}$. This exercise was done to prove that an apparatus with structure

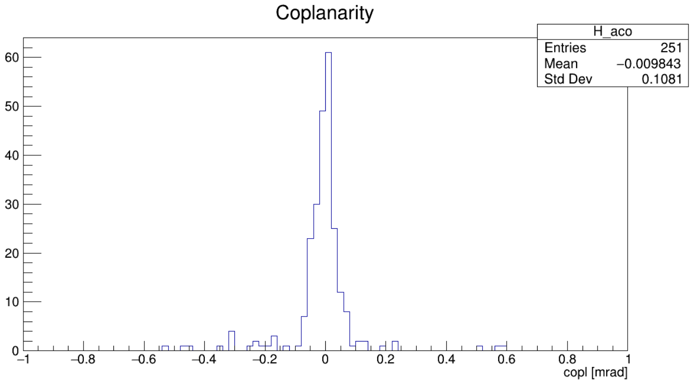

Figure 60: Coplanarity distribution of $\mu - e$ reconstructed events.

similar to the one used fo this Test Beam could be used to track the $\mu - e$ scattering and to reconstruct the kinematic plot presented in Fig. 14, which is going to be the fundamental handle to perform the final measurement on a_μ^{HLO}.

4.2.4.1 *Kinematic cuts*

This exercise allowed us to show the possibility to see our signal (the $\mu - e$ elastic scattering) using an experimental set-up consisting of a proof-of-concept of one module of the final MUonE apparatus. In order to ensure the control of systematic uncertainties to a 10^{-5} level in the final measurement, it is fundamental to control the ratio signal/background to this level. Moreover we have to define a criterion which allows to select signal events, to reject background or to determine the corrective factor to be applied for each bin to normalize $\frac{d\sigma}{d\theta_e}$ to the signal fraction. Hence, we studied different cuts based on the closed kinematic of the scattering. The first observable which could be used for this study is the planarity of the event: the $\mu - e$ elastic scattering is a pure two-bodies scattering and the two particles should be co-planar. As a consequence of multiple scattering, some of the events could become a-planar and should be discarded in the analysis. We used the following definition for the acoplanarity:

$$\mathcal{A} = \frac{\pi}{2} - \arccos\left(\frac{\vec{\mu}_i \cdot (\vec{\mu}_o \times \vec{e}_o)}{\mid \vec{\mu}_i \mid \cdot \mid \vec{\mu}_o \times \vec{e}_o \mid}\right) \tag{21}$$

Where $\vec{\mu}$ and $\vec{e}$ are the vectors in space of the muon and electron respectively and the subscripts o and i refer to the outgoing and incoming tracks. Fig. 60 shows the distribution of this observable for the 251 events reconstructed as described above. The secondary which accompanies this primary is, for most of the cases, the electron produced within the $\mu - e$ scattering in the target. Fig. 61 shows the result of a cut at $\mid \mathcal{A} \mid < 0.1$ mrad. First of all we observe that this cut appears very effective to select $\mu - e$ elastic scattering events with a

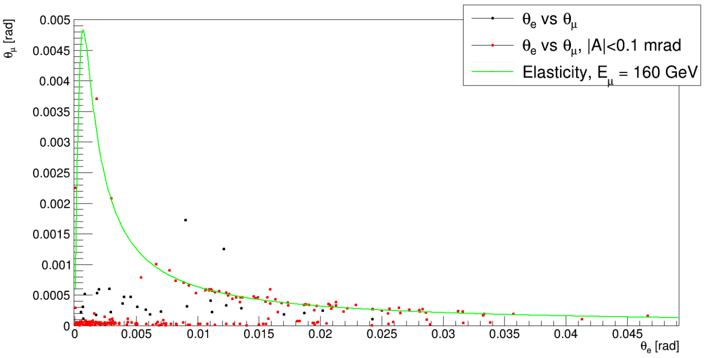

Figure 61: 251 reconstructed $\mu - e$ events (251) without cut (black) and with $\mid \mathcal{A} \mid < 0.1$ mrad cut applied (217, blue).

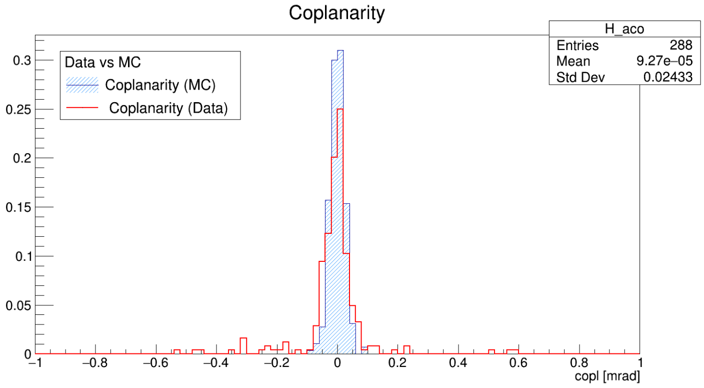

Figure 62: Normalized for data (red) and Monte Carlo (blue).

multiple scattered electrons. In this topology the two particles are no longer co-planar and hence the expected angular correlation is broken and we reconstruct these points under the elastic curve. In order to validate this result we used the `GEANT4` simulation of 10^8 incoming muons of 160 GeV. With the same fiducial cuts (see 4.2.1) and the same tracking procedure used for data we were able to reconstruct 3646 events, as shown in Fig. 59. The coplanarity of these events, calculated using eq. 21, is shown in Fig.62 normalized and superimposed to the $\mathcal{A}$ distribution from data. The Monte Carlo simulation confirms that, with this apparatus and the selection on hits (11444) used to select only a specific sub-set of $\mu - e$ events, the coplanarity cut allows to reject those events under the elastic curve, but does not introduce an effective criterion to select elastic events which present the expected angular correlation. A more sophisticated cut based on the kinematics of the $\mu - e$ scattering is the so called $D\theta$ cut, which is based on the distance of each point from the theoretical curve. The use of this cut has several advantages, as it would also allow to define a band along the elastic curve to reject large part of the background events. More precisely, let $(\theta_e^{exp}, \theta_\mu^{exp})$ the two reconstructed angles. Using the

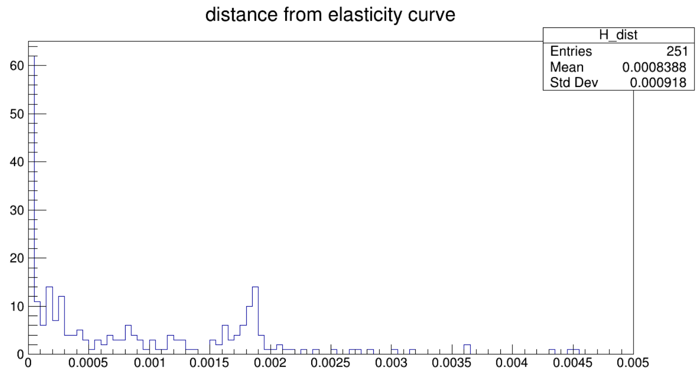

Figure 63: $D\theta$ distribution for the 251 events reconstructed from data.

analytical expression given in eq. (20) we can calculate the expected value for the muon angle, associated with the measured electron angle. We will use the closest distance from $(\theta_e^{exp}, \theta_\mu^{exp})$ to the tangent line as an estimate of the closes distance between the point and the theoretical curve. Hence, for each point we have calculated $D\theta$, id est the perpendicular distance from the point to the kinematic curve:

$$D\theta = \frac{\mid \theta_\mu^{meas} - \theta_\mu^{theo}(\theta_e) \mid}{\sqrt{d\theta_\mu^{theo^2}(\theta_e) + 1}} \tag{22}$$

Where $d\theta_\mu^{theo}(\theta_e)$ is the derivative of eq. (20) with respect to θ_e. Fig. 63 shows the distribution of $D\theta$ for the 251 $\mu - e$ events reconstructed from data: most of the points are in the first few bins, where the distance point-curve is almost null, but a second bump at $D\theta > 5 \times 10^{-4}$ mrad can be observed. With reference to Fig. 58 we understand that this second bump corresponds to the points in the bottom-left part of the plot: these points have large distance from the curve and we do expect them also from theoretical calculations (see Fig. 15). In the following section (4.2.4.2) we study the different μ-interactions and how they populate the $\theta_e - \theta_\mu$ plot and we show that actually those are $\mu \to \mu e^+ e^-$ events. Moreover some of these, as well as e^- coming from other interactions, could also fall on the elastic band: so it is fundamental to distinguish the different classes of interactions and to define a cut which allows to reject background as much as possible.

The result is presented in Fig. 64: this cut is highly selective in the region $\theta_e < 10$ mrad, $\theta_\mu < 0.5$ mrad. The observable $D\theta$ is commonly used to select only specific regions around a given theoretical one, as it was done by the NA7 collaboration to measure the pion form-factor [40]. In our case we used a slightly simplified definition of $D\theta$, which depends on the derivative of the theoretical distribution, which is almost infinite for $\theta_e \to 0$. As a result, in Fig. 64 we observe some points (13) in the very bottom corner of the plot: these points are not rejected because for these angular values the definition of $D\theta$

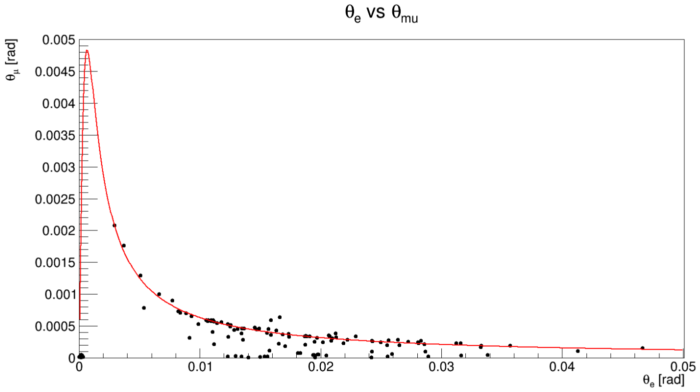

Figure 64: $\theta_e - \theta_\mu$ correlation plot for $D\theta$<5×10^{-4} mrad.

is inconsistent. However, these points can be interpreted as muons which travel undisturbed in the detector or with the emission of very low energy electrons which get re-absorbed. Eventually with this cut one can save entirely the region around the elastic band and a sub-set of background events with $\theta_e > 10$ mrad, which are $\mu - e$ events with an electron which underwent severe multiple scattering.
In order to validate this observable we used our `GEANT4` simulation, with an additional advantage: in data we do not know the initial energy of the muon, hence the theoretical curve used to evaluate $D\theta$ is the nominal one at $E_\mu = 160$ GeV (same curve drawn in Fig. 58); in the simulation we can extract, event by event, the initial beam momentum and use it to evaluate $D\theta$. This information is fundamental to understand if the energy spread, which is quoted but not measured in our experiment, is relevant to our selections and is enough to achieve the expected control on systematics. Fig. 65 shows the $D\theta$ distribution normalized for data and simulation: the distance is calculated differently in the two cases, with the MC result more precise than data. We observe that the trend of these distributions is the same. Moreover this cut does not have any direct link to other interesting observable, such as energy or angle of the two particles, but it is a sharp cut which rejects all the events under the $\theta_e = 10$ mrad, $\theta_\mu = 0.5$ mrad region.

The application of the $D\theta < 5 \times 10^{-4}$ mrad cut on the 3646 events from the simulation is shown in Fig. 66 and it confirms the previous observation: this is a quite sharp cut in the lower region of the plot. This cut leaves untouched all the points on the theoretical curve, i.e. signal, as well as all the points with $\theta_e > 10$ mrad. In the following section we analyze these events in order to understand if they are from $\mu - e$ scattering or if they are background events, coming from other μ-interactions. It is fundamental to answer this question since we have to know if these events could be cut (and how) or if we must determine a corrective factor based on the relative ratio signal/background to correct the $\frac{d\sigma}{d\theta_e}$ measurement.

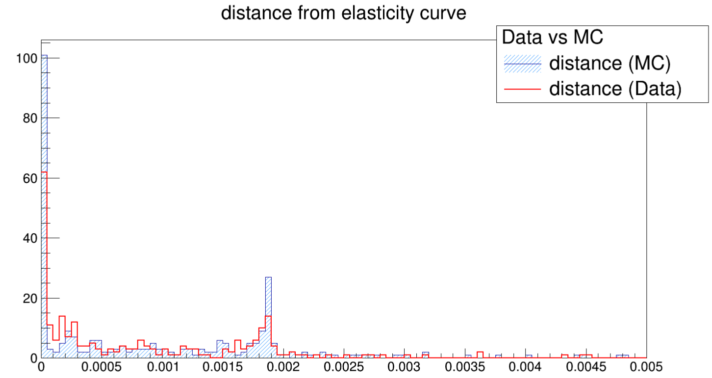

Figure 65: Normalized $D\theta$ distributions for data (red) and Monte Carlo (blue).

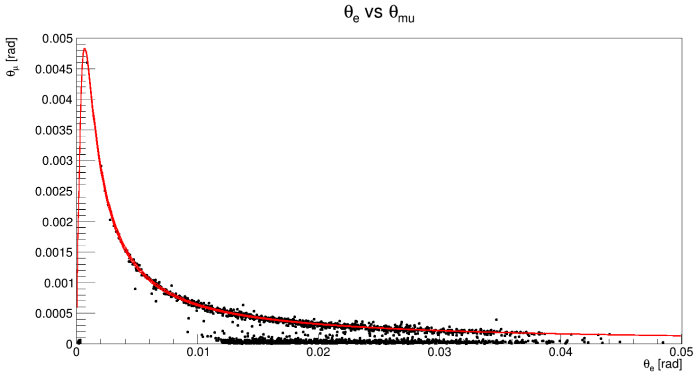

Figure 66: $D\theta$ cut applied to the 3646 $\mu - e$ events from Monte Carlo simulation.

Fig. 66 allows us also to clarify the question about the energy spread. In this plot we reproduced not only the theoretical curve at $E_\mu = 160$ GeV, but also the two curves at $E_\mu = 164$ GeV and $E_\mu = 156$ GeV, i.e. $\frac{\sigma_{E_\mu}}{E_\mu} = 2\%$ as quoted by machine experts. The three curves are almost indistinguishable: the result is that the $D\theta$ distribution for data and for Monte Carlo do not present any substantial difference (see Fig. 65). The dispersion of the points around the curve is the combined effect of the energy spread, the apparatus intrinsic resolution and the multiple scattering effect, which dominates for most of the θ_e values. As stated in sec. 4.1, a nominal precision on the incoming beam momentum of $2-3\%$ does not present a limit in the possibility of achieving our measurement with the desired precision as the effect of the energy spread is negligible within respect to the other sources of systematics which we must take into account and control to achieve a final level of 10^{-5}.

In this Test Beam we did not have at disposal a calorimeter to create an energy matrix of the secondaries and possibly apply it to data in order to reject some background at low energies. Due to this reason we had to study these kinematic cuts which could help us to select only the signal region, i.e. around the elastic curve, and to reject background and multiple scattering events which compose the lower region of the plot. Acoplanarity does not appear to be an highly discriminating variable, while $D\theta$ seems to be a good candidate to reject those e^+e^- events which populate the bottom-left corner of the plot. However the cut in distance is not an effective criterion to get rid of events of multiple scattering at $\theta_e > 10$ mrad, as shown in Fig. 66. This situation contains two different problems: events affected by multiple scattering populate the lower band of the plot and seem to be constrained by a θ_μ value; events on the elastic curve, without the possibility of distinguishing charge and/or energy, could possibly be background events which need to be corrected using the simulation bin per bin. Hence, the presence of the highly-populated band can be investigated and possibly filtered but we would still remain with a population which essentially is unknown in the ratio signal/background on the elastic band.

For what concerns the lower band of the $\theta_e - \theta_\mu$ plot: all these events are characterized by a muon which traverses the detector almost unperturbed ($\theta_\mu \simeq 0$ mrad) and electrons which are emitted at uniform angles between $\theta_e \simeq 10$ mrad and $\theta_e \simeq 30$ mrad. Fig. 67 shows the distribution of the muon angles for the 251 events reconstructed. It appears as if there were two populations: the first one ($\theta_\mu < 0.1$ mrad) is characterized by low angle particles, which travel almost without any interaction in the detector, while the second one ($\theta_\mu > 0.1$ mrad) is a bump in the distribution. Hence, assuming that this information could be used to discriminate between two different families of muons which traverse the experimental set-up, we also applied a θ_μ cut. The

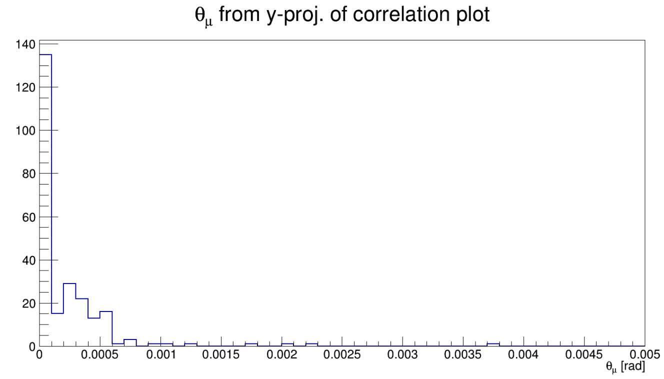

Figure 67: θ_μ distribution for the 251 events reconstructed from data.

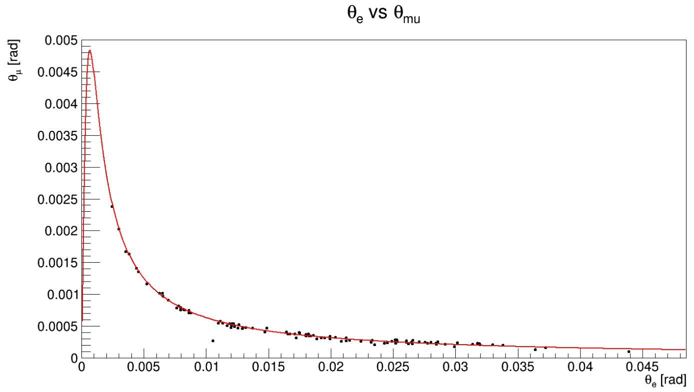

Figure 68: $\theta_\mu - \theta_e$ scatter plot after the application of $D\theta$ and $\theta_\mu > 0.1$ mrad cuts. 80 events.

result is encouraging and it is shown in Fig. 68. After the application of the $D\theta$ cut, the application of a cut at $\theta_\mu > 0.1$ mrad leaves us only with one of the two groups of muons (see Fig. 67).

The Monte Carlo simulation confirms the validity of this study, as shown in Fig. 69: we are left with 951 events on the elastic band, with very small residual background. Both in data and in the simulation, the application of the two cuts discussed above preserves $\sim 28\%$ of the initial statistics: this is a crucial point for the final experiment since, as shown in sec. 4.1, we need the order of 4×10^5 signal events to achieve the final precision on a_μ^{HLO}. However this result plays a fundamental role in terms of the final analysis strategy: we have shown that with current state-of-art silicon detectors and using an experimental apparatus not designed for scattering measurements, we could define some observables which reject with high accuracy background from other μ-interactions in the final $\theta_\mu - \theta_e$ correlation plot.

In the final experimental set-up we intend to use a calorimeter and a muon filter to perform particle ID and resolve the ambiguity in tracking, especially in the low-angles region ($\theta_e \simeq \theta_\mu \simeq 2 - 2.5$

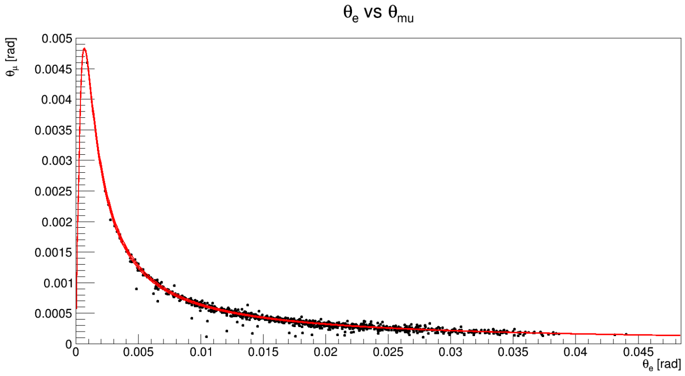

Figure 69: Simulated $\theta_\mu - \theta_e$ scatter plot after the application of $D\theta$ and $\theta_\mu > 0.1$ mrad cuts. 951 events.

mrad), and to create an energy matrix for the secondary track in order to increase the efficiency of background rejection. However, it is necessary to understand where these background events, and the signal events lost due to multiple scattering, are positioned in the correlation plot and which is their energy in order to understand if they are still present after the application of the $D\theta$ and θ_μ cuts presented here. More precisely, once we filter our dataset as shown in Fig. 68, we need to know if any corrective factor has to be estimated in order to take into account possible background event still present in the elastic region. This is a very crucial and delicate aspect of the design of the MUonE experiment, as it should ensure the feasibility of the proposed measurement and the possibility to control the signal/background ratio. In order to answer these questions we have used our `GEANT4` simulation to reproduce the Test Beam conditions and understand which is the fraction of background present in a possible data-set collected with this setup.

4.2.4.2 *Background population*

To study the problem of the background, we are interested in all the possible interaction the muon undergoes within the experimental apparatus. According to their energy and to the scattering medium properties, muons can produce secondaries in different ways and we should discriminate all of them to identify our signal of $\mu - e$ elastic scattering. There are four basic processes of muon interaction that determine muon energy loss and properties of the secondary particle(s): ionization (including production of high-energy δ-electrons), production of electron-positron pairs, bremsstrahlung and inelastic interaction with nuclei. In `GEANT4` these processes are implemented with four dedicated models:

- G4MuIonization;
- G4MuBremsstrahlung;

- G4MuPairProduction;
- G4MuNuclearInteraction.

A detailed description of these models in the simulation toolkit can be found in [41]. As pointed out above, in `GEANT4` each particle is uniquely identified by the so called `parentID`. More precisely, every primary has `parentID=0` and every secondary has `parentID=1`. In our `SteppingAction` class we derived the `G4Track` associated to the current `G4Step`. The advantage of using the `G4Track` is that it contains several useful methods to retrieve particles properties, such as the `parentID` and the `CreatorProcess`. This information can be extracted using the `GetCreatorProcess()` method of the `G4Track` class and it defines the interaction process (of the primary particle) which generated the current secondary.

Hence to address the problem of the background in our experiment, we used our simulation and we registered also the `parentID` and the `ProcessName` of the secondary track which accompanies the muon. Using the `fGeomBoundary` boolean variable we can register this information when the particle was exactly coming out from all the volumes of the detector geometry, especially the graphite target. We associated an integer to all the processes activated in the simulation:

```
if (aTrack->GetCreatorProcess()->GetProcessName() == "muIoni") {
f_processid=1;
} else if (aTrack->GetCreatorProcess()->GetProcessName() == "nuclearStopping"){
f_processid=2;
} else if (aTrack->GetCreatorProcess()->GetProcessName() == "muBrems"){
f_processid=3;
} else if (aTrack->GetCreatorProcess()->GetProcessName() == "eIoni"){
f_processid=4;
} else if (aTrack->GetCreatorProcess()->GetProcessName() == "muPairProd"){
f_processid=5;
} else if (aTrack->GetCreatorProcess()->GetProcessName() == "compt"){
f_processid=6;
} else if (aTrack->GetCreatorProcess()->GetProcessName() == "msc"){
f_processid=7;
} else if (aTrack->GetCreatorProcess()->GetProcessName() == "annihil"){
f_processid=8;
} else if (aTrack->GetCreatorProcess()->GetProcessName() == "phot"){
f_processid=9;
} else if (aTrack->GetCreatorProcess()->GetProcessName() == "eBrem"){
f_processid=10;
} else if (aTrack->GetCreatorProcess()->GetProcessName() == "conv") {
f_processid=11;
}
```

Where `f_processid` is a private variable of the `SteppingAction` class, defined to associate an integer flag when a specific interaction occurs. Along with the muon interactions defined above, we also have defined all the other interactions activated in the `PhysicsList` of this simulation. Most of them are electromagnetic interactions of electrons, since we are using the electromagnetic physics list `opt4`, specialized for this kind of interactions. Another important property of the secondary

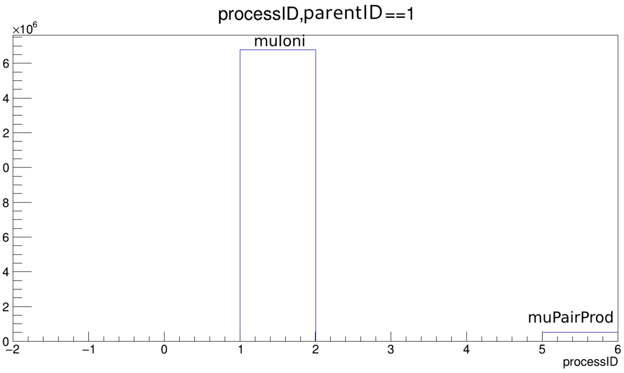

Figure 70: Histogram of the μ-interactions of secondaries coming out from the target.

which needs to be studied is its energy. In the final experiment we do not intend to measure the secondary energy in each module, but we have at disposal a calorimeter which could be used to create an energy-theta template and to impose a lower limit on E_e. Moreover it is important to understand what happens, also in terms of energy, when we apply the kinematic cuts presented in previous section in order to understand if they have a direct correspondence to secondaries energy or not.

The first important observation concerns the detector acceptance: Fig. 70 shows the `f_processid` values at the exit of the target, while Fig. 71 shows the same quantity when the selection[1] 11222 is applied to data. It is worth to note that both these plots are presented only for those events with `parentID==1`, i.e. the secondaries, because we are interested in studying $\mu - e$ events where the electron is a secondary particle coming from a muon interaction. Moreover the request of one hit in the two upstream planes and two hits in the downstream ones leaves us only with secondaries (`parentID==1`). Most of the secondaries coming out from the target (Fig. 70) are originated from a `muIonization` process and all the others come from `muPairProduction`. This is exactly what we expect from the interaction of 160 GeV muons with 8 mm thick graphite target. However when we select only those events which satisfy the request 11222 on hits multiplicity, due to the geometrical acceptance of the detector most of the electrons coming from $\mu - e$ scattering (ionization) are discarded. As we have seen in Fig. 59 some of these events, emitted at large angles, re-enter the detector acceptance due to multiple scattering, while the majority escapes the solid angle accessible with our set-up. More precisely, the number of electrons coming from pair production compose the $\sim$ 41% of the remaining dataset. However, almost all the events of $\mu \rightarrow \gamma^\star \rightarrow \mu e^+ e^-$ are arranged in the lower band of the $\theta_\mu - \theta_e$

---

[1] Here the selection is 11222 instead of 11444 as above, because in GEANT we have no ghost hits and the association hits-particle is unambiguous.

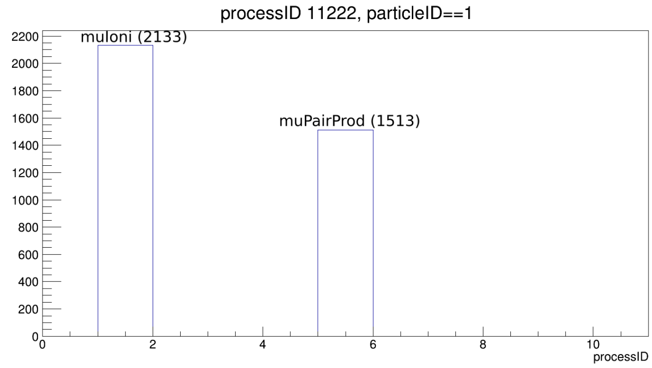

Figure 71: Histogram of the μ-interactions of secondaries coming out from the target for 11222 selection on hits.

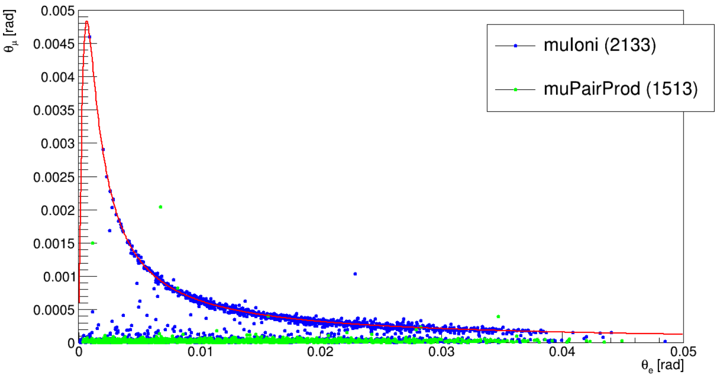

Figure 72: $\theta_e - \theta_\mu$ correlation plot with distinction on μ-interactions which generated secondary electrons.

correlation plot, as shown in Fig. 72. As expected from the theoretical event generator (see Fig. 15) the background is composed by e^+e^- events and electrons undergoing multiple scattering which re-enter the geometrical acceptance. Using the kinematic cuts proposed in the previous section (see Fig. 69) the only region which remains populated in the correlation plot is the elastic band and here we have $\sim 98\%$ of the events from muon ionization. The remaining $\sim 2\%$ of the electrons comes from muon pair production. Fig. 73 shows the $\theta_e - \theta_\mu$ plot with the different interactions distinguished one from the other and the kinematic cuts applied. Thus, the simulation confirmed that the background is composed by pair production electrons and that the application of these cuts is fundamental to select the signal region around the elastic band. However we observe that 13 background (`muPairProd`) events remain also in this final data-set. Moreover some of them also stay on the elastic curve and can not be rejected using any of the measurable observables. In order to study these events more in detail, we look at the energy they have at production: eventually we could introduce a lower limit on the secondary energy using the

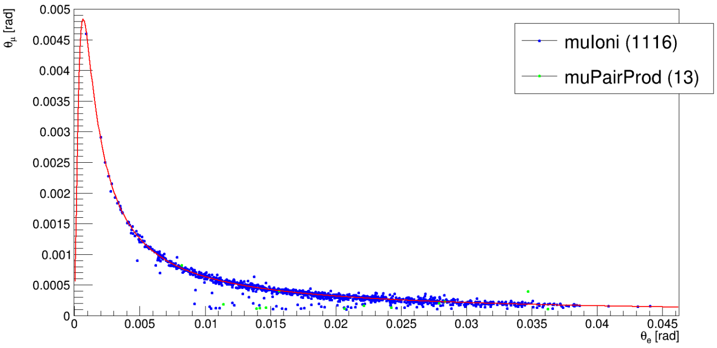

Figure 73: $\theta_e - \theta_\mu$ correlation plot with μ-interactions. Cuts presented in sec. 4.2.4.1 are applied to reject background.

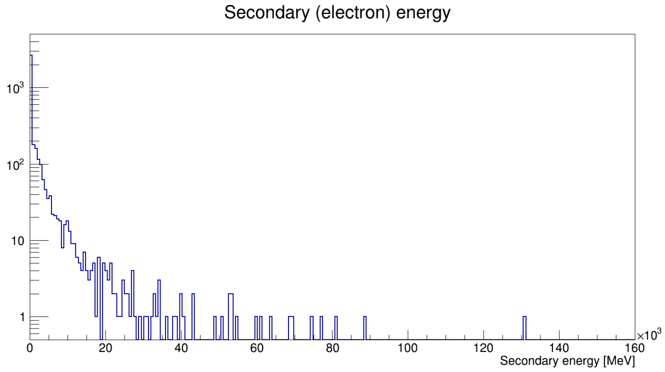

Figure 74: Energy distribution of the secondaries at exit of the target.

calorimeter (not installed in this Test Beam); otherwise one should use `GEANT4` to determine the ratio signal/background bin per bin and apply this corrective factor to the final measurement. Fig. 74 shows the energy distribution of all the secondaries coming out from the target, when there are only two tracks in the detector. We see the presence of high-energy electrons, as expected from theory (see Fig. 15) these are signal events around the peak region of the elastic curve. However most of the events contain low-energy electrons which compose both the signal region at larger θ_e angles and the background band. Fig. 75 shows the result of the correlation plot after the application of a cut on the secondary energy at 500 MeV. Since high-energy electrons compose the signal, especially around the peak region, this cut does not affect signal events except for those at large θ_e: above $\theta_e = 40$ mrad also events on the elastic curve have low-energy ($E_e < 1$ GeV, cfr. Fig. 15) and they are mixed with background from pair production. Not only most of the background from pair production is removed, but also signal events which underwent severe multiple scattering are lost. Hence we understand that the lower band highly populated in Fig. 73 is composed by low-energy events. The cut in θ_μ presented in sec. 4.2.4.1 is somehow similar to this energy cut, except for the fact that it

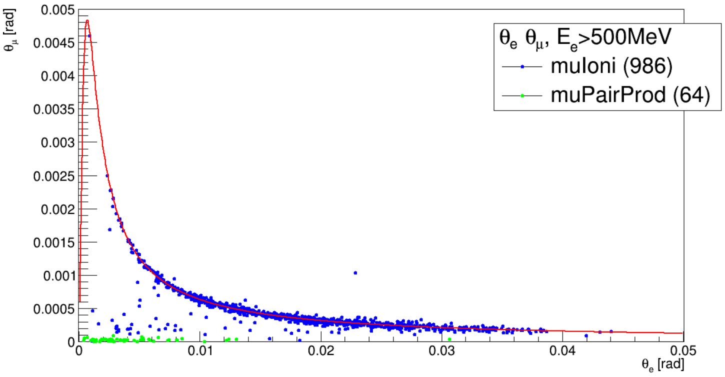

Figure 75: Simulated $\theta_e - \theta_\mu$ correlation plot with μ-interactions distinguished and cut on secondary energy at $E_e > 500$ MeV applied.

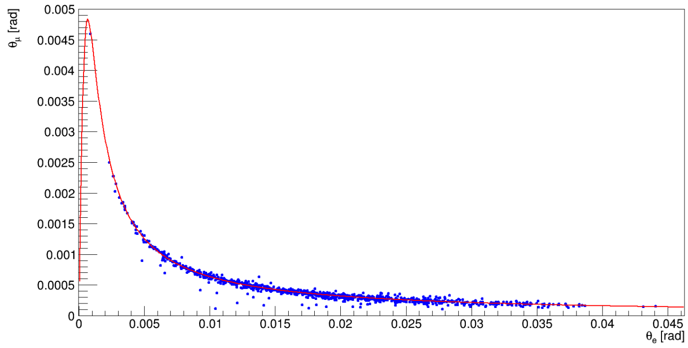

Figure 76: Simulated $\theta_e - \theta_\mu$ correlation plot. Kinematic cuts (sec. 4.2.4.1 and energy cut ($E_e > 500$ MeV) applied

rejects also background from pair production which has $E_e > 500$ MeV, as shown in Fig. 75. In our final apparatus we do not intend to measure the electrons energy event by event, but we plan to have at disposal a calorimeter positioned at the end of the detector. This study shows the necessity of using an information equivalent to this cut to get rid of events at low energies: while with kinematic cuts presented above we could not reject those background events from pair production, which were tracked on the elasticity curve, the application of an energy cut leaves us with a clear distinction between background and signal. The further application of the kinematic cuts presented above to Fig. 75 gives a very promising result: we are left with events from `muIoni`, without any background from pair production; the correlation plot is populated only by signal events which lay on the theoretical curve, confirming that the ratio signal/background can be controlled. This result is presented in Fig. 76: it appears fundamental to have at disposal the secondary energy, as it seems the only observable which permits the control of the signal/background ratio at the level expected. The 2017 Test Beam has been extremely fruitful and helped

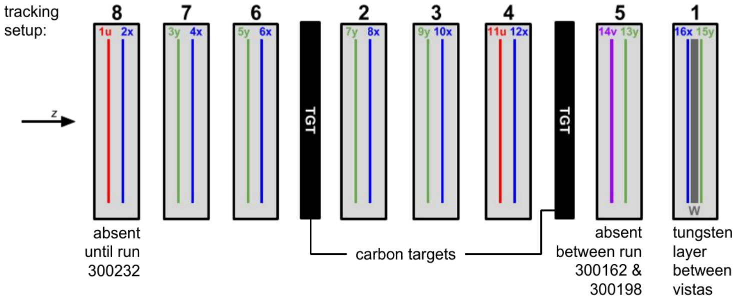

Figure 77: Scheme of the apparatus used for the 2018 Test Beam.

us a lot in understanding several aspects fundamental for the MUonE experiment. The study presented in this section is entirely based on the `GEANT4` simulation and could not be validated using data since in this Test Beam we did not have at disposal a calorimeter. If the calorimeter does not provide the possibility to discard low-energy events we could only apply the cuts presented in sec. 4.2.4.1 and we should evaluate the ratio signal/background from Fig.73 for those `muPairProd` events which have low energy but fall on the elastic band.

4.3 TEST BEAM 2018

In order to answer this question and to investigate more in detail the possibility of using a calorimeter to perform particle ID and to have at disposal a lower limit on energy, in April 2018 we started a new Test Beam which is going to last until October. We installed the experimental set-up behind COMPASS and we plan to use high energy μ beams $(180-190$ GeV) to perform scattering measurements. In addition to the calorimeter, in this Test Beam we have also installed two targets in order to study the effect of subsequent modules in the final apparatus. The detector consists of 8 tracking stations and two graphite target 8 mm thick. Each station is composed by two single-sided silicon detectors of 9.3×9.3 cm^2 active area. Their physical pitch is 121 μm, with a readout pitch of 242 μm with floating strips. These trackers are 410 μm thick and their resolution on measured hits is $\sim 35-40\mu$m. Fig. 77 shows the scheme of the experimental apparatus. Each station contains two tracking planes, but in boxes $8, 4, 5$ we have stereo planes. One of the difficulties in tracking $\mu-e$ events in the 2017 Test Beam was the presence of ghost hits: using the 11444 selection we could automatically discard one of the two ghosts, as said above; however in the final apparatus we expect to analyze also other topologies, where more than two tracks are in the detector. Hence it is fundamental to resolve ambiguities coming from the alignment procedure: this is the role of the u, v planes installed in this set-up. We expect to use hits registered on these tracking planes

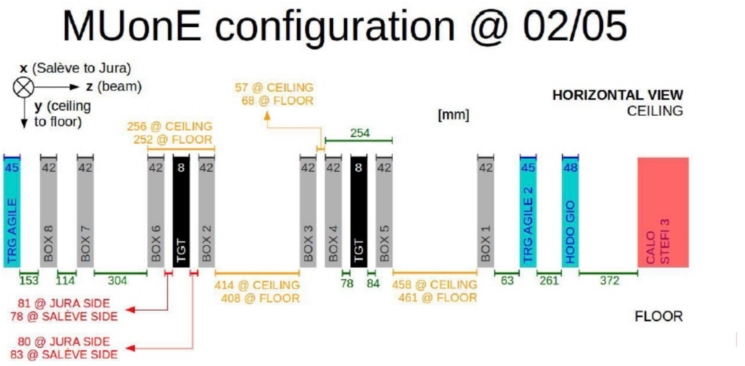

Figure 78: Test Beam 2018 experimental set-up with measured distances.

to uniquely determine hits on the x, y planes which precede/follow the stereo ones. Stereo planes have the same configuration of the normal ones but are installed with a $45°$ rotation. Moreover when the two scattered particles have small angles $\theta_e \simeq \theta_\mu \simeq 2.5/3$ mrad, it is difficult to reconstruct the two tracks and to distinguish one particle from the other. In this Test Beam we have at disposal a calorimeter installed at the end of the apparatus (not shown in Fig. 77) which should help us to perform particle ID in the ambiguity region.

The distances between tracking planes and targets are shown in Fig. 78: both the upstream and downstream lever arms are smaller than the ones at disposal with the UA9 apparatus in the 2017 test beam. The main consequence of this smaller set-up is the worsening of the intrinsic angular resolution within respect the one of the past year ($\sim$ 0.02 mrad with 160 GeV muons, see Fig. 50). In fact with 40μm of resolution on hits one has

$$\sigma_{intr.} = \frac{\sigma_{hits}\sqrt{2}}{D}, \; D = 55 \text{ cm}$$

$$\sigma_{intr.} \simeq 0.1 \text{ mrad}$$

In this test beam we worked with two muon beams of different profiles and energy spread:

- Muons from modified M2 (used for two weeks in April);
- Muons from π decays.

The M2 μ beam has $\sigma_x = 93.4$ mm and $\sigma_y = 99.8$ mm with a flux for 10^{13} pot/spill of $\sim 10^6/\text{cm}^2$, while the muon beam from pion decays has $\sigma_x = 80.9$ mm and $\sigma_y = 83.7$ mm, with a measured mean momentum of $\langle p_\mu \rangle = 186.8$ GeV and $\sigma_{p_\mu} = 6.5$ GeV. It is fundamental to link these conditions to each run of our data taking. Without this information we could not simulate with precision the beam profiles and perform the analysis of $\mu - e$ events with the required precision.

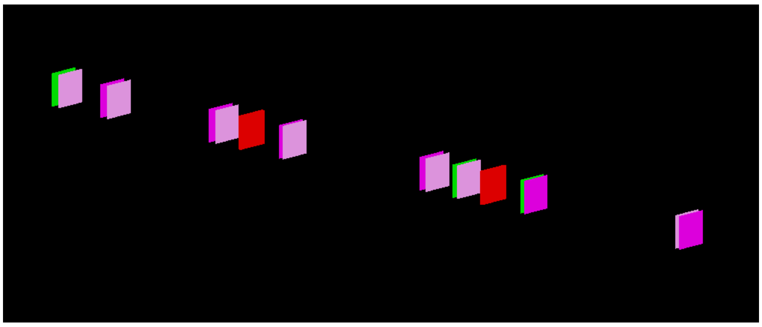

Figure 79: Test Beam 2018 geometry implemented in Geant4. Trackers in violet, targets in red and u, v planes in green.

During these months we have improved the alignment algorithm used for the 2017 Test Beam to process raw data acquired from the set-up to prepare them for the analysis. As one can see from Fig. 77 distances are not regular between the upper and lower parts of the apparatus and these tilts must be taken into account to regularize and prepare data for the analysis. We have also developed a simulation of this set-up. During the alignment phase we have started looking at hits profiles and it appears clear that the beam is not entering the detector parallel to the horizontal axis and that some *Si* planes have hardware problems which lead to critical inefficiencies in their readout. Hence, the `GEANT4` simulation is extremely important to control the result of the analysis and to confirm that this apparatus could be used with a 190 GeV beam to detect $\mu - e$ elastic scattering. Moreover it is important to study the calorimeter signal and validate it with the simulation to understand its efficiency in particle identification and the possibility to use it to reject background events.

Fig. 79 shows the reconstructed geometry using `GEANT4`. Details of the simulation are the same presented in sec. 4.2.2, with distances and dimensions modified according to the new geometry. The two targets are 8 mm thick and are made of the same graphite used for the 2017 targets ($\rho = 1.83\text{g/cm}^3$).

In the `PrimaryGenerator` class we simulate a simple beam profile consisting of a 187.0 GeV μ^+ beam parallel to the z axis (x in `GEANT4`), with position randomly selected within the active area of the trackers. The simulation works has presented in sec. 4.2.2: the `.txt` files produced are processed with a `ROOT` macro, which adds to the hits the smearing due to the detector intrinsic resolution and produces the `TTree` with the *ntuples* containing the informations registered. The tracking algorithm used is a simple extension of the one used for the 2017 analysis: except for distances, the first module has the same structure of the UA9 set-up with two upstream planes and three downstream ones. Moreover we could use the stereo planes to solve ambiguities and we should increase the efficiency in reconstructing $\mu - e$ elastic event. The problem is that the tracking planes present

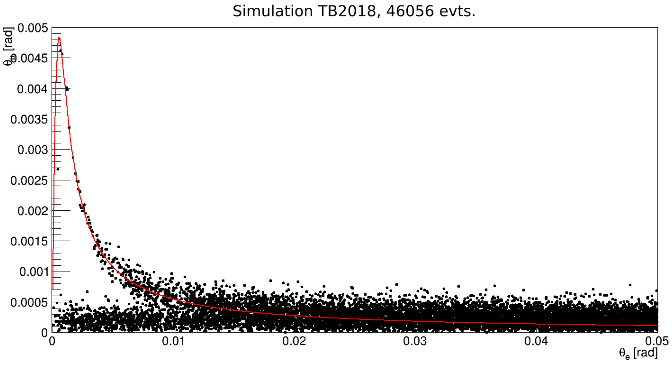

Figure 80: $\theta_e - \theta_\mu$ correlation plot obtained from the simulation of the 2018 Test Beam. $150E6$ muons at 187 ± 7 GeV.

some severe inefficiencies and these are correlated one plane from the other. Due to this situation, the alignment procedure of these data took more than expected, because we had to control that all the reference frames used for the data alignment were suitable and did not contain the most inefficient trackers. As a consequence of these inefficiencies, we need to merge different runs to collect enough statistics to reconstruct elastic events. However, the analysis of the first ~ 5 weeks runs did not show any clear angular correlation of $\mu - e$ elastic events reconstructed. Hence, to understand these problematics we used the `GEANT4` simulation, where the efficiency in tracks selection is maximum and silicon planes do not present strange behavior in hits recording. Fig. 80 shows the $\theta_e - \theta_\mu$ correlation plot obtained from $150e6$ incoming muons simulated, when we require only one track entering the detector (selection with max. efficiency ($\epsilon = 1$) in `GEANT4`) and two tracks in the first module of the experimental set-up, as we did for the 2017 Test Beam data and simulation. This constraint on multiplicity on trackers leaves us with 46056 events. In this Test Beam we are using an apparatus with shorter lever arms within respect the 2017 detector and Si trackers have a worse intrinsic resolution: the result is the important background band in the correlation plot. Moreover, this apparatus also has a larger angular acceptance within respect the 2017 one: we had $35 - 40$ mrad for the 2017 detector and $\sim 160 - 200$ mrad for the 2018 one. We see that most of the events reconstructed populate this region, instead of the signal one (elastic curve). However with such an high statistics, we show that signal can be distinguished from background. Especially for $\theta_e < 15 - 10$ mrad the signal and background populations become distinct and actually there are events which lay on the 187 GeV elastic curve.

As we did for the 2017 Test Beam, we have reproduced the angles correlation plot distinguishing contributions from different μ-interactions. The result is presented in Fig. 81 and it is analogous to what we have found the past year. Background events are composed

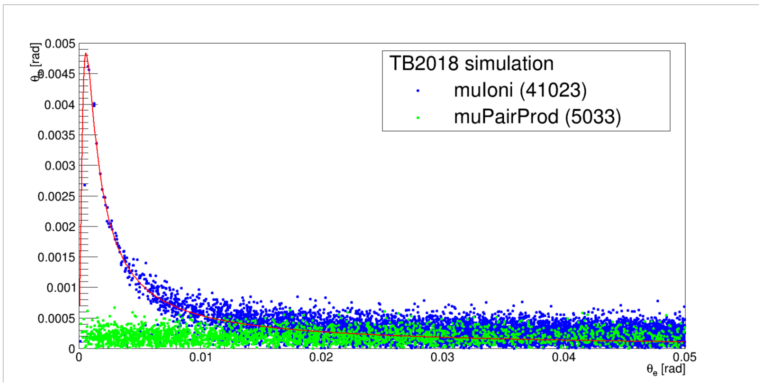

Figure 81: Simulated $\theta_e - \theta_\mu$ correlation plot with μ-interactions distinguished one from the other.

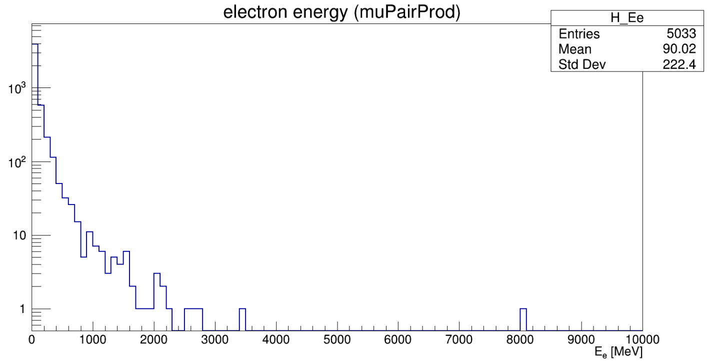

Figure 82: Energy spectrum of muPairProd events.

by pair production, intrinsically mixed with signal events lost due to severe multiple scattering. The background population is highly mixed with signal with respect the 2017, due to the acceptance and resolution of the detector used. For $\theta_e > 10$ mrad signal and background are no longer distinguishable and there is high contamination of the elastic band. From `GEANT4` we can extract the energy of these particles to better describe this population. Fig. 82 shows the energy spectrum of the background events: all the events from `muPairProd` are characterized by low-energy electrons (or positrons, since we do not distinguish the charge). When a cut on the secondary energy is applied, most of the events coming from e^+e^- production are rejected, as well as electrons from elastic events which have an important multiple scattering effect. More precisely, in the correlation plot for $E_e > 500$ MeV only few events from pair production are left in the bottom left corner, as shown in Fig. 83.

The collaboration is currently working on the data analysis of the 2018 Test Beam and further results and Monte Carlo validation are going to be the next steps of the MUonE project. Starting from the dedicated `GEANT4` we could confirm that signal events are expected, hidden in data due to the available accuracy of silicon trackers and

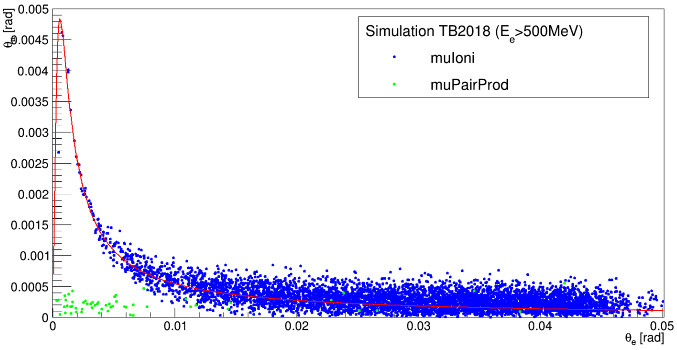

Figure 83: Simulated $\theta_e - \theta_\mu$ correlation plot with secondary energy cut applied. $E_e > 500$ MeV.

their intrinsic resolution on hits. The apparatus used this year allows to investigate a wide angular acceptance, however most of the events at $\theta_e > 30 - 40$ mrad are going to be useless due to the intrinsic mix of background and signal.

5

CONCLUSIONS

The MUonE experiment has the goal to measure the leading order hadronic contribution (a_μ^{HLO}) to a_μ with a statistical uncertainty of 0.3% exploiting $\mu - e$ elastic scattering. The crucial part of this innovative experiment is to control systematic uncertainty at the same level of statistical one. The experiment is primarily based on a precise measurement of the angles of the two outgoing particles as the q^2 of the $\mu - e$ interaction can be directly determined from one of the two scattering angles.

The basic detector foresees a modular apparatus, each module being composed of a target and three tracking layers. A low-Z target, limiting the effect of multiple scattering as well as other μ-interactions, will be used as scattering center.

In October 2017 we had a Test Beam dedicated to the MUonE experiment to study multiple scattering on $\mathcal{O}(10\ \text{GeV})$ electrons and to test a proof-of-concept of one module of the final detector. The intent of this test beam was to achieve a precise description of the multiple scattering effect in thin graphite targets and to develop a `GEANT4` simulation of the experimental apparatus to validate results of the analysis. Results are presented in sec. 4.2.

The analysis of 12, 20 GeV electrons allowed us to improve the `GEANT4` simulation and to achieve a $\sim 1\%$ agreement between data and Monte Carlo (sec. 4.2.2). We studied in detail the effect of multiple scattering in thin carbon targets (sec. 4.2.3) and we were able to estimate the effect on the overall resolution of the experimental apparatus. We also studied an analytical expression adequate to describe the multiple scattering in the silicon telescope. Using the convolution of a gaussian distribution and a Student's t we obtained an overall good agreement for all the test cases studied. A complementary use of the `GEANT4` simulation and of the analytical approach could allow us to have a deep understanding of all the components of the angular deflection distributions and to model multiple scattering with a systematic accuracy better than 1%.

Using a 160 GeV μ beam we could collect data during the last day of the allocated week for a total of $\sim 1.5 \times 10^6$ events. Notwithstanding the apparatus used is not specialized for scattering measurements, we could observe a first $\theta_e - \theta_\mu$ correlation plot (see Fig. 58) which confirms the validity of our proof-of-concept detector module. Using our `GEANT4` simulation we have performed a detailed analysis on this topic to investigate possible kinematic cuts to select signal with high efficiency and to understand which μ-interactions populate the background and to quantify the signal/background ratio (sec. 4.2.4).

We validated these preliminary results using the `GEANT4` simulation. The kinematic cuts studied could be used to reject background and preserve only signal events. We demonstrated that background mainly comes from e^+e^- pair production from muon interaction, as well as from e^- which underwent severe multiple scattering in target. We have also shown that a possible cut on secondary energy (e.g. $E_e > 500$ MeV) could help to reject background.

In April 2018 a new Test Beam has started and it will run continuously until October 2018, collecting data with muons. The experimental apparatus used in this test beam is dedicated to the MUonE experiment and it contains two modules, instead of one as in the 2017 TB, and a calorimeter has been installed at the end of last module. We have already developed a dedicated `GEANT4` simulation for this year Test Beam and we have studied the feasibility of collecting signal events with a detector resolution lower than the past year. We have confirmed that signal events are expected, however the statistics collected so far is too low. The presence of hardware inefficiencies and a 0.1 mrad angular resolution, increased the time needed to collect high statistics. With the simulation we have also studied the background population, obtaining results in agreement with expectations: e^+e^- pairs populate background; a possible cut on secondary energy could help to control the ratio signal/background.

We have developed a dedicated simulation, which confirmed that the same apparatus, without inefficiencies, could resolve $\mu - e$ signal events for $\theta_e < 10$ mrad. In the next months we plan to study the calorimeter signal and to use it to discriminate ambiguities in particle identification. Along with this we are improving the `GEANT4` simulation to perform dedicated studies on geometry and trackers thickness. In addition, the complete simulation obtained starting from this work is going to be used to simulate the final apparatus of the MUonE experiment.

In this work we have studied several issues of fundamental importance for the MUonE experiment. None of the two test beams returned results which could be interpreted as show-stoppers for the final experiment.

The MUonE experiment proposes to use a simple and robust technique, which has the potential to keep systematic effects under control, aiming to reach a systematic uncertainty of the same order as the statistical one. Preliminary results from Test Beams and simulations validated the experimental idea and the proposed method. Eventually, with a muons beam of 150 GeV with an average intensity of $\sim 1.3 \times 10^7$ μ/s, available at the CERN North Area, a statistical uncertainty of $\sim$ 0.3% can be achieved on a_μ^{HLO} in two years of data taking.

LIST OF FIGURES

BIBLIOGRAPHY

[1] E989 Collaboration (J. Grange et al.), "Muon (g-2) Technical Design Report", arXiv:1501.06858v1, (2015).

[2] F.J.M. Farley, Y.K. Semertzidis, "The 47 years of muon g - 2", Progress in Part. and Nuc. Phys., 52 (2004) 1-83, 2004. [doi:10.1016/j.ppnp.2003.09.004]

[3] A.B Arbuzov, D. Haidt, C. Matteuzzi, M. Paganoni, L. Trentadue, "The running of the electromagnetic coupling alpha in small-angle Bhabha scattering", Eur. Phys. J. c34 (2004) 267-275, 2004.

[4] A.B. Arbuzov, V.S. Fadin, E.A. Kuraev, L.N. Lipatov, N.P. Merenkov and L. Trentadue, "Small-angle electron-positron scattering with a per mille accuracy", Nucl. Phys. B485 (1997) 457.

[5] R. Bouchendira, P. Clade, S. Guellati-Khelifa, F. Nez and F. Biraben, "New determination of the Fine Strucutre Constant and Test of the Quantum Electrodynamics", Phys. Rev. Lett., 106 (2011). 080801

[6] M. Tanabashi et al. (Particle Data Group), Phys. Rev. D 98, 010001 (2018).

[7] A. Czarnecki, B. Krause and W. J. Marciano, Phys. Rev. Lett. 76 (1996) 3267.

[8] C. Gnendiger, D. Stöckinger and H. Stöckinger-Kim, Phys. Rev. D88 (2013) 053005.

[9] T. Blum, A. Denig, I. Logashenko, E. de Rafael, B. Lee Roberts, T. Teubner, G. Venanzoni, "The Muon (g-2) Theory Value: Present and Future", arXiv:1311.2198v1, (2013).

[10] K. Hagiwara, R. Liao, A. D. Martin, D. Nomura and T. Teubner, J. Phys. G38 (2011) 085003.

[11] M. Davier, A. Hoecker, B. Malaescu and Z. Zhang, Eur. Phys. J. C71 (2011) 1515, Erratum-ibid. C72 (2012) 1874.

[12] J. Prades, E. de Rafael and A. Vainshtein, in Advanced Series on Directions in High Energy Physics - Vol. 20 Lepton Dipole Moments, eds. B. L. Roberts and W. J. Marciano, World Scientific (2010), p. 303; arXiv:0901.0306v1

[13] T. Aoyama, M. Hayakawa, T. Kinoshita and M. Nio, Phys. Rev. Lett. 109 (2012) 111808.

[14] J. P. Miller, E. de Rafael, B. L. Roberts and D. Stöckinger, Ann. Rev. Nucl. Part. Sci. 62 (2012) 237.

[15] J. Prades, E. de Rafael and A. Vainshtein, in Advanced Series on Directions in High Energy Physics - Vol. 20 Lepton Dipole Moments, eds. B. L. Roberts and W. J. Marciano, World Scientific (2010), p. 303; and arXiv:0901.0306v1.

[16] G. Charpak, F. J. M. Farley, R. L. Garwin, T. Muller, J. C. Sens, V. L. Telegdi, and A. Zichichi, "Measurement of the anomalous magnetic moment of the muon", Phys. Rev. Lett. vol. 6 no. 3 , 1961.

[17] F. Combley et al. "The CERN muon (g-2) experiments", Phys. Rep. 68, no. 2 (1981), 93-119, 1981.

[18] G. W. Bennett, et al. (Muon g-2 Collaboration), "Final Report of the Muon E821 Anomalous Magnetic Moment Measurement at BNL", 2006, arXiv:hep-ex/0602035v1.

[19] N. Saito [J-PARC g-2/EDM Collaboration], AIP Conf. Proc. 1467 (2012) 45.

[20] F. Jegerlehner and R. Szafron, Eur. Phys. J. C 71 (2011) 1632.

[21] F. Jegerlehner, arXiv:1705.00263

[22] M. Davier, A. Hoecker, B. Malaescu and Z. Zhang, Eur. Phys. J. C 77 (2017) 827.

[23] A. Keshavarzi, D. Nomura, T. Teubner, "The hadronic vacuum polarsation contributions to the muon g-2", arXiv:1802.06229v1 (2018).

[24] KLOE Collaboration, F. Ambrosino et al., Phys. Lett. B700 (2011) 102.

[25] CMD-2 Collaboration, R. R. Akhmetshin et al., Phys. Lett. B648 (2007) 28, arXiv:hep-ex/0610021.

[26] B. Aubert et al. [BaBar Collaboration], Phys. Rev. Lett. 103 (2009) 231801.

[27] D. Babusci et al. [KLOE Collaboration], Phys. Lett. B 720 (2013) 336.

[28] A. Anastasi et al. [KLOE-2 Collaboration], arXiv:1711.03085 [hep-ex].

[29] M. Ablikim et al. [BESIII Collaboration], Phys. Lett. B 753 (2016) 629.

[30] C. M. Carloni Calame, M. Passera, L. Trentadue, G. Venanzoni, "A new approach to evaluate the leading hadronic corrections to the muon g-2", Phys. Lett. B 746 (2015) 325.

[31] G. Abbiendi et al., "Measuring the leading hadronic contribution to the muon g-2 via $\mu - e$ scattering", 2016, arXiv:1609.08987v1.

[32] R. Losito, E. Laface, W. Scandale, "The UA9 Experiment at the CERN-SPS", Particle Accelerator Conference 2009, Vancouver, Canada, 04 - 08 May 2009, pp.WE6RFP024

[33] S. Agostinelli et al., "GEANT4-a simulation toolkit", Nuc. Inst. and Meth. in Phys. Res., vol. 506 (3), 250-303, 2003.

[34] G. Moliere, "Theorie der Streuung schneller geladener Teilchen", I.I. Mehrfach- und Vielfachstreuung. Z Naturforsch, pp. 78-85

[35] G.R. Lynch, O.I. Dahl, "Approximations to multiple Coulomb scattering", Nucl. Instr. and Meth., B58 (1991), p. 6

[36] R. Früwirth, M. Regler, "On the quantitative modelling of core and tails of multiple scattering by Gaussian mixtures", Nucl. Instr. Meth. Phys. Res., 456 (2001), 369-389.

[37] R. Früwirth, M. Liendl, "Mixture models of multiple scattering: computation and simulation", Computer Physics Communications, 14 (2001), 230-246.

[38] N. Berger et al., "Multiple Coulomb Scattering in thin silicon", Jour. of Inst., 9 (2014)

[39] P. Billoirm, "Track fitting with multiple scattering: a new method", Nuc. Inst. Met. in Phys. Res., 225 (1994)

[40] NA7 Collaboration, "A measurement of the space-like pion electromagnetic form factor", Nuc. Phys. B277 (1986) 168-196.

[41] A. G. Bogdanov et al., "Geant4 Simulation of Production and Interaction of Muons", IEEE Trans. Nuc. Sci., vol. 55, n. 2, April 2006.